# Viscous and second gradient regularization techniques for the description of the behavior of geomaterials

Huan Wang

## ▶ To cite this version:

HAL Id: tel-02954012

https://theses.hal.science/tel-02954012

Submitted on 30 Sep 2020

# THESE DE DOCTORAT DE

L'ÉCOLE CENTRALE DE NANTES

COMUE UNIVERSITE BRETAGNE LOIRE

ECOLE DOCTORALE N° 602
*Sciences pour l'Ingénieur*
Spécialité : Génie civil

Par

## « Huan WANG»

## « Viscous and second gradient regularization techniques for the description of the behavior of geomaterials»

**Thèse présentée et soutenue à NANTES, le 13/12/2019**
**Unité de recherche : UMR 6183, Institut de Recherche en Génie Civil et Mécanique (GeM)**

**Rapporteurs avant soutenance** :

Pierre BESUELLE          Chargé de recherche, CNRS, Université Grenoble Alpes
Angela MADEO             Professeur des Universités, INSA Lyon

**Composition du Jury :**

Président : Pierre BESUELLE                Chargé de recherche, CNRS, Université Grenoble Alpes

Examinateurs : Frédéric COLLIN            Professeur, University of Liège
               Jacopo CIAMBELLA          Assistant Professor, University of Rome

Dir. de thèse : Panagiotis KOTRONIS       Professeur, Ecole Centrale de Nantes
Co-dir. de thèse : Giulio SCIARRA         Professeur, Ecole Centrale de Nantes

# Acknowledgements

I would like to thank my supervisors Panagiotis KOTRONIS and Giulio SCIARRA for their dedication in guiding me during my three-year study at CENTRALE NANTES. Without their help, it is not possible for me to finish my Ph.D. study. Their suggestions have greatly shaped my view on research work and life. From the first day I entered in ECN, Panos gives me endless support and encouragement. Every time, I stuck on a subject, it is his encouragement and advice that helped me to solve the problem. His optimism and rigorous working attitude have impressed me most and will benefit me for a lifetime. Giulio who is very hardworking with a lot of patience. Whenever I have questions, he will always be there and willing to help me figure it out. I am very grateful for those countless discussions.

Besides my supervisors, I would also express my great gratitude to my jury committee members, Professors Frédéric, Pierre, Angela and Jacopo, for providing me with great support and invaluable advice to refine my work.

I am also very grateful to Professor YIN Zhenyu for his helpful suggestions on research and life during the three years. I would also appreciate Professor Pierre-Yves HICHER and SHIMU, Ms Pearl-Angelika Lee for their instructions on research, language learning skills in these three years.

I am so fortunate to be surrounded by great companies through my study and life. I would give my gratitude to my colleagues in the GeM lab, GUO Menghuan, Ibrahim Bitar, ZHAO Chaofa, WU Zexiang, LIU Jiangxin, ZHU Ran, JIN Zhuang, YANG Jie, Andreea Roxana Vasilescu, LIU Xiaodong, ZOU Yuliang, YIN Kexin, Androniki-Anna Doulgeroglou, WU Guowei. Thanks for their useful suggestions and enjoyable discussions. I would also like to thank my classmates in college, CAO Shuhan, WANG Chuang and MA Chaolun for their encouragement and precious talks. Also many thanks for my friend ZHAO Hui, XING Yangkai, SHI Yabin, LUO Qiuyue, LI Siyuan, DENG Yang, HONG Zhen, Gêne, LI Zheng, TANG Xuejiao and CHEN Chuan, thanks for their accompany and the major life events we

1

shared together.

Finally, I would like to express my deepest gratitude to my family. Thanks for their continuous support and endless love which enable me to finish my Ph.D. study and pursue my initial dream here. Whenever I feel depressed and sad, it's their love that encourages me all the time.

# Abstract

Geomaterials may exhibit time-dependent behaviors as their microstructures evolve. This process may vary from a few minutes (sand) to several days or even years (soft soils). To describe this time-dependent behavior, viscoplastic models are commonly used. Other than providing an intrinsic description of the viscous behavior, rate-dependent constitutive laws are sometimes presented in the literature as a regularization technique.

In this thesis, we study the possibility to use viscoplastic constitutive laws in transient problems to describe the time-dependent response of soft soils and strain localization. Analytical and numerical studies are presented and several conclusions are found based on the Hill's criterion, the Rice's criterion, a numerical perturbation algorithm and classical linear perturbation theory. It turns out that the use of viscoplastic models in transient problems is not able to regularize the problem.

Viscoplastic models are then integrated in a higher order continuum, the second gradient model. Problems concerning the uniqueness, bifurcation and mesh dependency are examined and a classical linear perturbation analysis is presented. The combination of a second gradient model with viscoplastic laws makes possible both to regularize the problem and to take into account rate effects. Finally, the bearing capacity and progressive failure of a shallow foundation are analyzed in order to demonstrate the performance of the approach on a real case study.

**Key words:** regularization, strain localization, viscoplasticity, second gradient, uniqueness, bifurcation, mesh dependency, stability

# Résumé

Les géomatériaux présentent des comportements plus ou moins dépendants du temps, car leur microstructure évolue. Ce processus peut varier entre quelques minutes (sable) et plusieurs jours voire plusieurs années (sols mous). Pour décrire un comportement dépendant du temps, des modèles viscoplastiques, dépendant de la vitesse, sont couramment utilisés. Autre qu'une description intrinsèque du comportement visqueux, la dépendance à la vitesse de la loi constitutive est également présentée quelques fois dans la littérature comme une technique de régularisation.

On étudie dans cette thèse la possibilité d'utiliser une loi de comportement viscoplastique pour décrire le comportement transitoire des sols mous dépendant du temps et la localisation des déformations. Des études analytiques et numériques sont présentées et plusieurs conclusions sont trouvées sur la base du critère de Hill, du critère de Rice, d'un algorithme de perturbation numérique et de la théorie classique de perturbation linéaire. Il s'avère que l'utilisation d'un modèle viscoplastique pour des chargements transitoires ne permet pas de régulariser le problème.

Afin de proposer une stratégie de modélisation performante, les modèles viscoplastiques sont ensuite intégrées dans un milieu à microstructure et plus spécifiquement dans un modèle second gradient. Des problèmes concernant l'unicité, la bifurcation et la dépendance au maillage sont examinés et une analyse classique de perturbation linéaire est présentée. La combinaison d'un modèle second gradient avec des lois viscoplastiques permet de régulariser le problème et de prendre en compte l'influence de la vitesse de la sollicitation. Afin de démontrer la performance de l'approche dans un cas réel, une fondation superficielle est analysée en mettant l'accent sur sa capacité portante et sa défaillance progressive.

**Mots clés**: régularisation, localisation des déformations, viscoplasticité, second gradient, unicité, bifurcation, dépendance au maillage, stabilité

# Table of contents

# List of Figures

9

12

# List of Tables

# List of notations and abbreviations

**LATIN SYMBOLS**

$c$          Cohesion

$e$          Void ratio

$e_0$         Initial void ratio

$f$          Yield function

$g$          Potential function

$M$          Slope of critical state line

$p$          Mean effective stress

$p_c$         Preconsolidation pressure

$q$          Deviatoric stress

$u$          Displacement

**GREEK SYMBOLS**

$\Delta\lambda$         Plastic multiplier

$\Omega$         Integration domain in a unit sphere

$\psi$          Dilatation angle

$\rho$          Materials density

$\sigma$          Cauchy stress tensor

$\varepsilon$          Euler strain tensor

$\varphi$        Friction angle

$\chi_{ijk}$       Double strain tensor

$\Sigma_{ijk}$       Double stress tensor

## ABBREVIATIONS

CPM       Cutting Plane Method

CPPM       Closest Point Projection Method

CT       Computed Tomography

DEM       Discrete Element Method

DIC       Digital Image Correlation

FEM       Finite Element Method

Q4       8-node quadrilateral finite element

Q8       4-node quadrilateral finite element

Q9       9-node quadrilateral finite element

REV       Representative Element Volume

# Chapter 1

# General introduction

## 1.1 Background and motivation

Geomaterials may exhibit time-dependent behavior as their microstructure evolves. This process varies from a few minutes (sand) to several days or even years (soft soils) and has been investigated by various researches in both laboratory and field. Three typical laboratory time-dependent tests are often performed: creep, Constant Strain Rate (CSR) and stress relaxation tests (see for example [9, 10, 11]). In field studies, one can mention the uneven settlement of the Pisa Tower in Italy [12] or the settlements of buildings on Norwegian normally-consolidated marine clays in Drammen [1].

Several constitutive models have been proposed to describe the time-dependent behavior. They could be classified into three categories: empirical, rheological and stress-strain rate dependent models. Viscoplastic models belong to the third group and are commonly used for boundary value problems with the finite element method.

Other than an intrinsic description of the viscous behavior, viscoplastic constitutive laws are sometimes presented in the literature as a regularization technique for strain localization problems. Strain localization occurs as compaction bands and shear bands and it is a precursor to failure of geomaterials (e.g. soft soils, stiff clay, sand, rock). Its reliable prevention and accurate prediction are therefore of great significance for structural safety. Within the framework of continuum mechanics and when no internal length is considered pathological problems appear, e.g. the thickness of the localization zone narrows and tends towards zero (indicating a zero energy dissipation) with mesh refinement. The introduction of an internal length regularizes the equations and can be done in several ways: non-local models

[13, 14, 15], gradient plasticity [16] and continua with microstructure [17, 18]. The regularization effect of viscosity has been studied by numerous researchers in recent years but conclusions are contradictory [19, 20, 21]. The capacity of viscoplasticity in regularizing the problem is therefore questioned.

## 1.2 Thesis objectives

The objective of this PhD is to study the ability of viscoplastic constitutive laws to describe the time-dependent response of soft soils and strain localization. Questions concerning uniqueness, bifurcation, stability and mesh dependency are answered and then viscoplastic models are used in a second gradient medium in order to improve the model performance. The bearing capacity and post-peak progressive failure of a shallow foundation are finally simulated to illustrate the advantages of the proposed approach.

## 1.3 Thesis outline

This thesis is organized in the following way:

Firstly, experimental results on time-dependent behaviour are reviewed. Three commonly used viscoplastic models are presented and their algorithms are explained. Strain localization, loss of uniqueness and stability are illustrated. Moreover, several numerical techniques for strain localization are summarized.

Secondly, we study the ability of viscoplastic constitutive laws for soft soils to describe their time-dependent response. Analytical and numerical studies are presented focusing on the the so-called regularization effect which several authors attribute to the viscoplastic model. Next, a viscoplastic constitutive law is introduced in a second gradient medium and a validation test is performed. Uniqueness, bifurcation, mesh-dependency and stability issues are revisited.

Finally, the model is applied for an engineering case study, i.e. the bearing capacity and progressive failure of a swallow foundation.

The following notations are adopted; compression is positive, tensor indices are located at the lower position, bold letters are used for fourth-order tensors. Dots denote derivatives

with respect to time and the superscript $\mathrm{T}$ denotes the transpose. Inertial forces are neglected and the small strain hypothesis is adopted.

# Chapter 2

# Literature review

## 2.1 Experimental results of time-dependent behaviour of geomaterials

Geomaterials may exhibit a time dependent behaviour as their microstructure evolves with time. The process may vary from a few minutes (sand) to several days or even years (soft soil) [22]. The time-dependent behaviour is observed experimentally as creep, stress relaxation or influence of the velocity under constant strain rate (CSR) [23], illustrated in Fig 2.1.



(a) Creep      (b) Stress relaxation      (c) Constant strain rate
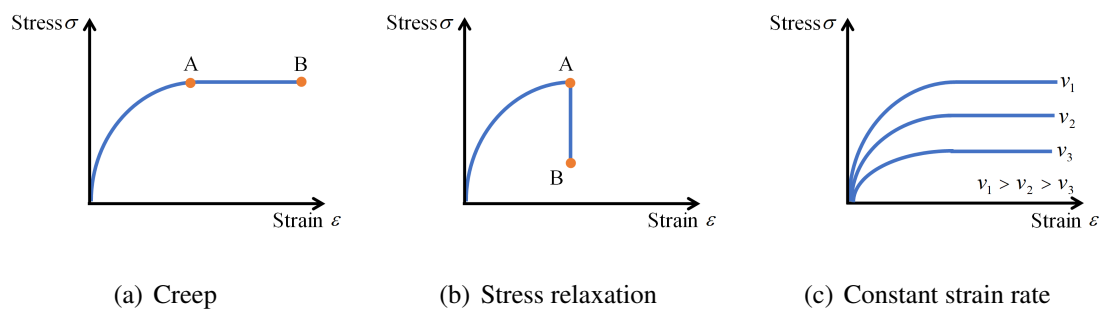
Figure 2.1: Illustration of the time dependent behaviour of soils

### 2.1.1 Time-dependent behaviour of soft soils

Viscous phenomena in geotechnical engineering are generally admitted to take place in clayey soils during secondary consolidation, say during the soil settlement occurring once the effective stress has attained its equilibrium value. This is for instance the case of the

uneven settlement of the Pisa Tower in Italy, identified as caused by creep [12]. Bjerrum [1] reviewed several geological processes changing with time for Norwegian normally-consolidated marine clays. The settlements of six representative buildings in Drammen are for example depicted in Fig 2.2. In Western Finland, Murro test embankment built on 23-m-thick medium sensitive clay in 1993. Settlement were recorded to exceed 70mm during 1000 days after construction [24]. Viscous phenomenon on soft clay was also observed for two trial embankments with significant creep deformation measured for three years [25].

Time-dependent behaviour is commonly observed in soft soils and has been investigated
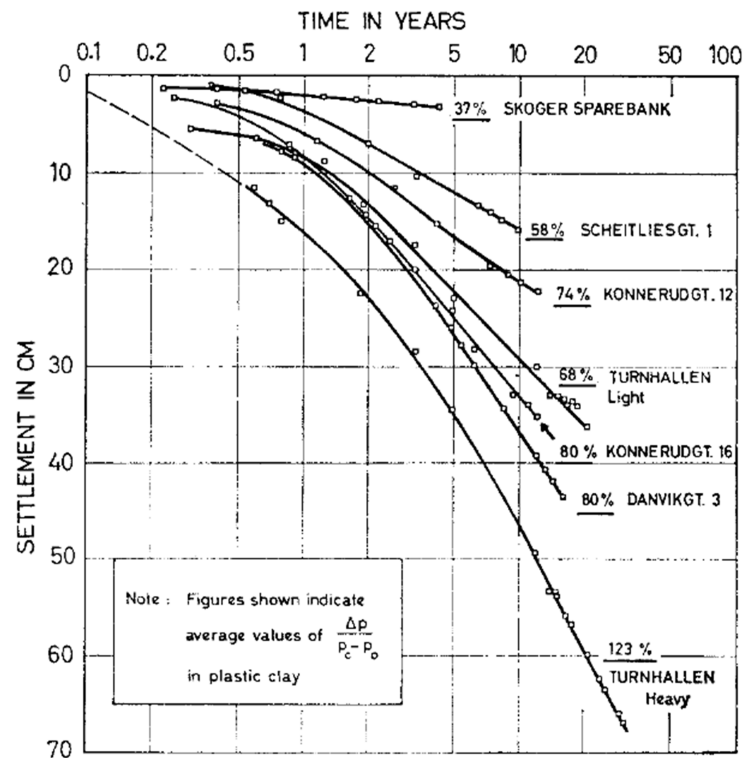


Figure 2.2: Settlement versus time of six building in Drammen (figure from [1])

(see for example [26, 1, 9, 10, 11]). Drained or undrained oedometer and triaxial tests are often used in the laboratory to observe time-dependent behaviour of geomaterials. Oedometer CSR and creep tests were conducted by Lerouel et al. [2] on clay samples. The CSR tests on Batiscan clay showed that greater strain rate results in higher effective stress and larger excess pore pressure measured at the base of the specimen, Fig 2.3. The creep tests on Batiscan clay for different stress levels (from 67 kPa to 151 kPa) showed that strain increases with time and higher stresses result to a steeper $\varepsilon$-$log_t$ curve, see Fig 2.4; the slope of the curve initially increases and then decreases. This result is consistent with later observations

21
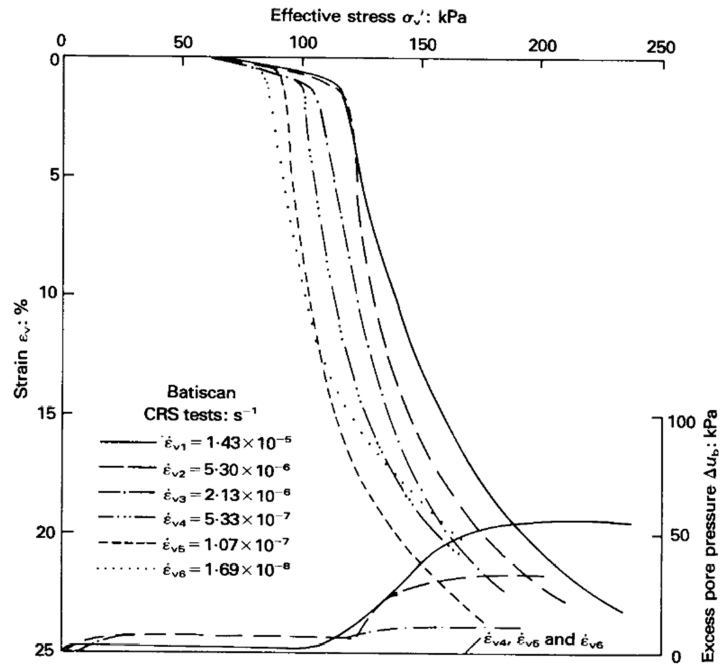
Figure 2.3: Oedometer CSR tests on Batiscan clay (figure from [2])

for soft soils in one-dimensional tests [27].

Triaxial experiments are also used in laboratory to evaluate the viscous behaviour of soft
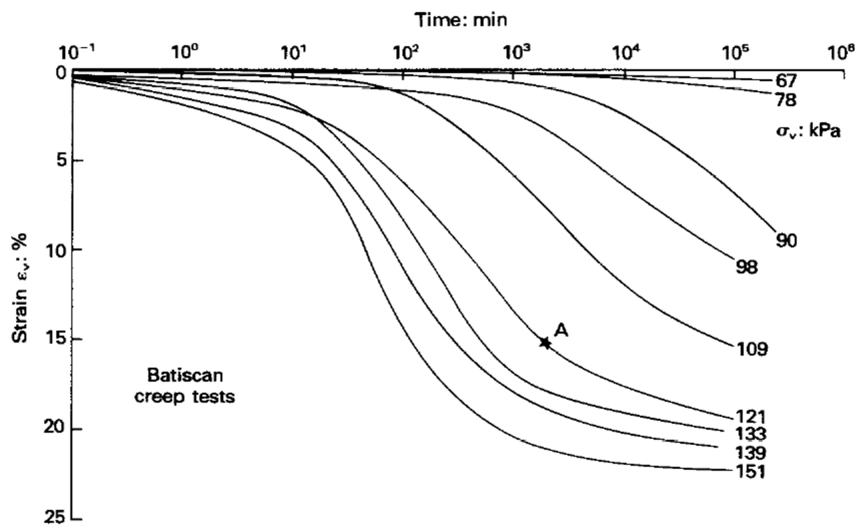


Figure 2.4: Oedometer creep tests on Batiscan clay (figure from [2])

soils. CSR, creep and stress relaxation tests under undrained triaxial condition on Hong Kong Marine Deposits (HKMD) were investigated by Zhu [3]. Results of the CSR tests are given in Fig 2.5. The increase of strain rate leads to an increase of the peak shear stress and to higher pore pressure in compression tests.

In the stress relaxation tests of Zhu [3], the samples were firstly sheared under a certain



(a) Axial strain versus deviatoric stress



(b) Axial strain versus pore pressure
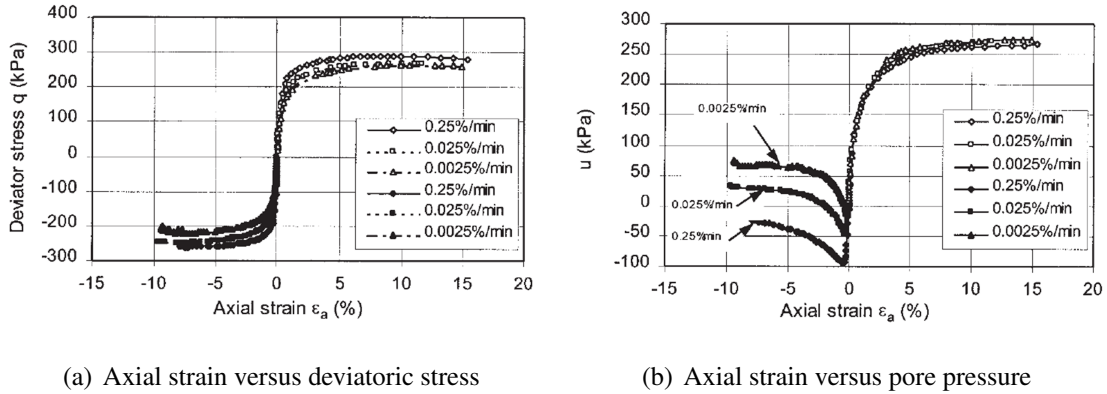
Figure 2.5: CSR undrained triaxial tests of Hong Kong marine deposits (figure from [3])

imposed strain rate (denoted $\dot{\varepsilon}_a$) to a given final strain ($\varepsilon_a$), which was then held constant to observe the stress evolution. Six samples were tested for various combinations of $\dot{\varepsilon}_a$, $\varepsilon_a$ and confining pressures ($\sigma'_h$). The parameters measured at the beginning of the relaxation tests are given in Table 2.1. Fig 2.6 presents the scatter plot of the experimental results and the fitting curves. During the tests, deviatoric stresses decreased with time.

Table 2.1: Parameters measured at the beginning of the relaxation tests of Hong Kong marine deposits (data from [3])

| Test label | $\sigma'_h$ | $\varepsilon_a$ | $\dot{\varepsilon}_a$ | $\Delta u / \sigma'_h$ |
|---|---|---|---|---|
| CUC1 | 200 | 7.3 | 0.001 | 0.015 |
| CUC5 | 400 | 17.1 | 0.025 | 0.017 |
| CUC8 | 200 | 25.0 | 0.41 | 0.054 |
| CUE9 | 400 | 9.5 | 0.0025 | 0.123 |
| CUE5 | 200 | 10.7 | 0.025 | 0.097 |
| CUE8 | 400 | 11.1 | 0.25 | 0.080 |

Note: CUC and CUE correspond to compression and extension tests respectively.

Additional tests can be also performed to characterize the viscous behaviour. For example, multi-stage loading tests and controlled gradient tests in oedometer devices on clay samples were performed by [2]. A series of undrained triaxial tests under cyclic loadings on
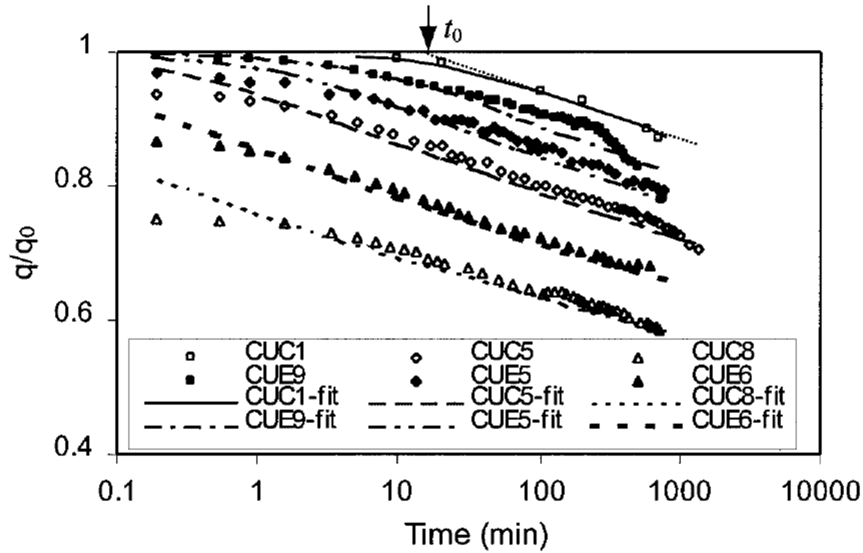
Figure 2.6: Stress relaxation undrained triaxial tests of Hong Kong marine deposits (figure from [3])

compacted clay were done by [11].

The physical explanation of these time-dependent phenomena in laboratory and in field is however rather unclear, especially concerning what happens at the microscopic scale of a clayey soil. Several interpretations have been proposed in the literature. A first proposal is that secondary consolidation is due to friction at inter-particle contacts, which occurs both during primary and secondary consolidation, becoming the predominant effect during this last phase of the process [28]. An alternative interpretation explains the phenomenon in terms of diffusive or advective pore-water transport at the scale of the pores [29, 30, 31].

Several macro-scale laws can be used to simulate this behaviour: semi-empirical approaches and rheological models [32] or elasto-viscoplastic models [9, 33, 34]. Similar approaches can also adopted to simulate strength degradation induced by pore pressure variations. The idea is that softening may not only be attributed to loss of cohesion or to reduction of the friction angle but also to pore pressure built-up.

## 2.1.2 Time-dependent behaviour of sand

The mechanical behaviour of sand is usually considered to be time-independent. Moreover, compared to soft soils, there are relatively few experimental results concerning its viscous behaviour. Nevertheless, the response of sand to external loadings evolves, generally within minutes [35]. This behaviour has been proven in several experiments [36, 37, 38], from

laboratory to in-situ tests.

As reported by Herve et al. [36], the time-dependent behaviour of clean sands (Hostun and Toyoura sands) was investigated under drained plane strain compression tests. A viscous behaviour was more pronounced a) when the strain rate was changed stepwise b) under creep and stress relaxation conditions c) during a constant strain rate followed by a creep phase just after the beginning of the loading. For a scaling loading rate factor less than $500$, no viscous behaviour was observed.

Under drained triaxial condition, creep, relaxation and stepwise strain rate tests were also performed on loose and dense air-dried Hostun sand [37]. For strains varying between $10^{-5}$ m/m and $10^{-3}$ m/m, the general trends of Fig 2.1 were observed.

Due to the fact that viscous effects are negligible in CSR sand tests, creep and stress relaxation tests are more commonly used to evaluate the time dependent behaviour of sand [22].

## 2.2 Modeling time-dependent behaviour

### 2.2.1 Constitutive models

The models developed to simulate the time-dependent behaviour can be classified into three categories, empirical models, rheological models and rate dependent constitutive laws [32]. The empirical models are generally obtained by fitting experimental data, for example the Singh and Mitchell's Creep Model [39], where a general relation between strain rate and time is presented as follows

$$\dot{\varepsilon}_1 = A e^{\bar{\alpha}\bar{q}} \left( \frac{t_i}{t} \right)^m \tag{2.1}$$

where $\bar{\alpha} = \alpha q_{\max}$, $\bar{q} = q/q_{\max}$, $q$ denotes the deviatoric stress and therrefore $q_{\max}$ is the deviatoric stress at the beginning of the creep process; parameters $A$, $\alpha$ and $m$ can be determined from ordinary creep tests. Based on Singh and Mitchell's Creep Model and make use of the relation between creep and stress relaxation tests, the Lacerda and Houston's Relaxation Model was developed [40]. The deviatoric stress $q$ is observed to decrease with time, whose evolution is given by

$$\frac{q}{q_0} = 1 - s \log \left( \frac{t}{t_0} \right) \tag{2.2}$$

where $q_0$ is the deviatoric stress at time $t_0$, $s$ is the slope of the relaxation curve in a $q/q_0$-$log(t)$ diagram. Analogously, there are several other empirical models derived from the observed testing data, for example, the Strain Rate model proposed by Leroueil et al. [41], incorporating empirical models in elastic viscous plastic constitutive relations [42, 43]. However, due to their simplicity, their applications to boundary value problems are limited.

Rheological models were initially used to describe the viscous behaviour of fluids and metals. Three well-known models are the Maxwell model, the Kelvin–Voigt model and the Bingham model, illustrated in Fig 2.7 and in Table 2.2. Despite the difficulty to extend them in 2D or 3D they are often used as they enable to understand more intuitively the viscous properties. Rate dependent constitutive laws and more specifically elasto-viscoplastic mod-



(a) Maxwell model          (b) Kelvin–Voigt model

(c) Bingham model
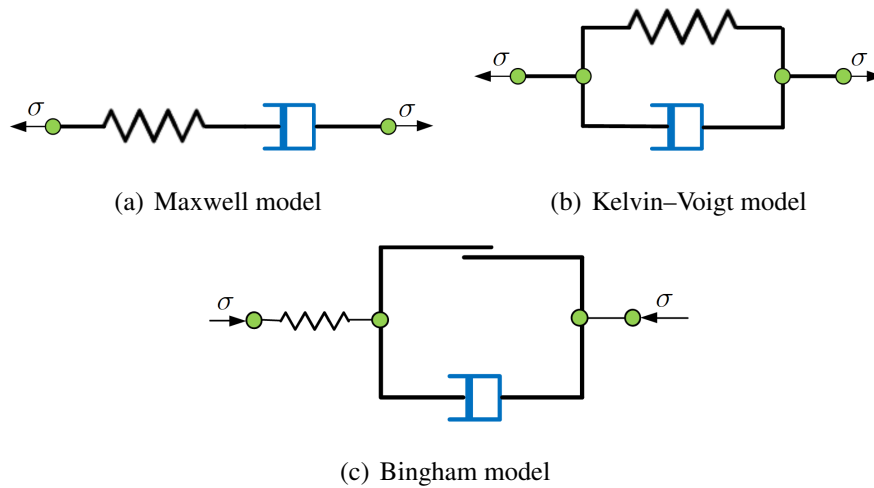
Figure 2.7: Rheological models

els can be divided in two kinds. The ones based on the overs-stress theory (Perzyna [26] and Duvaut-Lions [44] overstress models) and consistency models [45, 46, 47] based on the classical elasto-plastic theory adopting a yield surface with time related factors. They are easily implemented in finite element codes and can be used for boundary value 3D problems under complex stress paths. They are detailed in the following section.

## 2.2.2 Elasto-viscoplastic models

Three elasto viscoplastic constitutive models, the Perzyna, the Duvaut-Lions and the consistency model are briefly summarized hereafter. The two former are known as overstress models due to the fact that the stress state can stay outside the yield surface. Furthermore, the plastic strain is explicitly defined in overstress models while consistency models use the

Table 2.2: The different components of the rheological models

| / | Linear spring | Viscous dashpot | Plastic slider |
|---|---|---|---|
| Component |  |  |  |
| $\sigma - \varepsilon$ plot |  |  |  |
| $\sigma - \varepsilon$ relation | $\sigma^e = E\varepsilon^e$ | $\sigma^v = \eta\varepsilon^v$ | $\langle \sigma - \sigma^y \rangle = \begin{cases} \sigma - \sigma^y & \sigma > \sigma^y \\ 0 & \sigma \leqslant \sigma^y \end{cases}$ |
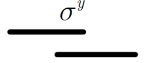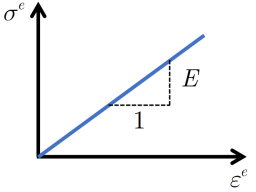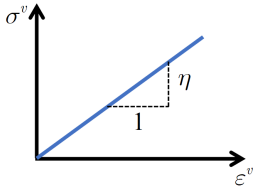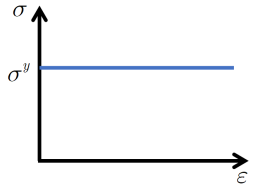
Note: Subscripts $e$ and $v$ denote elasticity and viscous behavior respectively, $E$ the Young's modulus, $\eta$ the viscosity, $\sigma^y$ the yield stress.

consistency condition.

In small strain viscoplasticity, the following additive decomposition of total strain $\varepsilon$ is considered:

$$\dot{\varepsilon} = \dot{\varepsilon}^e + \dot{\varepsilon}^{vp} \tag{2.3}$$

where $\dot{\varepsilon}^e$ denotes the elastic strain rate and $\dot{\varepsilon}^{vp}$ is the viscoplastic strain rate.

**Perzyna model**

The viscoplastic strain rate in the Perzyna model [48, 26] is given as:

$$\dot{\varepsilon}^{vp} = \frac{1}{\eta} < \Phi(f) > \frac{\partial g}{\partial \sigma} \tag{2.4}$$

where $\eta$ is the viscosity parameter, $g$ the potential function and $\Phi(f)$ the overstress function. Following the classical plasticity theory, an explicit expression for the plastic multiplier rate $\dot{\lambda}$ is obtained:

$$\dot{\lambda} = \frac{< \Phi(f) >}{\eta} \tag{2.5}$$

where the function $f$ depends on the current state and it is often referred to in the literature as the "dynamic" yield function (this terminology however can be misleading as no inertia forces are considered). $< \cdot >$ indicates the McCauley brackets, defined by:

$$< \Phi(f) > = \begin{cases} 0 & (\Phi(f) \leqslant 0) \\ \Phi(f) & (\Phi(f) > 0) \end{cases}$$

According to [49], the following conditions must hold true

- Initial condition: $\Phi(0) = 0$

- Continuity condition: $\Phi(f)$ is continuous in $[0, +\infty)$

- Convexity condition: $\Phi(f)$ is convex in $[0, +\infty)$

A power form is commonly adopted for the overstress function:

$$\Phi(f) = (\frac{f}{\sigma_0})^N \tag{2.6}$$

where $N \geqslant 1$ is a calibration parameter and $\sigma_0$ the initial yield stress.

**Duvaut-Lions model**

In the Duvaut-Lions overstress model [44], the viscoplastic strain rate and the hardening variable rate are determined by the difference between the states associated to the rate-dependent and the rate-independent solutions:

$$
\begin{aligned}
\dot{\varepsilon}^{vp} &= \frac{\mathbf{A}^{-1}}{\eta}(\sigma - \sigma_\infty) \\
\dot{\kappa} &= \frac{\mathbf{B}^{-1}}{\eta}(\kappa - \kappa_\infty)
\end{aligned}
\tag{2.7}
$$

where as before $\eta$ is the viscosity, $\sigma$ the stress state associated to the rate-dependent solution and $\sigma_\infty$ the stress state associated to the rate-independent solution. In the same way, $\kappa$ is the hardening variable associated to the rate-dependent solution and $\kappa_\infty$ the hardening variable associated to the rate-independent solution. The fourth-order tensor $\mathbf{A}$ defines the projection of the difference between the two stress states; two particular cases of $\mathbf{A}$ are the unit fourth-order tensor $\mathbf{I}_{ijkl}$ [44] and the elastic moduli $\mathbf{C}_{ijkl}$ [49]. For a scalar hardening parameter, $\mathbf{B}$ becomes a scalar and could be considered equal to 1.

**Consistency model**

Unlike the overstress theories, the viscoplastic consistency model does not allow the stress state to be outside the yield surface, i.e. the consistency condition of classical plasticity is satisfied [47]. In this case however, the yield function depends not only on the stress and

hardening variables but also on their time derivatives. The strain rate therefore affects the evolution of the yield surfaces (hardening, softening, size, shape). The consistency condition reads:

$$\lambda \dot{f}(\sigma, \kappa, \dot{\kappa}) = 0 \tag{2.8}$$

where $\lambda$ is the plastic multiplier, $\kappa$ and $\dot{\kappa}$ state variables dependent on the strain and strain rate.

As in classical plasticity, the plastic strain rate is defined as

$$\dot{\varepsilon}^{vp} = \dot{\lambda} \frac{\partial g}{\partial \sigma} \tag{2.9}$$

where $g$ denotes the plastic potential.

### 2.2.3 Algorithmic aspects of the elasto-viscoplastic models

Some algorithmic aspects of the numerical implementation of the elasto-viscoplastic models are detailed hereafter. For each step $n$ and at each Gauss point, the stress state is updated at time $t_{n+1}$ from the converged values of time $t_n$. The difference between the updated and the converged stress state is represented by $\Delta$, while $\delta$ is used to indicate a (local) iteration from $t_{n+1}^{(k)}$ to $t_{n+1}^{(k+1)}$ in the Newton-Raphson loop. The generalized midpoint rule is adopted so that the increment of the viscoplastic strain is approximated as

$$\begin{aligned} \varepsilon_{n+1}^{vp} &= \varepsilon_n^{vp} + \Delta t \dot{\lambda} \left( \varepsilon_{n+\theta}^{vp} \right) \\ \varepsilon_{n+\theta}^{vp} &= \theta \varepsilon_{n+1}^{vp} + (1 - \theta) \, \varepsilon_n^{vp} \end{aligned} \tag{2.10}$$

in which $\theta$ ranges from 0 to 1. Depending on the value $\theta$, the following three well-known algorithms can be retrieved:

- $\theta = 0$, forward (explicit) Euler

- $\theta = 0.5$, midpoint rule

- $\theta = 1$, backward (implicit) Euler

According to [50] the algorithm is unconditionally stable for $\theta \geqslant 0.5$. Therefore, the implicit Euler method is adopted to preserve stability, we have

$$\Delta \varepsilon_{n+1}^{vp} = \Delta \lambda_{n+1} \frac{\partial g}{\partial \sigma} |_{n+1} \tag{2.11}$$

If we omit the time step indicator $n + 1$ in the subscript, as in classical plasticity, equation (2.11) turns into

$$\Delta\varepsilon^{vp} = \Delta\lambda\frac{\partial g}{\partial\sigma} \tag{2.12}$$

The incremental stress is related to the elastic strain increment as:

$$\Delta\sigma = \mathbf{C}(\Delta\varepsilon - \Delta\varepsilon^{vp}) \tag{2.13}$$

The internal variable $\kappa$ is a function of the plastic multiplier:

$$\kappa = \kappa(\lambda) \tag{2.14}$$

**Perzyna model**

Since the consistency condition is no more valid for the Perzyna overstress model, the plastic multiplier is constrained by the residual function as shown in equation (2.15)

$$r_{resi} = \eta\frac{\Delta\lambda}{\Delta t} - \Phi(f) \tag{2.15}$$

Assume that the constraint equation is satisfied at iteration $k + 1$, the Taylor series expansion implies:

$$r^{k+1} = r^k + \eta\frac{\delta\lambda}{\Delta t} - \left(\frac{\partial\Phi(f)}{\partial\sigma}\right)^T\delta\sigma - \frac{\partial\Phi(f)}{\partial\lambda}\delta\lambda = 0 \tag{2.16}$$

Differentiation of the equation (2.13) leads to

$$\delta\sigma = \mathbf{H}\left[\delta\varepsilon - \left(\Delta\lambda\frac{\partial^2 g}{\partial\sigma\partial\lambda} + \frac{\partial g}{\partial\sigma}\right)\delta\lambda\right] \tag{2.17}$$

where $\mathbf{H} = \left(\mathbf{C}^{-1} + \Delta\lambda\frac{\partial^2 g}{\partial\sigma^2}\right)^{-1}$

Substitution of equation (2.17) into equation (2.16), the viscoplastic incremental plastic multiplier in a local iteration is derived as

$$\delta\lambda^{k+1} = \frac{1}{\beta^p}\left[-r^k + \left(\frac{\partial\Phi(f)}{\partial\sigma}\right)^T\mathbf{H}\delta\varepsilon\right] \tag{2.18}$$

where $\beta^p = \left(\frac{\partial\Phi(f)}{\partial\sigma}\right)^T\mathbf{H}\left(\Delta\lambda\frac{\partial^2 g}{\partial\sigma\partial\lambda} + \frac{\partial g}{\partial\sigma}\right) + \left(\frac{\eta}{\Delta t} - \frac{\partial\Phi(f)}{\partial\lambda}\right)$

The algorithmic tangent moduli $\mathbf{C}^{ep}$ which guarantees a quadratic convergence rate could be calculated through the substitution of equation (2.18) into (2.17)

$$\mathbf{C}^{ep} = \mathbf{H} - \frac{1}{\beta^p}\mathbf{H}\left(\frac{\partial g}{\partial\sigma} + \Delta\lambda\frac{\partial^2 g}{\partial\sigma\partial\lambda}\right)\frac{\partial\Phi(f)}{\partial\sigma}\mathbf{H} \tag{2.19}$$

The algorithm is summarized in Box 2.1.

Box 2.1: Implicit algorithm for the Perzyna model

1 Compute the trial state

$\sigma_{n+1}^{tr} = \mathbf{C}\Delta\varepsilon_{n+1} + \sigma_n,\, \kappa_{n+1}^{tr} = \kappa_n$

If $f\left(\sigma_{n+1}^{tr}, \kappa_{n+1}^{tr}\right) \leq 0$

    Elastic behaviour

else:

    Plastic behaviour

        (1) Initialize the variables

        $\Delta\lambda_{n+1}^{(0)} = 0,\, \Delta\sigma_{n+1}^{(0)} = \mathbf{C}\left(\Delta\varepsilon - \Delta\lambda^{(0)}\frac{\partial g}{\partial\sigma}\right)$

        $r_{resi}^{(0)} = \eta\frac{\Delta\lambda_{n+1}^{(0)}}{\Delta t} - \Phi(f)_{n+1}^{(0)}$

        (2) Local iterations

            1) Compute local variable increment

            $\delta\lambda^{k+1} = \frac{1}{\beta^p}\left(-r^k + \left(\frac{\partial\Phi(f)}{\partial\sigma}\right)^T\mathbf{H}\delta\varepsilon\right)$

            $\Delta\lambda^{(k+1)} = \delta\lambda^{(k+1)} + \Delta\lambda^{(k)}$

            2) Update variables

            $\Delta\sigma_{n+1}^{(k+1)} = \mathbf{C}\left(\Delta\varepsilon - \Delta\lambda^{(k+1)}\frac{\partial g}{\partial\sigma}\right)$

            $\Delta\kappa_{n+1}^{(k+1)} = \Delta\kappa_{n+1}^{(k)} + \frac{\partial\kappa}{\partial\lambda}\delta\lambda_{n+1}^{(k+1)}$

            3) Compute residuals and check convergence

            $r_{resi}^{(k+1)} = \eta\frac{\Delta\lambda_{n+1}^{(k+1)}}{\Delta t} - \Phi(f)_{n+1}^{(k+1)}$

            IF $\left\|r_{resi}^{(k+1)}\right\| > Tol$

                Set $k \leftarrow k + 1$ and go to (2).

            ELSE $(\cdot)_{n+1} \leftarrow (\cdot)_{n+1}^{(k+1)}$

**Duvaut-Lions model**

In the Duvaut-Lions model, the rate-independent solution should be first calculated and thus $\sigma_\infty$ and $\kappa_\infty$. The viscoplastic strain increment is expressed as (using equations (2.7) and (2.13))

$$\Delta\varepsilon_{n+1}^{vp} = \frac{\frac{\Delta t}{\eta}\left(\Delta\varepsilon - \mathbf{C}^{-1}\Delta\sigma\right)}{1 + \frac{\Delta t}{\eta}} \tag{2.20}$$

The viscoplastic stress becomes

$$\sigma_{n+1} = \frac{\sigma_n + \mathbf{C}\Delta\varepsilon + \frac{\Delta t}{\eta}\bar{\sigma}_{n+1}}{1 + \frac{\Delta t}{\eta}} \tag{2.21}$$

and the hardening parameter $\kappa_{n+1}$ is obtained as follows

$$\kappa_{n+1} = \frac{\kappa_n + \frac{\Delta t}{\eta}\bar{\kappa}_{n+1}}{1 + \frac{\Delta t}{\eta}} \tag{2.22}$$

The algorithm of Duvaut-Lions model is given Box 2.2.

Box 2.2: Implicit algorithm for the Duvaut-Lions model

---

1 Compute the trial state

$\sigma_{n+1}^{tr} = \mathbf{C}\Delta\varepsilon_{n+1} + \sigma_n,\ \kappa_{n+1}^{tr} = \kappa_n$

If $f\left(\sigma_{n+1}^{tr}, \kappa_{n+1}^{tr}\right) \leq 0$

    Elastic behaviour

else:

    Plastic behaviour

        (1) Compute the rate-independent solution

        $\sigma_\infty, \kappa_\infty$

        (2) Update the viscoplastic stress and hardening variable

        $\sigma_{n+1} = \frac{\sigma_n + \mathbf{C}\Delta\varepsilon + \frac{\Delta t}{\eta}\bar{\sigma}_{n+1}}{1 + \frac{\Delta t}{\eta}}$

        $\kappa_{n+1} = \frac{\kappa_n + \frac{\Delta t}{\eta}\bar{\kappa}_{n+1}}{1 + \frac{\Delta t}{\eta}}$

Set $n \leftarrow n + 1$ and go to 1.

---

**Consistent viscoplastic model**

Assuming that the consistency condition is satisfied at iteration $k + 1$, the Taylor series expansion implies:

$$f^{(k+1)} = f^{(k)} + \frac{\partial f}{\partial \sigma}\delta\sigma + \frac{\partial f}{\partial \lambda}\delta\lambda + \frac{\partial f}{\partial \dot{\lambda}}\delta\dot{\lambda} = 0 \tag{2.23}$$

where $\frac{\partial f}{\partial \lambda}\delta\lambda = \frac{\partial f}{\partial \kappa}\frac{\partial \kappa}{\partial \lambda}\delta\lambda$, $\frac{\partial f}{\partial \dot{\lambda}}\delta\dot{\lambda} = \frac{\partial f}{\partial \dot{\kappa}}\frac{\partial \dot{\kappa}}{\partial \dot{\lambda}}\delta\dot{\lambda}$.

Assuming an associated flow rule where the plastic potential $g$ is equal to $f$ and differentia-

tion of equation (2.13) leads to the local stress increment $\delta\sigma$:

$$\delta\sigma = \mathbf{H}\delta\varepsilon - \mathbf{H}\left[\frac{\partial g}{\partial\sigma} + \Delta\lambda\frac{\partial^2 g}{\partial\sigma\partial\lambda} + \frac{\Delta\lambda}{\Delta t}\frac{\partial^2 g}{\partial\sigma\partial\dot{\lambda}}\right]\delta\lambda \qquad (2.24)$$

where $\mathbf{H} = \left(\mathbf{C}^{-1} + \Delta\lambda\frac{\partial^2 g}{\partial\sigma^2}\right)^{-1}$ and the term $\delta\varepsilon$ vanishes during the local iteration due to a fixed total strain increment $\Delta\varepsilon$.

The combination of equation (2.23) and equation (2.24) provides the local increment of the plastic multiplier:

$$\delta\lambda = \frac{1}{\beta}\left[f^{(k)} + \left(\frac{\partial f}{\partial\sigma}\right)^T\mathbf{H}\delta\varepsilon\right] \qquad (2.25)$$

where $\beta = \left(\frac{\partial f}{\partial\sigma}\right)^T\mathbf{H}\left(\frac{\partial g}{\partial\sigma} + \Delta\lambda\frac{\partial^2 g}{\partial\sigma\partial\lambda} + \frac{\Delta\lambda}{\Delta t}\frac{\partial^2 g}{\partial\sigma\partial\dot{\lambda}}\right) - \frac{\partial f}{\partial\lambda} - \frac{1}{\Delta t}\frac{\partial f}{\partial\dot{\lambda}}$

The derivation of the consistent tangent moduli $\mathbf{C}^{ep}$ is important as it results to a quadratic convergence rate in a finite element analysis [51, 52] and it is needed to calculate the determinant of the acoustic tensor used in section 3.3. Substituting equation (2.25) into equation (2.24), the consistent tangent moduli reads:

$$\mathbf{C}^{ep} = \mathbf{H} - \frac{1}{\beta}\mathbf{H}\left(\frac{\partial g}{\partial\sigma} + \Delta\lambda\frac{\partial^2 g}{\partial\sigma\partial\lambda} + \frac{\Delta\lambda}{\Delta t}\frac{\partial^2 g}{\partial\sigma\partial\dot{\lambda}}\right)n^T\mathbf{H} \qquad (2.26)$$

The algorithm is summarized in Box 2.3.

Box 2.3: Implicit algorithm for the consistency viscoplastic model

---

1 Compute the trial state

$$\sigma_{n+1}^{tr} = \mathbf{C}\Delta\varepsilon_{n+1} + \sigma_n, \ \kappa_{n+1}^{tr} = \kappa_n, \ \dot{\kappa}_{n+1}^{tr} = \dot{\kappa}_n$$

If $f\left(\sigma_{n+1}^{tr}, \kappa_{n+1}^{tr}, \dot{\kappa}_{n+1}^{tr}\right) \leq 0$

      Elastic behaviour

else:

      Plastic behaviour

            (1) Initialize the variables

            $\Delta\kappa_{n+1}^{(0)} = 0, \ \Delta\dot{\kappa}_{n+1}^{(0)} = \frac{\Delta\kappa_{n+1}^{(0)}}{\Delta t}, \ \Delta\sigma_{n+1}^{(0)} = \mathbf{C}\left(\Delta\varepsilon - \Delta\lambda^{(0)}\frac{\partial g}{\partial\sigma}\right)$

            $R^{(0)} = f\left(\sigma_n + \Delta\sigma_{n+1}^{(0)}, \kappa_n + \Delta\kappa_{n+1}^{(0)}, \dot{\kappa}_n + \Delta\dot{\kappa}_{n+1}^{(0)}\right)$

            (2) Local iterations

                1) Compute local variable increment

                $\mathbf{H}^{(k)} = \left(\mathbf{C}^{-1} + \Delta\lambda^{(k)}\frac{\partial^2 g}{\partial\sigma^2}\right)^{-1}$

                $\beta^{(k)} = n^T\mathbf{H}^{(k)}\left(\frac{\partial g}{\partial\sigma} + \Delta\lambda\frac{\partial^2 g}{\partial\sigma\partial\lambda} + \frac{\Delta\lambda}{\Delta t}\frac{\partial^2 g}{\partial\sigma\partial\dot{\lambda}}\right)^{(k)} - \left(\frac{\partial f}{\partial\lambda} - \frac{1}{\Delta t}\frac{\partial f}{\partial\dot{\lambda}}\right)^{(k)}$

                $\delta\lambda^{(k)} = \frac{f^{(k)}}{\beta^{(k)}}$

                $\Delta\lambda^{(k+1)} = \delta\lambda^{(k+1)} + \Delta\lambda^{(k)}$

                2) Update variables

                $\Delta\sigma_{n+1}^{(k+1)} = C\left(\Delta\varepsilon - \Delta\lambda^{(k+1)}\frac{\partial g}{\partial\sigma}\right)$

                $\kappa_{n+1}^{(k+1)} = \kappa_{n+1}^{(k)} + \frac{\partial\kappa}{\partial\lambda}\delta\lambda^{(k)}$

                3) Compute residuals and check convergence

                $R^{(k+1)} = f\left(\sigma_n + \Delta\sigma_{n+1}^{(k+1)}, \kappa_{n+1}^{(k+1)}, \dot{\kappa}_{n+1}^{(k+1)}\right)$

                IF $\left\|R^{(k+1)}\right\| > Tol$

                    Set $k \leftarrow k + 1$ and go to (2).

                ELSE $(\cdot)_{n+1} \leftarrow (\cdot)_{n+1}^{(k+1)}$.

## 2.3 Experimental results of strain localization of geomaterials

Strain localization has been intensively experimentally studied the last thirty years. The following points are of particular interest: the time when strain localization occurs, the thickness, orientation and evolution of the localized zone and their influencing factors (e.g. loading rate, loading path). Several experimental techniques have been employed to detect strain localization [53, 54], for instance, Computed Tomography (CT), Scanning Electronic Microscopy (SEM), etc. Particular aspects of strain localization in soft soils and sand are detailed hereafter.

### 2.3.1 Strain localization of soft soils

Concerning work on strain localization of soft soils, investigations have been conducted, where characteristics of shear band and their influencing factors, e.g. the loading rate, the loading conditions, the sample shape, are analyzed.

We refer to, for instance, [55]. In this paper, the thickness and orientation of the shear band were found to depend on the applied strain rates, which are from fast to slow $5$ mm/min, $0.5$ mm/min, $0.05$ mm/min, $0.005$ mm/min. Effect on shear band formation was more pronounced under higher rates as no evident shear band was visible for the slowest one $0.005$ mm/min . Increasing the loading rate may increase the inclination angle of the shear band and decrease its thickness [56]. Several possible explanations can be assumed, like the generation and dissipation of excess pore pressure, microstructural changes and interparticle sliding [55]. In their experiments, large strain rates form localized strains while diffused strains are induced by small strain rates. For intermediate values, a switch mode seem to exist.

Moreover, the influence of testing conditions was also investigated by Hicher et al. [57] (drained and undrained triaxial compression tests). Compared with the region outside the shear band, the density in the localized region was larger for a normally consolidated sample and smaller for an overconsolidated clay. Shear band orientation stayed constant for a given clay irrespective of the sample sizes, end conditions (with or without lubrication) or overconsolidation ratios (between 1 and 10). The homogeneity, the onset and development

of shear band were however greatly influenced by the testing conditions.

Several shear band shapes were observed during the experiments. Single, 'X', wedge and sub-single types [4], Fig 2.8. Samples with larger aspect ratio were more likely to show buckling-like mode, whereas samples with smaller aspect ratio an 'X' mode (two shear bands developed along the edge of the top or the bottom intercross each other) [58].

The shear band evolution was recorded in a series of undrained plane strain tests of Nor-



|  (a) Single  |  (b) X  |  (c) Wedge  |  (d) Sub-single  |
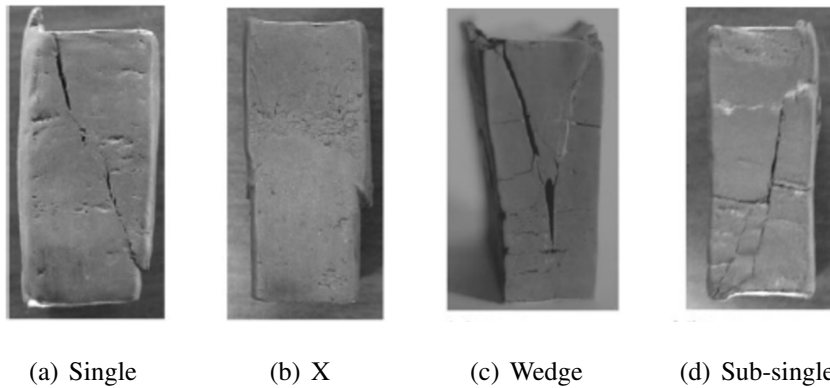
Figure 2.8: Image of four shear band types of Shanghai silty clay (figure from [4])

wegian quick clays [5]. As seen from Fig 2.9, shear bands initiated locally and developed in a 'X' mode until dividing the specimen into several sub-zones. The shear band thickness evolved during the whole process.

The process of shear band formation and evolution is very complex and the induced physical mechanism is not very well understood, therefore its evaluation is still an open as well as a chanlenging issue. Typically, shear band thickness for soft soils is from $10~\mu$m to $20$ mm [59], which is many times the diameter of individual clay particle (mostly less than 0.002 mm). A distinct shear band of 3 mm thick was observed for Norwegian quick clay under undrained plane strain conditions [6], see Fig 2.10. It was also interesting to find that the orientation of the shear band varied along the band. In the upper left corner, orientation was about $40°$ and it increased towards the center to a maximum value of about $53°$. Another similar research on Norwegian quick clay, a 2-3 mm thick shear band with an orientation of $52°$ was recorded through cutting the samples after the test [60]. Localized deformation was also monitored for very sensitive Scandinavian soft clay under undrained plane strain condition, where shear band thickness was measured approximately to be 18 mm; shear band orientation to the horizontal plane was around $53°$. Except for soft sensitive clays, under drained and undrained triaxial conditions, observations at the particle level [57] showed the
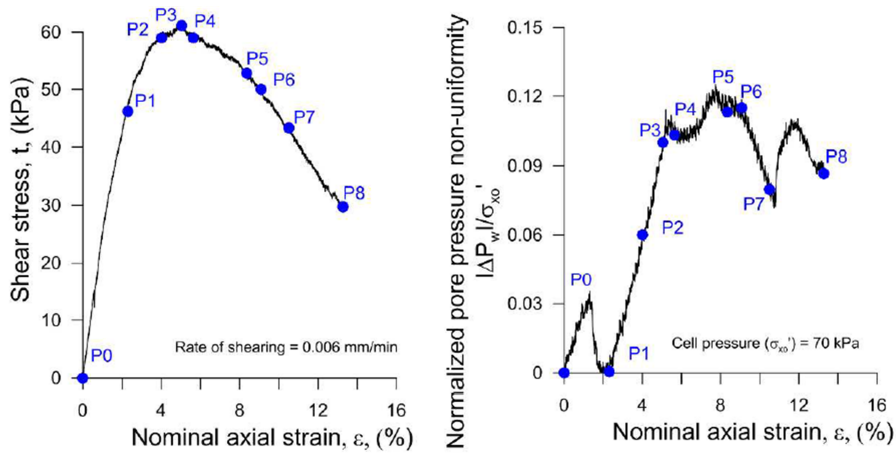
(a) Shear stress versus deformation

(b) Pore pressure versus deformation
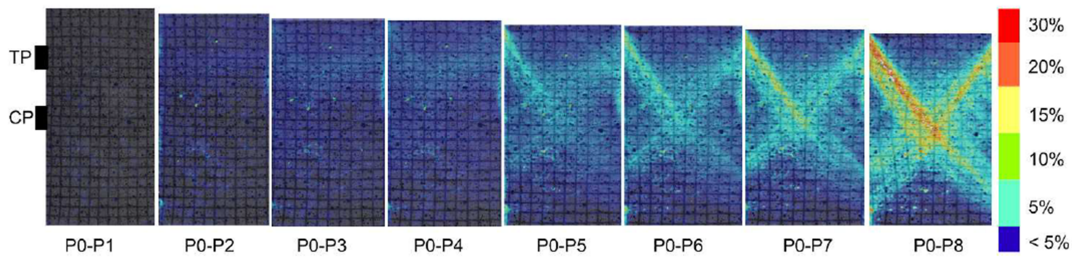


(c) Total strain at different selected stages

Figure 2.9: DIC results in undrained plane strain tests of Norwegian quick clays (figure from [5])
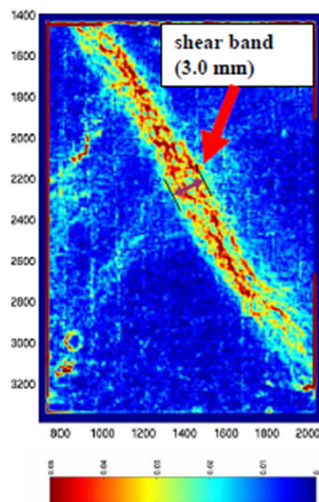


Figure 2.10: Shear band measured for Norwegian quick clay under undrained plane strain conditions (figure from [6])

mean thickness of an overconsolidated sample of Kaolinite was 3.3 mm in the early stage and then increased to 5.3 mm. Values of measured thickness for Bentonite was found to lie in a range from 2 mm to 7 mm.

### 2.3.2 Strain localization of sand

A series of biaxial experiments were conducted on fine, medium and coarse-grained uniform silica sand [61]. Strains were monitored and analyzed by means of a grid pattern imprinted on the latex membrane. It was found out that the specimen density, confining pressure, grain texture and the resulting failure mode influenced its overall stress-strain behaviour.

Under drained and undrained conditions, plane strain experiments were performed on loose masonry sand. Shear band formation was found and a persistent localization mode progressively took the place of macroscopically uniform deformation [53]. The average volume of the shear band remained constant while local variations of volumetric strain existed within the band.

Various patterns of strain localization can appear in sand: single, crossing shear, parallel and 'non-persistent' (temporary) modes, see Fig 2.11. Parallel and crossing shear bands depend on the boundary conditions and the specimen's aspect ratio [7]. As suggested by Muhlhaus



(a) Single shear band

(b) Crossing shear bands

(c) Parallel shear bands
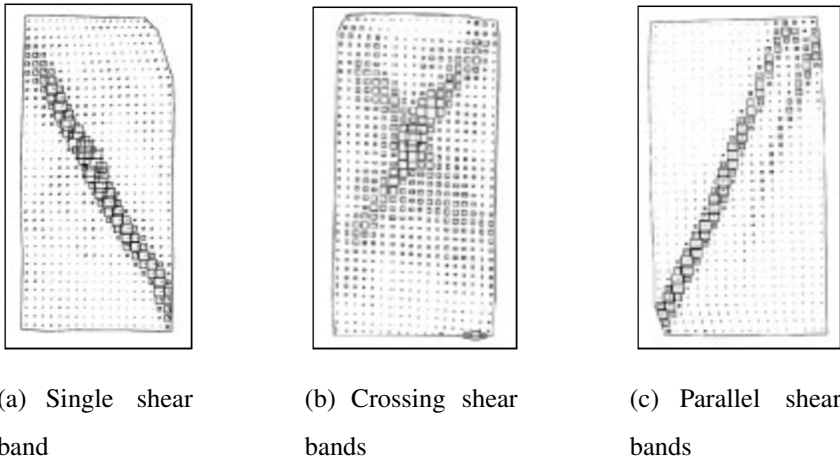
Figure 2.11: Stereophotogrammetry-based shear strain intensity of loose sand (figure from [7])

and Vardoulakis [62], the thickness of the shear band in granular materials is $8$ to $10$ times the mean grain size. Richard et al. [53] presented experimental tests which characterized the

behaviour of loose sand under drained and undrained plane strain condition. Shear bands were observable for all testing conditions and their thicknesses varied from 10 to 25 times the mean grain diameter and their orientations were measured to be from 55° to 65°.

## 2.4 Few remarks on uniqueness and bifurcation

In the following section we briefly review the literature results concerning the uniqueness of the solution of the (visco-) plastic problem i.e. the rate form of the governing equations endowed with a (visco-) plastic constitutive law. In particular, sufficient conditions describing the loss of uniqueness of the solution and consequently the showing up of multiple (bifurcated) solutions are reminded. Then we focus on a plane strain problem and on the algorithm to search for multiple solutions.

### 2.4.1 Theory of uniqueness

Following the classical argument adopted by Kirchoff to prove the uniqueness theorem in the framework of small strain elasticity, a sufficient condition for uniqueness of the non-linear (visco-) plastic problem is provided by the second-order work ([63, 64]):

$$\int_V \Delta\dot{\sigma} : \Delta\dot{\varepsilon}\, dV > 0 \tag{2.27}$$

where $\Delta\dot{\sigma}$ satisfy equilibrium and homogeneous traction boundary conditions on that part of the boundary where natural boundary conditions are prescribed, while $\Delta\dot{\varepsilon}$ verifies homogeneous conditions on that part of the boundary where essential boundary conditions are given. In this paper, focus is put on the global level, one of interest in local investigation can refer to [65]. When the constitutive operator $\mathbf{C}$ can be defined, as for the case of rate independent plasticity or of the consistency viscoplastic model, $\mathbf{C} = \mathbf{C}^{ep}$ and $\Delta\dot{\sigma} = \mathbf{C}\dot{\varepsilon}_1 - \mathbf{C}\dot{\varepsilon}_2$ coincides with $\mathbf{C}(\Delta\dot{\varepsilon})$. A local sufficient condition resulting from equation (2.27) is that for each $x \in V$ and for each $\Delta\dot{\varepsilon} \neq 0$:

$$\Delta\dot{\sigma} : \Delta\dot{\varepsilon} > 0 \tag{2.28}$$

which implies that the constitutive operator $\mathbf{C}$ is required to be positive definite.

Starting from equations (2.27) and (2.28), exclusion of bifurcation fails to hold when the

positive definiteness of the constitutive operator $\mathbf{C}$ is lost, that is when at least one tensor $X \neq 0$ exists such that:

$$X \cdot \mathbf{C}[X] = 0 \tag{2.29}$$

Equation (2.29) does not mean that $\mathbf{C}$ is necessarily singular as in the general case of non-associative plasticity one can verify equation (2.29) even if $\mathbf{C}[X] \neq 0$, see [64]. Therefore, loss of positive definiteness does not necessarily imply bifurcation. Conversely the non singularity condition of the constitutive operator $\mathbf{C}$ can be written as:

$$\mathbf{C}[X] \neq 0 \tag{2.30}$$

for every tensor $X \neq 0$.

It is clear that failing to satisfy (2.30) is critical for the bifurcation of the homogeneous solution.

Consider now the so called (semi-) strong ellipticity conditions for the constitutive operator $\mathbf{C}$, say

$$g \cdot \mathbf{C}[g \otimes n]n \geq 0, \forall n \in V, \quad \|n\| = 1 \quad \text{and} \quad g \neq 0 \tag{2.31}$$

which may be expressed, in a different notation, as the positive (semi-)definiteness of the acoustic tensor $A(n)$

$$gA(n)g = g\mathbf{C}[g \otimes n]n \geq 0 \tag{2.32}$$

It is possible to prove [66] that when the inequality (2.32) is not satisfied during a loading program of a generic boundary value problem, the sufficient condition (2.27) does not hold. As in the previous discussion about the constitutive operator $\mathbf{C}$, when condition (2.32) fails the acoustic tensor can still be non-singular. A similar non singularity condition as that of equation (2.30) for the constitutive operator can be introduced for the acoustic tensor, the so-called ellipticity condition:

$$det A(n) \neq 0, \forall n \in V, \|n\| = 1 \tag{2.33}$$

It is also possible to prove that failure of ellipticity describes a shear band formation, i.e. strain localization into a planar band, as sketched in Fig 2.12 [67]. In plane strain case, the direction $n$ normal to the shear band can be expressed as

$$n = \begin{bmatrix} \sin \theta \\ \cos \theta \end{bmatrix} \tag{2.34}$$

where $\theta$ is prescribed to be the angle between $n$ and x-axis and let $z = \tan\theta$. Then the determinant of the acoustic tensor becomes according to Ortiz [68]:

$$\det(A) = a_4 z^4 + a_3 z^3 + a_2 z^2 + a_1 z^1 + a_0 \tag{2.35}$$

with $a_0, a_1, a_2, a_3, a_4$ defined in terms of the constitutive tangent moduli:

$$a_0 = \mathbf{C}_{1111}\mathbf{C}_{1212} - \mathbf{C}_{1112}\mathbf{C}_{1211}$$

$$a_1 = \mathbf{C}_{1111}\mathbf{C}_{1222} + \mathbf{C}_{1111}\mathbf{C}_{2212} - \mathbf{C}_{1112}\mathbf{C}_{2211} - \mathbf{C}_{1122}\mathbf{C}_{1211}$$

$$a_2 = \mathbf{C}_{1111}\mathbf{C}_{2222} + \mathbf{C}_{1112}\mathbf{C}_{1222} + \mathbf{C}_{1211}\mathbf{C}_{2212} - \mathbf{C}_{1122}\mathbf{C}_{1212} - \mathbf{C}_{1122}\mathbf{C}_{2211} - \mathbf{C}_{1212}\mathbf{C}_{2211}$$

$$a_3 = \mathbf{C}_{1112}\mathbf{C}_{2222} + \mathbf{C}_{1211}\mathbf{C}_{2222} - \mathbf{C}_{1122}\mathbf{C}_{2212} - \mathbf{C}_{1222}\mathbf{C}_{2211}$$

$$a_4 = \mathbf{C}_{1212}\mathbf{C}_{2222} - \mathbf{C}_{2212}\mathbf{C}_{1222}$$

$$\tag{2.36}$$
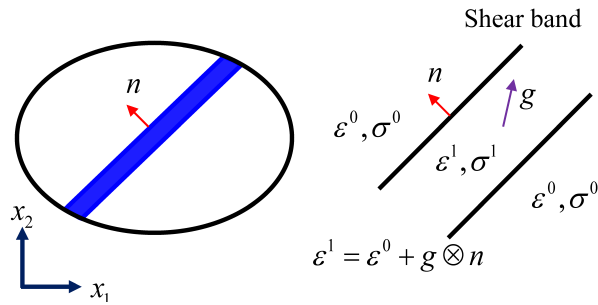


Figure 2.12: Principle scheme of a shear band

Following Bigoni [64] we can summarize the previous remarks as follows:

- the positive definiteness of the constitutive operator $\mathbf{C}$ implies the non singularity, see equation (2.28), as well as the non singularity condition (ellipticity condition) of the acoustic tensor, equation (2.33).

- the opposite is in general not true; the loss of uniqueness, characterized by violating the non-singularity condition of the constitutive operator $\mathbf{C}$ does not necessarily imply violation of the ellipticity condition of the acoustic tensor. From the physical point of view different bifurcated solutions can arise before the occurrence of shear band.

41

## 2.4.2 Algorithm for non-uniqueness search (random initialization)

For a finite element discretization of the boundary value problem, Hill's criterion (2.27) reads as:

$$\int_V \dot{\varepsilon}^T \dot{\sigma} dV = \int_V \dot{u}^T B^T \mathbf{C} \, B \, \dot{u} \, dV = \dot{u}^T \mathbf{K} \, \dot{u} > 0 \tag{2.37}$$

where $\mathbf{K} = B^T \mathbf{C} \, B$ is the global stiffness matrix, $B$ a matrix function of the finite element shape functions and $\dot{u}$ the vector of nodal velocities. Note that the boundary conditions at the beginning of section 2.4.1 must hold true. The sufficient condition (2.28) can be therefore rephrased by :

$$\dot{u}^T \mathbf{K} \, \dot{u} > 0 \tag{2.38}$$

According to Vieta's rule, equation (2.38) turns into

$$det(\mathbf{K}) = \prod_{i=1}^{n} \omega_i > 0 \tag{2.39}$$

with $\omega_i$ the eigenvalue $i$ of $\mathbf{K}$. If we restrict our attention to the non sigularity condition (2.30) we can state that bifurcation of the homogeneous solution emerges when the minimum eigenvalue of the global stiffness matrix $\mathbf{K}$ vanishes.

However as already pointed out by [69], a zero eigenvalue is hard to get due to numerical round-off errors. Perturbation techniques can be therefore used while the minimum eigenvalue is (slightly) negative to check the existence of multiple solutions (see for example [70] for a random initialization of the Newton Raphson scheme). In the following, the bifurcated solution $\Delta a$ is obtained as

$$\Delta a = \alpha \Delta a^* + \beta v_1 \tag{2.40}$$

where $v_1$ is the eigenvector corresponding to the smallest eigenvalue, $\Delta a^*$ is the homogeneous solution (or fundamental solution).

$\alpha$ and $\beta$ can be determined using different assumptions. Those made by de Borst [69] are hereafter adopted. The first assumption is that the bifurcated solution is orthogonal to the fundamental solution and therefore:

$$(\Delta a)^{\mathrm{T}} \Delta a^* = 0 \tag{2.41}$$

$\beta$ can therefore be determined as:

$$\beta = -\frac{(\Delta a)^{\mathrm{T}} \Delta a^*}{(\Delta a^*)^{\mathrm{T}} v_1} v_1 \tag{2.42}$$

42

The perturbed solution turns into:

$$\Delta a = \alpha\{\Delta a^* - \frac{(\Delta a^*)^{\mathrm{T}}\Delta a^*}{(\Delta a^*)^{\mathrm{T}}v_1}v_1\} \tag{2.43}$$

The second assumption considers that the norm of the fundamental solution and the perturbed solution are the same to avoid $(\Delta a^*)^{\mathrm{T}}v_1$ in equation (2.43) to vanish, this is written as

$$(\Delta a^*)^{\mathrm{T}}\Delta a^* = (\Delta a)^{\mathrm{T}}\Delta a \tag{2.44}$$

Finally, the bifurcated solution becomes:

$$\Delta a = \frac{1}{\sqrt{(\Delta a^*)^{\mathrm{T}}\Delta a^* - [\Delta a^*]^{\mathrm{T}}v_1]^2}}\times\{(\Delta a^*)^{\mathrm{T}}v_1\Delta a^* - (\Delta a^*)^{\mathrm{T}}\Delta a^* v_1\} \tag{2.45}$$

Other ways to determine the scalar parmaters $\alpha$ and $\beta$ can be found in [71, 72].

Depending on the chosen perturbation, numerical calculations can diverge or converge to a new solution or to the fundamental solution [73]. The procedure can be summarized as follows:

1. Choose a step in the global response curve to study if there are multiple solutions (in addition to the fundamental one)

2. Use equation (2.40) to apply the perturbation

3. Generate the perturbation coefficients $\alpha$ and $\beta$

4. Run the calculations to check if the code diverges or converges to a new solution or to the fundamental solution

5. If the code converges to a new solution, restart the calculations to illustrate the new response for the remaining time steps

The previous tools are used hereafter to verify if the introduction of rate effects restores the unicity of the solution and regularizes the problem. More specifically, a two-dimensional numerical study is presented in section 3.3.

## 2.5 Regularization techniques

Under static loading conditions, boundary value problems can result to a loss of ellipticity (or to a loss of hyperbolicity under dynamic loading conditions). Let us now focus on the case when loss of uniqueness corresponds to the showing up of localized solutions. Within the framework of classical continuum mechanics, results are no longer objective, i.e., an infinite number of solutions exist and the thickness of shear band is mesh dependent. To remedy this, regularization techniques have to be used, e.g., non-local models [13, 14, 15], gradient plasticity [16] and continua with microstructure [17, 18]. Besides, rate-dependence is sometimes mentioned in the literature as another method able to regularize the problem based on the introduction of a characteristic time rather than an intrinsic material parameter [19, 74, 20] (this last argument will be seriously questioned in this manuscript). The Extended Finite Element Method (XFEM) [75, 76] and the Assumed Enhanced Strain Method (AESM) [77] are also adopted to regularize strong discontinuity problems. A short description of several regularization techniques follows.

### 2.5.1 Nonlocal theory

The nonlocal theory has been introdyced by Pijaudier-Cabot and Bažant [13] and applied for geomaterials such as concrete [14] and soils [15]. This method is based on the spatial averaging of variables (e.g. strains); the mechanical response is not only (locally) affected by the state of the given point but also by the state of its neighbouring points.

Typical loading function formulated in terms of non-local strain is expressed as [78]

$$f\left(\bar{\varepsilon}, k\right) = \bar{\varepsilon} - k \tag{2.46}$$

where $\bar{\varepsilon}$ is the non-local strain; $k$ is the local history parameter; the non-local strain can be calculated.

$$\bar{\varepsilon}\left(\mathbf{x}\right) = \frac{1}{\psi\left(\mathbf{x}\right)} \int_V \psi\left(\mathbf{x}, \mathbf{y}\right) \bar{\varepsilon}\left(\mathbf{y}\right) dV \quad \psi\left(\mathbf{x}\right) = \int_V \psi\left(\mathbf{x}, \mathbf{y}\right) dV \tag{2.47}$$

in which $\psi\left(\mathbf{x}, \mathbf{y}\right)$ is a weight function, $\mathbf{x}$ is the position of a given point and $\mathbf{y}$ denotes the position of the infinitesimal volume $dV$. Homogeneous and isotropic assumption allows the weight function to only depend on the distance $s = \|\mathbf{y} - \mathbf{x}\|$. The challenging difficulty is to determine the radius and its evolution with loading.

## 2.5.2 Gradient plasticity models

The gradient plasticity proposed by Aifantis [16] takes into account the gradient of internal variables. If we expand the plastic strain in Taylor series and truncated after the second order term under isotropic assumption, it writes

$$\bar{\varepsilon} = \varepsilon_s + c\nabla^2\varepsilon_s \qquad (2.48)$$

where $c$ is a gradient parameter of dimension $[L^2]$, $\varepsilon_s$ is the local plastic strain. Equation (2.48) is known to be an explicit form. For both higher gradient models, additional boundary conditions have to be imposed.

## 2.5.3 Continua with microstructure

Continua with microstructure are also called micromorphic media, see the work of Germain [17] and Mindlin [18] and they accounts for the effects of intrinsic characteristic lengths. These models are in particular of interest when modeling strain localization, since classical continuum mechanics are not capable to provide an objective description of the process when a scale effect is involved. These models are characterized by an enriched kinematics able to describe micro strains and micro rotations, for instance local dilatancy and grain rotation in granular materials. An additional field $f_{ij}$ also called the microkinematic gradient is added to the classical continua. The following notations are introduced here for the two level fields.

Table 2.3: Notations for macro field and micro field

| Macro field | | Micro field | |
|---|---|---|---|
| Field | Notation | Field | Notation |
| Macro displacement | $u_i$ | / | / |
| Macro gradient | $F_{ij} = \frac{\partial u_i}{\partial x_j}$ | Micro kinematic gradient | $f_{ij}$ |
| Macro strain | $\varepsilon_{ij} = \frac{1}{2}\left(F_{ij} + F_{ji}\right)$ | Microstrain | $v_{ij} = \frac{1}{2}\left(f_{ij} + f_{ji}\right)$ |
| Macro rotation | $R_{ij} = \frac{1}{2}\left(F_{ij} - F_{ji}\right)$ | Microrotation | $r_{ij} = \frac{1}{2}\left(f_{ij} - f_{ji}\right)$ |
| / | / | Micro second gradient | $\chi_{ijk} = \frac{\partial f_{ij}}{\partial x_k}$ |

Like classical continuum, the virtual work done is still considered to be a linear form with respect to the displacement gradient, micro strain and the difference between the macro displacement gradient and microkinematic gradient, see [17]. Herein a virtual quantity is denoted with a superscript $*$. The density of virtual work is given by

$$w^* = \sigma_{ij}\varepsilon_{ij}^* + \tau_{ij}\left(f_{ij}^* - F_{ij}^*\right) + \chi_{ijk}^*\Sigma_{ijk} \tag{2.49}$$

where $\sigma_{ij}$ is the macro stress or Cauchy stress, $\tau_{ij}$ is the additive stress associated with the microstructure, $\Sigma_{ijk}$ is the double stress related with the micro second gradient $\chi_{ijk}$.

For a given body, the internal work is integrated throughout the domain $\Omega$ and becomes

$$W_{in}^* = \int_\Omega w^* d\Omega = \int_\Omega \left[\sigma_{ij}\varepsilon_{ij}^* + \tau_{ij}\left(f_{ij}^* - F_{ij}^*\right) + \chi_{ijk}^*\Sigma_{ijk}\right] d\Omega \tag{2.50}$$

As with the classical theory, no double body forces are considered, the virtual work done by the external work is consequently given by

$$W_e^* = \int_\Omega \rho_i f_i u_i^* d\Omega + \int_\Gamma \left(p_i u_i^* + P_{ij} f_{ij}^*\right) d\Gamma \tag{2.51}$$

where $f_i$ is the body force per unit mass, $\rho_i$ is the mass density, $p_i$ is the external (classical) force per unit area and $P_{ij}$ is an additional (double) force per unit area applied on a part of the boundary part $\Gamma$.

Based on different mathematical constraints, the micromophic model could be simplified into different models, among them, Cosserat model and second gradient model will be presented here.

(1) Cosserat model

In Cosserat theory, some kinematic constraint is applied to let the micro strain vanish following the work of Germain (1973a) [79] and Mühlhaus, where the microkinematic gradient $f_{ij}$ is antisymmetric and equal to its rotation $r_{ij}$. This assumption is applicable to granular materials with rigid grains according to the findings of Calvetti et al. [80] and Matsushima et al.[81]. The internal work of equation (2.50) could be rewritten into the following form.

$$W_{in}^* = \int_\Omega \left[\alpha_{ij}\varepsilon_{ij}^* + \tau_{ij}\left(r_{ij}^* - R_{ij}^*\right) + \chi_{ijk}^*\Sigma_{ijk}\right] d\Omega \tag{2.52}$$

where $\alpha_{ij} = \sigma_{ij} - \tau_{ij}$.

A particular case of the Cosserat model, Cosserat second gradient model, its macro rotation is equal to the micro rotation, thus we get $r_{ij} = R_{ij}$.

(2) Second gradient model

During the last twenty years, the second gradient model have been proven to be an effective regularization technique, more analysis or applications could be found, in e.g. [82, 83, 84, 85, 86]. The works of Chambon et al. [8], Shu et al. [87] belong to this class of model, in which the microstrain is assumed to be equal to the macro strain, such that

$$f_{ij} = F_{ij} \tag{2.53}$$

And consequently

$$f_{ij} = \frac{\partial u_i}{\partial x_j} \tag{2.54}$$

The internal virtual work writes

$$W_{in}^* = \int_\Omega \left[ \sigma_{ij}\varepsilon_{ij}^* + \Sigma_{ijk}\chi_{ijk}^* \right] d\Omega \tag{2.55}$$

The following relation could be accomplished either by the use of continuity element or though the employment of Lagrange multiplier.

The constitutive laws of the second gradient model could be complex. However, the simplest relation between double stress and double strain is the following linear isotropic constitutive law.

$$
\begin{bmatrix}
\Sigma_{111} \\
\Sigma_{112} \\
\Sigma_{121} \\
\Sigma_{122} \\
\Sigma_{211} \\
\Sigma_{212} \\
\Sigma_{221} \\
\Sigma_{222}
\end{bmatrix}
=
\begin{bmatrix}
a^{12345} & 0 & 0 & a^{23} & 0 & a^{12} & a^{12} & 0 \\
0 & a^{145} & a^{145} & 0 & a^{25} & 0 & 0 & a^{12} \\
0 & a^{145} & a^{145} & 0 & a^{25} & 0 & 0 & a^{12} \\
a^{23} & 0 & 0 & a^{34} & 0 & a^{25} & a^{25} & 0 \\
0 & a^{25} & a^{25} & 0 & a^{34} & 0 & 0 & a^{23} \\
a^{12} & 0 & 0 & a^{25} & 0 & a^{145} & a^{145} & 0 \\
a^{12} & 0 & 0 & a^{25} & 0 & a^{145} & a^{145} & 0 \\
0 & a^{12} & a^{12} & 0 & a^{23} & 0 & 0 & a^{12345}
\end{bmatrix}
\begin{bmatrix}
\chi_{111} \\
\chi_{112} \\
\chi_{121} \\
\chi_{122} \\
\chi_{211} \\
\chi_{212} \\
\chi_{221} \\
\chi_{222}
\end{bmatrix}
\tag{2.56}
$$

where all the items in the coefficient matrix only depend on five constants defined by Mindlin [18], they are

$$a^{12345} = 2\left(a^1 + a^2 + a^3 + a^4 + a^5\right)$$
$$a^{23} = a^2 + 2a^3$$
$$a^{12} = a^1 + a^2/2$$
$$a^{145} = a^1/2 + a^4 + a^5/2$$
$$a^{25} = a^2/2 + a^5$$
$$a^{34} = 2\left(a^3 + a^4\right)$$

47

Four of the five parameters are material characteristic lengths whilst the last one is a coupling parameter as proved by Sciarra [88]. A simple constitutive law involving only one parameter $D_{sg}$ is adopted in the following analysis. It has been intensively used in the literature (for example, [84], [86] and [82], et al.). Equation (2.57) is adopted in [84] and [86]. Different from that used by [82] and [89], in which all the components are positive while the absolute value of each component is the same as that in equation (2.57).

$$
\begin{bmatrix}
\sum_{111} \\
\sum_{112} \\
\sum_{121} \\
\sum_{122} \\
\sum_{211} \\
\sum_{212} \\
\sum_{221} \\
\sum_{222}
\end{bmatrix}
= D_{sg}
\begin{bmatrix}
1 & 0 & 0 & 0 & 0 & 1/2 & 1/2 & 0 \\
0 & 1/2 & 1/2 & 0 & -1/2 & 0 & 0 & 1/2 \\
0 & 1/2 & 1/2 & 0 & -1/2 & 0 & 0 & 1/2 \\
0 & 0 & 0 & 1 & 0 & -1/2 & -1/2 & 0 \\
0 & -1/2 & -1/2 & 0 & 1 & 0 & 0 & 0 \\
1/2 & 0 & 0 & -1/2 & 0 & 1/2 & 1/2 & 0 \\
1/2 & 0 & 0 & -1/2 & 0 & 1/2 & 1/2 & 0 \\
0 & 1/2 & 1/2 & 0 & 0 & 0 & 0 & 1
\end{bmatrix}
\begin{bmatrix}
\chi_{111} \\
\chi_{112} \\
\chi_{121} \\
\chi_{122} \\
\chi_{211} \\
\chi_{212} \\
\chi_{221} \\
\chi_{222}
\end{bmatrix}
\tag{2.57}
$$

Table 2.4: Summary of element type for second gradient model

| Name | TU24L4 | TU24L12 | TU36L12 | QU34L4 | QU34L16 | QU54L16 | QU32L4 | TU24L1 | TU27L3 | TU24L6 |
|---|---|---|---|---|---|---|---|---|---|---|
| Element |  |  |  |  |  |  |  |  |  |  |
| Interpolation | $u_i$ P2 $v_{ij}$ P1 $\lambda_{ij}$ P0 | $u_i$ P2 $v_{ij}$ P1 $\lambda_{ij}$ P1 | $u_i$ P2 $v_{ij}$ P2 $\lambda_{ij}$ P1 | $u_i$ P2 $v_{ij}$ P1 $\lambda_{ij}$ P0 | $u_i$ P2 $v_{ij}$ P1 $\lambda_{ij}$ P1 | $u_i$ P2 $v_{ij}$ P2 $\lambda_{ij}$ P1 | $u_i$ P2 $v_{ij}$ P1 $\lambda_{ij}$ P0 | $u_i$ P2 $v_{ij}$ P1 $\lambda_{ij}$ P0 | $u_i$ P2 $v_{ij}$ P1 $\lambda_{ij}$ P1 | $u_i$ P2 $v_{ij}$ P2 $\lambda_{ij}$ P1 |
| Gauss integration |  |  |  |  |  |  |  |  |  |  |
| Reference | | | [87] | | | | [82] | | [90] | |

Each symbol represents one or more degrees of freedom, such that

$u_i$ ◆   $\lambda_{ij}$ ◣   $u_i$, $v_{ij}$ ⬤   $u_i$, $\lambda_{ij}$ ★

$u_i$, $v_{ij}$, $\lambda_{ij}$ ⬡   ✕ Gauss integration

$u_i$, $v_{ij}$, $\lambda_{ij}$ ◆ ⬡

The name rule of each element is explained here. The leading letter T or Q represents the element shape, triangular or quadrilateral. Un denotes the

total number of degrees of freedom ( for displacement $u_i$ and strain $v_{ij}$). The number of m Lagrange multiplier is denoted by Lm. Hence, TU24l4 is a triangular element with 24 degrees of freedom for $u_i$ and $v_{ij}$ and 4 Lagrange multipliers.

As for interpolation function, P2 is a quadratic form, P1 is a linear form and P0 is a constant form.

## 2.5.4 Viscoplasticity

Several investigations pointed out the capability of viscoplasticity to solve the pathological loss of uniqueness, once entering in the softening regime of the constitutive law, if an initial imperfection of a given characteristic size is provided [19]. However, once the localized area or the imperfection length is not predefined, the number of solutions are still infinite. Viscoplasticity has also been proposed as a method to overcome pathological mesh dependency problem, and its effectiveness has been numerically assessed for several specific case studies [91], [92] and [93]. Some say that rate dependnet model regularizes problem by delaying the occurrence of strain localization. Through a linear perturbation analysis, this is theoretically proved by [21]. Numerically, the delaying role was also found by Wang and Sluys [20] as the regularization effect is achieved by restricting the deformation process at the beginning. However, when deformation exceeds 40%, mesh dependency appears despite the use of viscoplasticity. As a consequence the capacity of viscoplasticity in regularizing the problem is limited.

Besides, when the viscous parameter should be validated apriori from a physical point of view, the viscoplasticity does not really regularize the problem for granular soils accorrding to [22]. Moreover, Goran Ljustina et al. [94], Larsson [95] and Pirali et al. [96] have both demonstrated that mesh dependence is still encountered using damage models regardless of the employment of viscoplasticity.

Overall, the capacity of viscoplasticity in regularizing the problem is limited as above mentioned and one can not benefit the regularization effect under the following conditions: small or inappropriate viscosity parameter is used or deformation exceed a certain value. When soil exhibiting viscous characteristics is described with viscoplastic models, a kind of numerical regularization can be obtained only within a time interval consistent with the viscous parameter introduced in the model. In order to remedy this inefficiency, it is necessary to add a more enhanced regularization technique.

In what follows viscoplasticity and second gradient model will be combined in order on the one hand to account for time dependent behavior of the constitutive relation and on the other one to get an effective regularization of the model during softening.

## 2.6    Concluding remarks

This chapter briefly reviews time-dependent behavior and strain localization of geomaterials observed both in laboratory and in field. Then the constitutive models to take into consideration the viscous effect are introduced and the general elasto-viscoplastic model is adopted in the application of boundary value problems after comparison. Regularization techniques to remedy the inefficiency of classical medium are also discussed. Moreover, few remarks are given on the theory of uniqueness and bifurcation from literature results.

# Chapter 3

# Analytical and numerical investigations using viscoplastic models

## 3.1 Introduction

In the literature, several authors attribute a regularization effect to rate-dependent constitutive laws based on viscoplasticity, often used for geomaterials to describe viscous phenomena typical of their mechanical response. Analytical and numerical studies are presented in this chapter to investigate this claim based on the Hill's criterion, the Rice criterion, the results of a numerical perturbation algorithm and a 1D linear perturbation analysis.

## 3.2 One-dimensional analytical and numerical study

Consider a 1 D bar subjected to an axial displacement at the right end and fixed at the left end, see Fig 3.1. The boundary conditions are:

$$u(0) = 0$$
$$u(L) = Vt \tag{3.1}$$

where $V = \frac{\partial u(L)}{\partial t}$ is the loading rate, $u(0)$ and $u(L)$ the displacements at the two extremities and $L$ the bar length.
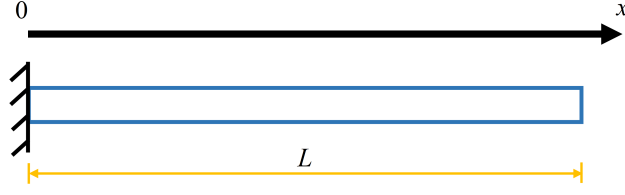
Figure 3.1: Geometry of the 1D bar

### 3.2.1 Constitutive laws

Without loss of generality a piecewise linear constitutive law is adopted Fig 3.2, where $A_1 > 0$ and $A_2 < 0$ specify respectively the positive and negative slope and $\gamma_{lim}$ the limit strain at the stress peak (see also [97]). In the absence of viscous terms, the rate-independent
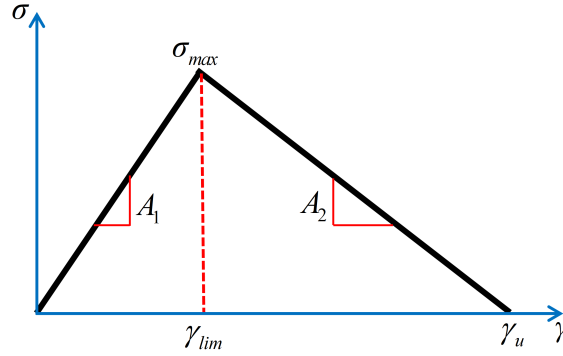


Figure 3.2: 1 D piecewise constitutive law

yield function $f$ is given by

$$f(\sigma, \gamma) = \begin{cases} \sigma - \sigma_{max} & (\gamma < \gamma_{lim}) \\ \sigma - \sigma_{max} - A_2(\gamma - \gamma_{lim}) & (\gamma_{lim} < \gamma < \gamma_u) \end{cases} \tag{3.2}$$

where $f(\sigma_{max}, \gamma_{lim}) = f(0, \gamma_u) = 0$.

The 1D rate-dependent constitutive law is formulated hereafter following the Perzyna overstress model, the Duvaut-Lions model and the consistent model (see section 2.2.2). It is shown hereafter that the three models coincide under certain conditions.

In Perzyna's overstress theory, the viscoplastic strain is explicitly determined by the overstress function $\Phi(f)$, which can be chosen as $\Phi(f) = \frac{f}{\sigma_{max}}$. Substitution of $\Phi(f)$ in equation (2.4) provides the viscoplastic strain:

$$\dot{\gamma}^{vp} = \frac{1}{\eta \sigma_{max}}[\sigma - \sigma_{max} - A_2(\gamma - \gamma_{lim})] \tag{3.3}$$

In the Duvaut-Lions theory, the viscoplastic strain (equation (2.7)) depends on $\sigma_\infty$ that is found according to Fig 3.2 equal to:

$$\sigma_\infty = \sigma_{max} + A_2(\gamma - \gamma_{lim}) \tag{3.4}$$

The Duvaut-Lions model viscoplastic strain rate becomes therefore:

$$\dot{\gamma}^{vp} = \frac{1}{\eta A}[\sigma - \sigma_{max} - A_2(\gamma - \gamma_{lim})] \tag{3.5}$$

The viscoplastic strain rate of the Duvaut-Lions model coincides with the Perzyna's rate if:

$$A = \sigma_{max} \tag{3.6}$$

Finally, the yield function of the consistent viscoplastic model depends on the strain and the strain rate, equation (3.7). For the 1D case one gets:

$$f(\sigma, \gamma) = \sigma - \sigma_{max} - \gamma^{vp}\frac{A_1 A_2}{A_2 - A_1} - y\dot{\gamma}^{vp} \tag{3.7}$$

where $y$ is the hardening function related to the strain rate effect. In order to get the same expression as for the Perzyna's overstress model, $y$ can be chosen as [98]:

$$y = \eta\left(\frac{d\Phi(f)}{df}\right)^{-1} = \eta\sigma_{max} \tag{3.8}$$

In the following, the viscoplastic strain rate is finally considered equal to:

$$\dot{\gamma}^{vp} = \frac{1}{\eta\sigma_{max}}[\sigma - \sigma_{max} - A_2(\gamma - \gamma_{lim})] \tag{3.9}$$

## 3.2.2   Loss of uniqueness

The stress-strain relation of the 1D problem is:

$$\dot{\sigma} = A_1(\dot{\gamma} - \dot{\gamma}^{vp}) \tag{3.10}$$

A constant loading velocity $V$ applied at the right end of the beam (equation (3.1)) results in a constant strain given by:

$$\dot{\gamma} = V/L \tag{3.11}$$

Introducing the viscoplastic strain equation (3.9) into equation (3.10) provides:

$$\dot{\sigma} = A_1\{\dot{\gamma} - \frac{1}{\eta\sigma_{max}}[\sigma - \sigma_{max} - A_2(\gamma - \gamma_{lim})]\} \tag{3.12}$$

After some rearrangements, the governing equation of the problem is the following first order linear differential equation:

$$\dot{\sigma} = -\frac{A_1}{\eta \sigma_{max}}\sigma + A_1 \dot{\gamma} + \frac{A_1}{\eta} + \frac{A_1 A_2}{\eta \sigma_{max}}(\gamma - \gamma_{lim}) \tag{3.13}$$

If we assume the initial state corresponding to the peak of the rate-independent constitutive law, so that $\sigma \mid_{t=0} = \sigma_{max}$ and $\gamma \mid_{t=0} = \gamma_{lim}$, the solution of equation (3.13) is given as:

$$\sigma(t) = C_1 e^{-\frac{A_1 t}{\eta \sigma_{max}}} - \frac{\dot{\gamma}\sigma_{max}\eta A_2}{A_1} + A_2 \dot{\gamma} t + \dot{\gamma}\sigma_{max}\eta + \sigma_{max} \tag{3.14}$$

with $C_1$ a constant determined from the initial condition $\sigma \mid_{t=0} = \sigma_{max}$ as:

$$C_1 = \frac{\dot{\gamma}\sigma_{max}\eta A_2}{A_1} - \dot{\gamma}\sigma_{max}\eta \tag{3.15}$$

The stress is therefore expressed as:

$$\sigma(t) = [\frac{\dot{\gamma}\sigma_{max}\eta A_2}{A_1} - \dot{\gamma}\sigma_{max}\eta]e^{-\frac{A_1 t}{\eta \sigma_{max}}} - \frac{\dot{\gamma}\sigma_{max}\eta A_2}{A_1} + A_2 \dot{\gamma} t + \dot{\gamma}\sigma_{max}\eta + \sigma_{max} \tag{3.16}$$

Numerical examples of the 1D bar problem are shown in Fig 3.3 considering different loading rates. The following parameters are chosen: $A_1 = 150$ kPa, $A_2 = -75$ kPa, $\gamma_{lim} = 0.1$, $\eta = 50$ kPa $\cdot$ s, $v_1 = 0.01$ m/s, $v_2 = 0.005$ m/s, $v_3 = 0.001$ m/s, $v_4 = 0$ (rate-independent), $L = 1$ m.
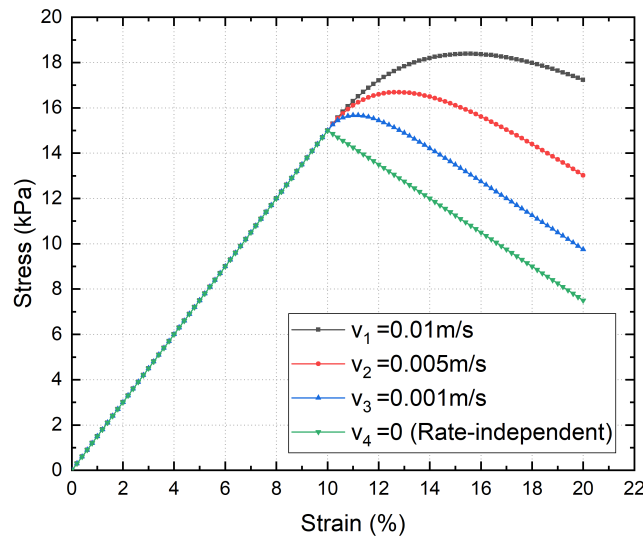


Figure 3.3: Stress-strain behaviour of the 1 D bar considering different strain velocities

It can be clearly seen that depending on the chosen loading rate, the peak points of the rate-dependent curves are not the same. The larger is the loading rate, the later appears the peak stress.

**Hill's criterion**

The loss of uniqueness is first studied hereafter using Hill's criterion. The expression for $\Delta\dot\sigma$ in terms of $\Delta\dot\gamma$ can be deduced by differentiating equation (3.16), as this last does not explicitly account for the value of imposed displacement boundary condition. A critical time $t_c$ exists such that for $t \geqslant t_c$ the positive definiteness of the second order work is lost:

$$t_c = \frac{\eta\sigma_{max}}{A_1} \ln\left(\frac{A_2 - A_1}{A_2}\right) \tag{3.17}$$

At $t_c$, the critical strain $\gamma_c$ corresponds to the peak stress value and it is found equal to:

$$\gamma_c = \gamma_{lim} + \frac{V\eta\sigma_{max}}{A_1 L} \ln\left(\frac{A_2 - A_1}{A_2}\right) \tag{3.18}$$

In terms of the stress-strain curve, the terms $\Delta\dot\gamma^2 e^{-\frac{A_1 t}{\eta\sigma_{max}}}$ and $\left(A_2 e^{\frac{A_1 t}{\eta\sigma_{max}}} + A_1 - A_2\right)$ are both positive at the peak of the rate-independent solution. With increasing time, the slope of the rate-dependent curve decreases and for $t > t_c$ becomes negative. Hill's criterion being a sufficient condition for the uniqueness of the solution, a bifurcation point (non uniqueness of the solution) can thus appear for $t \geqslant t_c$.

**Acoustic tensor**

As discussed in section 2.4, a particular form of loss of uniqueness is the formation of a shear band, occurring when the determinant of the acoustic tensor vanishes (see equation (2.33), $n$ being the outward unit vector normal to the localization band, which in the 1D case coincides with the direction of the bar). The tangent modulus $\mathbf{C}$ is in this case a scalar and it can easily be obtained as:

$$\mathbf{C} = \frac{\dot\sigma}{\dot\gamma} = e^{-\frac{A_1 t}{\eta\sigma_{max}}} \left(A_2 e^{\frac{A_1 t}{\eta\sigma_{max}}} + A_1 - A_2\right) \tag{3.19}$$

The determinant of the acoustic tensor $A(n)$ is therefore

$$det(A) = e^{-\frac{A_1 t}{\eta\sigma_{max}}} \left(A_2 e^{\frac{A_1 t}{\eta\sigma_{max}}} + A_1 - A_2\right) \tag{3.20}$$

indicating that $det(A) = 0$ holds true for the same critical time $t_c$ when Hill's criterion fails, i.e. the peak point of the stress-strain curve.

**Illustration of localized solutions**

The existence of multiple localized solutions when using viscoplastic models is addressed hereafter. Following the illustration presented in [97] for rate independent models, let us assume a localized solution so that one part of the bar unloads elastically (hard part) and the other softens (soft part), see Fig 3.4. The characteristic size of the domain affected by softening in what follows is termed $l$.

We denote hereafter the quantities inside the band by a superscript "0" and the quantities
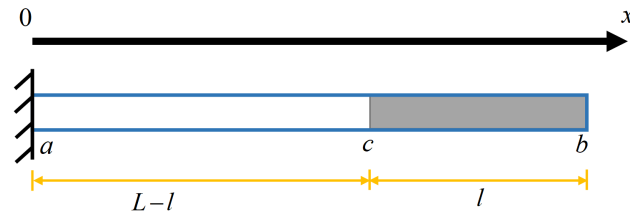


Figure 3.4: 1D bar; a hard (white) - soft (grey) localized solution

outside the band by a superscript "1". Equilibrium condition requires continuity of stresses; moreover, the longitudinal displacements should be also continuous. This implies that at the junction $c$ one has:

$$u^{0c} = u^{1c} = u^c$$
$$\sigma^{0c} = \sigma^{1c} = \sigma^c$$
(3.21)

The strain rate is assumed uniformly distributed in both parts of the bar with a jump across the band. Compatibility equations set the relationship between the strain rates:

$$\int_a^c \dot{\gamma}^0 \, dx = \dot{u}^c - \dot{u}^a = \dot{u}^c$$
$$\int_c^b \dot{\gamma}^1 \, dx = \dot{u}^b - \dot{u}^c = V - \dot{u}^c$$
(3.22)

The integration of equation (3.22) leads to

$$\dot{\gamma}^0 = \frac{V - \dot{\gamma}^1 l}{L - l}$$
(3.23)

Outside the band the behavior is elastic and thus the stress-strain rate relation gives

$$\dot{\sigma}^0 = A_1 \dot{\gamma}^0$$
(3.24)

Inside the band, the bar is submitted to a viscoplastic loading and the stress rate is given by equation (3.12):

$$\dot{\sigma}^1 = A_1 \{ \dot{\gamma}^1 - \frac{1}{\eta \sigma_{max}} [\sigma - \sigma_{max} - A_2 (\gamma - \gamma_{lim})] \}$$
(3.25)

58

Combining equation (3.24) and equation (3.25) and considering a continuous stress state, the two unknown strain rates $\dot{\gamma}^0$ and $\dot{\gamma}^1$ are:

$$A_1\{\dot{\gamma}^1 - \frac{1}{\eta\sigma_{max}}[\sigma - \sigma_{max} - A_2(\gamma - \gamma_{lim})]\} = A_1\dot{\gamma}^0 \tag{3.26}$$

Equations (3.23) and (3.26) constitute a linear algebraic system of equations whose solution are the unknown strain rates:

$$\dot{\gamma}^0 = \frac{\eta\sigma_{max}V - [\sigma - \sigma_{max} - A_2(\gamma - \gamma_{lim})]l}{\eta\sigma_{max}L}$$
$$\dot{\gamma}^1 = \frac{(L - l)\,[\sigma - \sigma_{max} - A_2(\gamma - \gamma_{lim})] + \eta\sigma_{max}V}{\eta\sigma_{max}L} \tag{3.27}$$

A viscoplastic constitutive law as the one studied in this paper does not have any internal length parameter. An infinite number of localized solutions is therefore possible, depending on the value of $l$. Two extreme solutions are found for $l = 0$ and $l = L$. The solution for $l = 0$ corresponds to stain localization inside a zero length zone and therefore to a spurious dissipation indicating mesh dependency (see also section 3.3.3). The solution for $l = L$ is the homogeneous solution. All the other intermediate solutions are possible. Fig 3.4 is an example of a typical localized pattern. Other patterns corresponding to alternative spatial distributions of soft and hard zones are however possible, as long as the total size of the soft parts is equal to $l$. Fig 3.5 for example illustrates two other patterns, a hard-soft-hard and a soft-hard-soft solution. The above conclusions are similar to the ones obtained for rate-independent constitutive laws that do not have any internal length parameter [97].



(a) Possible solution of hard-soft-hard form

(b) Possible solution of soft-hard-soft form
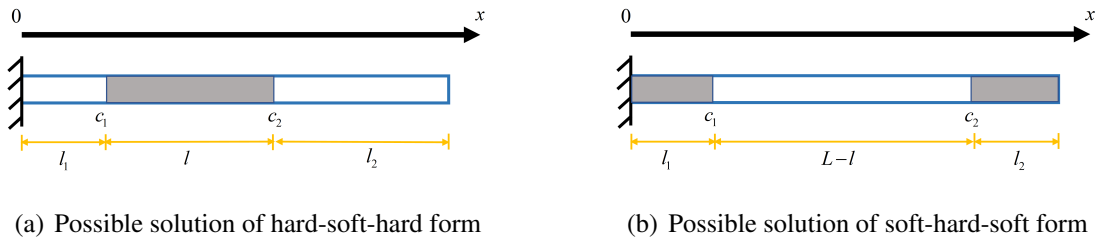
Figure 3.5: A hard-soft-hard (a) and a soft-hard-soft solution (b) of equation (3.27)

A numerical way to illustrate the different possible solutions and the mesh dependency problems when using a viscoplastic model is to use a random initialization technique (algorithm for non-uniqueness, see section 2.4.2). Three typical converged solutions are presented in Fig 3.6, where a random initialisation was applied at the peak (the point where the Hill's criterion is no longer satisfied). Near the peak, the three solutions seem similar to the homogeneous solution when looking at the global level, Fig 3.6. The local results (distribution of

the accumulated equivalent plastic strain) however show different localization patterns, Fig 3.7. A characteristic time $t_c$ can be also identified such that: for $t \leqslant t_c$, locally, different patterns of localization could be observed, however, globally there is no evident difference; when $t > t_c$ both global and local responses differ significantly, see Fig 3.6 and Fig. 3.8.
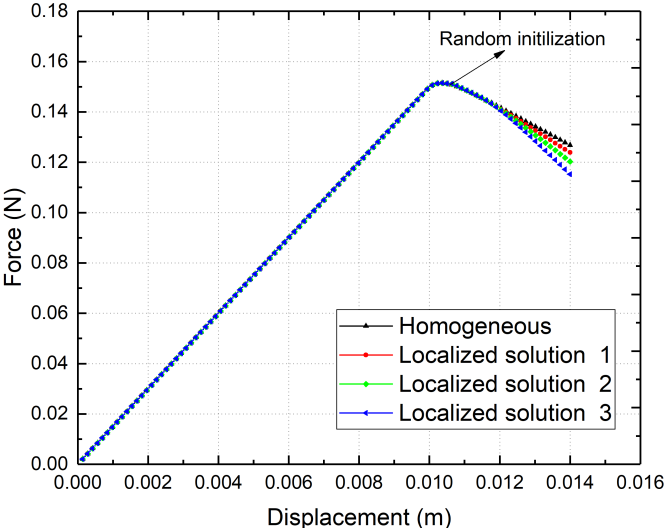


Figure 3.6: Global response: force-displacement curves for different localized solutions obtained with random initialization



(a) Localized solution 1      (b) Localized solution 2      (c) Localized solution 3
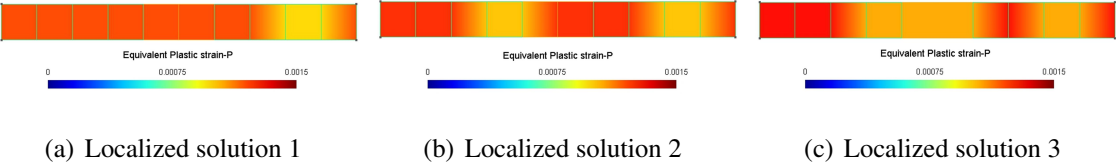
Figure 3.7: Local responses: accumulated equivalent plastic strain distribution for different localized solutions obtained using random initialization, at the peak



(a) Localized solution 1      (b) Localized solution 2      (c) Localized solution 3
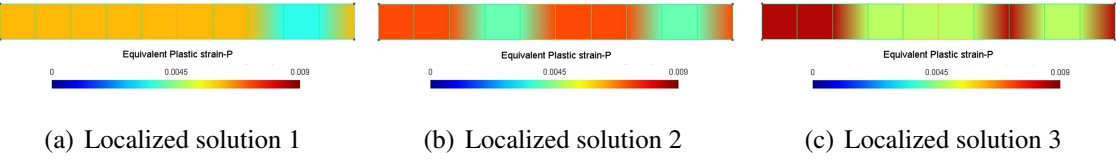
Figure 3.8: Local responses: accumulated equivalent plastic strain distribution for different localized solutions obtained using random initialization, last loading step

## 3.3 Two-dimensional numerical study

A biaxial numerical test is conducted hereafter to investigate the loss of uniqueness of the solution when using a viscoplastic constitutive law.

### 3.3.1 The MCC viscoplastic model

The consistent viscoplastic model is chosen due to its robust implementation algorithm (see section 2.2.2) and its ability to reproduce a smooth transition between rate-dependent and rate-independent solutions [99]. The viscoplastic model is based on the pressure sensitive Modified Cam Clay (MCC) model often used for clayey geomaterials. The well-known yield function of the MCC model is given by:

$$f(\sigma, p_c) = \frac{q^2}{M^2} + p(p - p_c) \tag{3.28}$$

where $p$ is the mean effective stress, $q$ the deviator stress, $p_c$ the preconsolidation pressure and $M$ the slope of the critical state line in the $p$-$q$ plane. An associated flow rule is adopted for simplicity. Depending on the plastic strain and strain rate, the derivatives of the preconsolidation pressure $p_c$ are therefore given by:

$$\frac{\partial p_c}{\partial \kappa} = h, \ \frac{\partial p_c}{\partial \dot{\kappa}} = y \tag{3.29}$$

where $h$ and $y$ are hardening functions associated with the internal variables $\kappa$ and $\dot{\kappa}$. Following the classical MCC model formulation $\kappa = \varepsilon_v^{vp}$, the volumetric plastic strain and $h$ is given as:

$$h = \nu^* p_c = \frac{1 + e_0}{\lambda^* - \kappa^*} p_c \tag{3.30}$$

where $e_0$ denotes the initial void ratio, $\lambda^*$ the virgin compression index and $\kappa^*$ the swelling index during a time increment from $t_n$ to $t_{n+1}$. The hardening parameter $\nu^*$ is considered constant [100].

The hardening function $y$ is assumed equal to the viscosity parameter $\eta$:

$$y = \eta \tag{3.31}$$

The rate form of $p_c$ writes:

$$\dot{p}_c = \nu^* p_c \dot{\kappa} + \eta \ddot{\kappa} \tag{3.32}$$

The initial preconsolidation pressure $p_c$ and the slope of the critical state line $M$ can be determined from constant strain rate tests, the initial void ratio $e_0$, the compression index $\lambda^*$ and the recompression index $\kappa^*$ from the oedometer test and the viscosity parameter $\eta$ from three different constant strain rate tests.

### 3.3.2 Validation of the viscoplastic MCC model

Before simulating the biaxial tests and in order to validate the implementation of the MCC viscoplastic model, undrained constant strain rate tests are simulated hereafter [101]. The calibrated model parameters are presented in Table 3.1, where the Poisson's ratio $\nu$ is taken to be 0.3.

Table 3.1: Calibrated parameters of the viscoplastic MCC model

| Category | Parameter | Value |
|---|---|---|
| Elastic parameters | Recompression index $\kappa^*$ | 0.06 |
| | Poisson's ratio $\nu$ | 0.3 |
| Plastic parameters | Compression index $\lambda^*$ | 0.4 |
| | Slope of critical state line $M$ | 1.2 |
| Viscous parameter | Viscosity parameter $\eta$ | $3 \times 10^9$ Pa·s |
| State variables | Initial preconsolidation pressure $p_c$ | 550 kPa |
| | Initial void ratio $e_0$ | 2 |

A good agreement between the experimental and the numerical results is observed in Fig 3.9, implying the good implementation and calibration of the model.
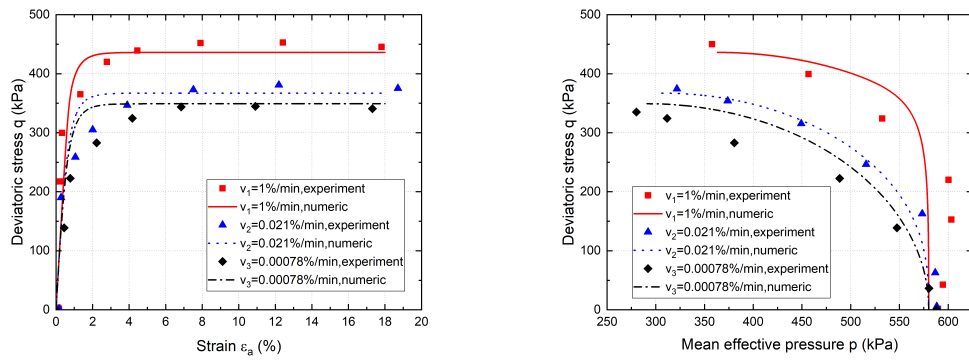
(a) Deviatoric stress versus strain    (b) Deviatoric stress versus mean effective stress

Figure 3.9: Validation of the viscoplastic MCC model: comparison between experimental and numerical results

### 3.3.3 Biaxial test

The geometry, the applied loading and the boundary conditions of the biaxial test reproduced numerically with the implemented viscoplastic MCC model are described hereafter. The aspect ratio of the specimen is taken equal to 2, small enough to avoid the occurence of buckling before the shear band localization, see Fig 3.10.
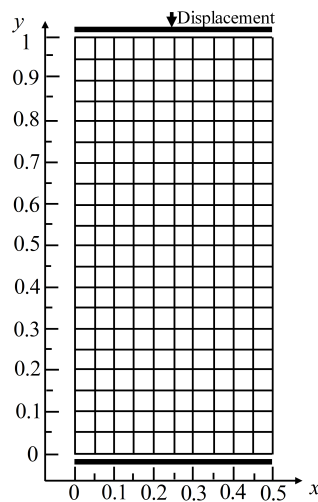


Figure 3.10: Loading and boundary conditions of the biaxial test

The specimen is submitted to a constant lateral confining pressure and to an imposed vertical displacement at the top. At the bottom, all vertical displacements are constrained and the horizontal direction of the middle point is fixed. Perfect sliding is assumed at the top and the

63

bottom of the specimen. The confining pressure is 50 kPa and the preconsolidation pressure 550 kPa, the soil specimen is thus in a state of overconsolidation (OCR=11). Once the yield surface is attained, plastic deformation makes the specimen shrink.

**Loss of uniqueness**

Three loading rates are considered, 0.002% m/min, 0.02% m/min, 0.2% m/min corresponding to a small, medium and large loading rate, respectively. The global responses are given in Fig 3.11 where it can be observed that different rates result in different peak points. The peak points are delayed by the rate effects, a result consistent with the 1D analysis presented in section 3.2.2.
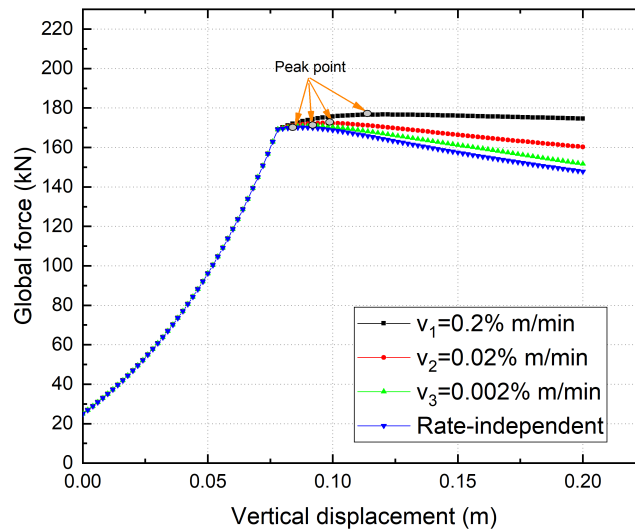


Figure 3.11: Biaxial test: global force-displacement curves for different loading rates

The uniqueness of the solution is studied in terms of Hill's criterion (equation (2.28)). It is found that the Hill's criterion is no longer satisfied at the peak points of Figure3.11 for the MMC model with and without rate effects. From the peak points and on (increasing displacements) the uniqueness of the solution is therefore no longer guaranteed.

Shear band formation in bifurcation points is then investigated by means of the Rice criterion, equation (2.33), see Fig 3.12. Four characteristic steps are selected: elastic step, first plastic step, first bifurcated step and last step as shown in Fig 3.12(a). The Rice criterion evolution associated to the uniform solution is presented during the increasing loading history in Fig 3.12(b) as a function of $\tan \theta$, where $\theta$ is the orientation of the shear band normal

to the loading vertical axis, i.e. the shear band orientation with the horizontal direction. The determinant of the acoustic tensor $det(Q)$ is calculated using equation (2.35) and plotted here as a normalized value with respect to a fixed value (the determinant at the first elastic step) for simplicity. It can be seen that for the elastic step, the determinant of the acoustic tensor is always positive. As the loading increases up to the first plastic step, two extrema appear but the minimum value of the deteminant remains positive. Later on, a bifurcation point with two possible bifurcated directions occurs, since a double real solution appears. At this point, that coincides with the peak of the global curve, the Hill's criterion is also violated as the flow rule is associated, see also section 3.2.2 and [102]. From higher levels of loading, four possible bifurcated directions occur till the last step. A similar evolution is found for rate independent materials [103] and for multiphysics couplings [104].

Another method to illustrate different bifurcated solutions is to apply the algorithm for the random initialisation, see section 2.4.2. Fig 3.13 presents the homogeneous solution, a bifurcated solution and the position of the bifurcation point (after the peak point, corresponding to a vertical displacement of 0.0098 m). At the local level, two modes of strain localization are illustrated in Fig 3.14.

**Mesh dependency**

The purpose is this section is to illustrate mesh dependency problems when using a viscoplastic constitutive law. In the following analysis weak elements are introduced to trigger localization in three different meshes: a coarse mesh of $10 \times 20$ elements, a medium mesh of $20 \times 40$ and a fine mesh of $30 \times 60$ elements. The area of the weak elements is kept the same for three mesh refinements. The global and local responses (last step) for the three meshes under a medium imposed loading rate are given in Fig 3.15 and Fig 3.16. It can be qualitatively observed that the size of the finite element mesh controls the solution at the global level but also the width and the magnitude of the shear bands.
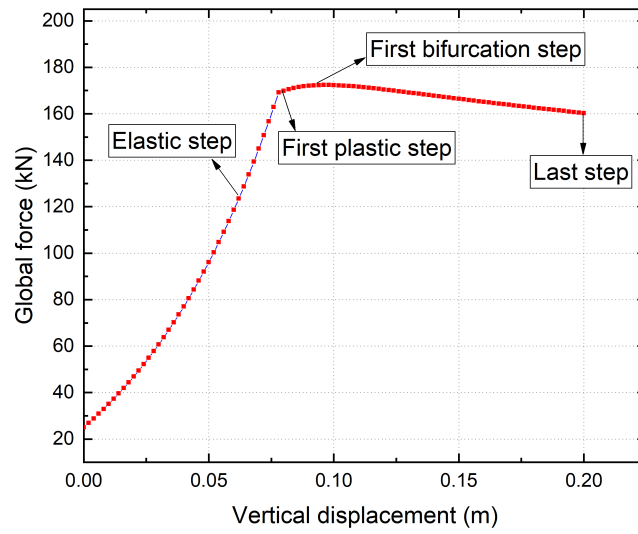
(a) Four characteristic steps
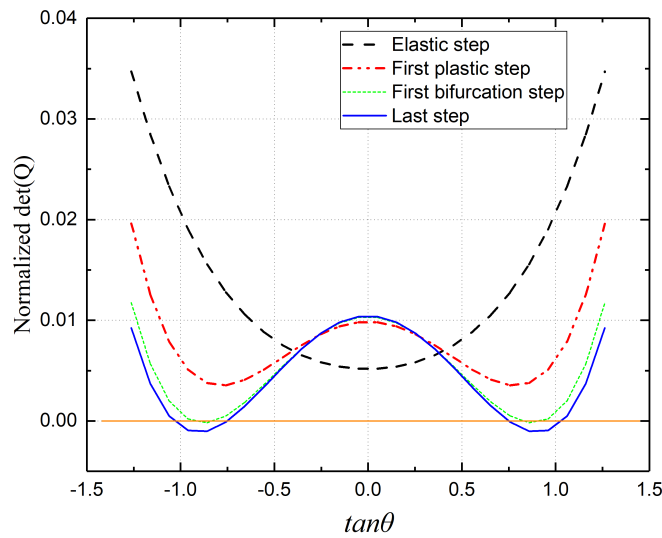


(b) Evolution of the Rice criterion

Figure 3.12: Biaxial test: evolution of the Rice criterion for four characteristic steps

## 3.4 One-dimensional linear perturbation analysis using viscoplastic model

Another way to study the stability condition (the onset condition for the growth of small periodic non-uniformities) for the case of a viscoplastic law is to perform a 1D linear pertur-
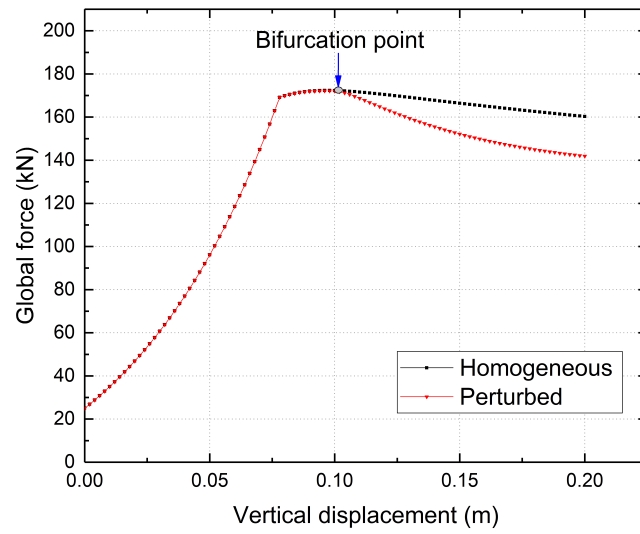
Figure 3.13: Biaxial test: homogeneous solution and a bifurcated solution obtained using random initialization



(a) Example 1         (b) Example 2
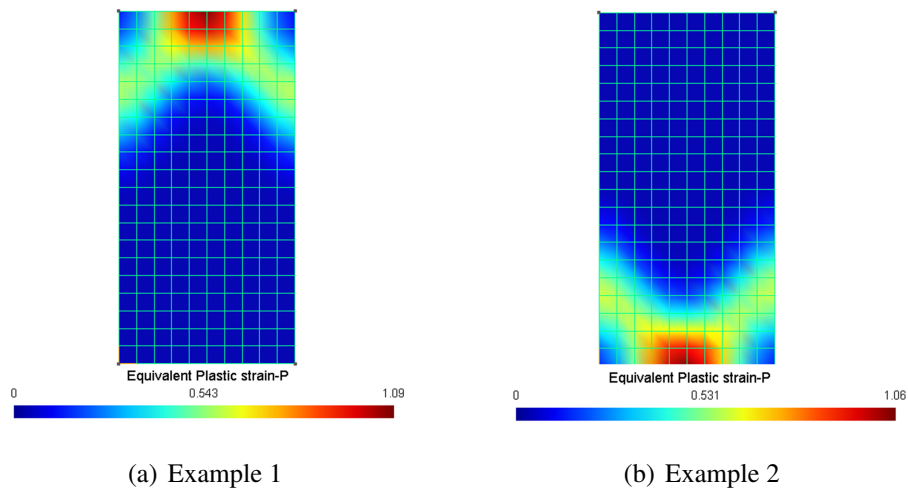
Figure 3.14: Biaxial test: two examples of localized solutions obtained using random initialization

bation analysis. Linear analysis is adopted on the one hand to capture sufficiently the onset of instability condition, on the other hand to obtain an analytical solution. Examples of 1D, 2D and 3D linear perturbation analyses are also presented in [105, 106, 21].

67
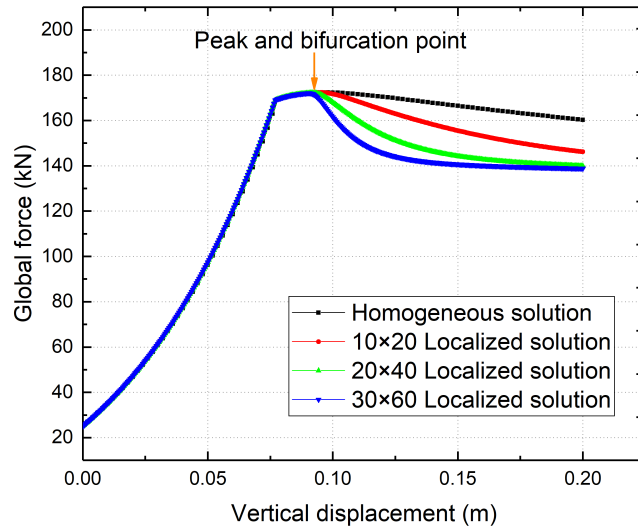
Figure 3.15: Biaxial test: global force-displacement curves for different mesh sizes



(a) $10 \times 20$ elements      (b) $20 \times 40$ elements      (c) $30 \times 60$ elements
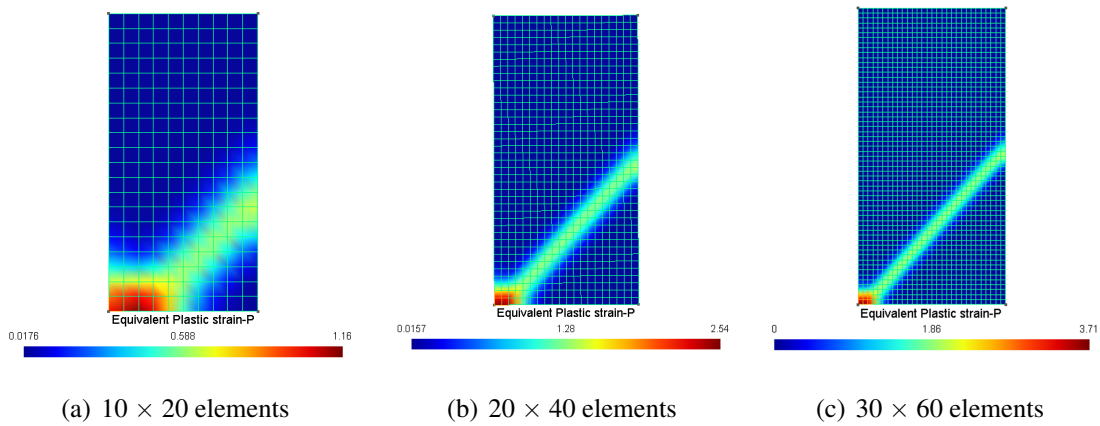
Figure 3.16: Biaxial test: distribution of accumulated equivalent plastic strain for different mesh sizes, last loading step

## 3.4.1 Fundamental relations

**Equilibrium equation**

The equilibrium equation for the 1D case is

$$\frac{\partial \sigma}{\partial x} = 0 \tag{3.33}$$

68

**Constitutive law**

The 1D viscoplastic constitutive law and the viscoplastic strain rate are:

$$\dot{\sigma} = E\left(\dot{\gamma} - \dot{\gamma}^{vp}\right)$$

$$\dot{\gamma}^{vp} = \frac{1}{\eta\sigma_{max}}[\sigma - \sigma_{max} - A_2(\gamma - \gamma_{lim})]^N \tag{3.34}$$

where $N \geqslant 1$ is a calibration parameter (for simplicity, $N = 1$ is assumed hereafter).

## 3.4.2 Perturbation analysis

The perturbation in displacement $\delta u$ is assumed to be periodic and imposed on the homogeneous state such that

$$\delta u = \hat{u}e^{\omega t + ikx} \tag{3.35}$$

with $k$ the wave number, $\omega$ the growth rate and the amplitude $\hat{u}$ is of order $\hat{u} \ll 1$. The perturbations related with displacement are derived as follows

$$\delta\dot{u} = \frac{\partial\delta u}{\partial t} = \omega\delta u$$

$$\delta\gamma = \frac{\partial\delta u}{\partial x} = ik\delta u$$

$$\delta\dot{\gamma} = \frac{\partial\delta\gamma}{\partial t} = ik\omega\delta u \tag{3.36}$$

$$\delta\dot{\gamma}_{,x} = \frac{\partial\delta\dot{\gamma}}{\partial x} = -k^2\omega\delta u$$

The perturbation of the viscoplastic strain is obtained as

$$\delta\dot{\gamma}^{vp} = \frac{N}{\eta\sigma_{max}}[\sigma - \sigma_{max} - A_2(\gamma - \gamma_{lim})]^{N-1}\left(\delta\sigma - A_2\delta\gamma\right) \tag{3.37}$$

For simplicity, $N = 1$ is assumed. Differentiation of the two sides of equation (3.37) with respect to $x$ yields

$$\delta\dot{\gamma}_{,x}^{vp} = \frac{k^2 A_2}{\eta\sigma_{max}}\delta u \tag{3.38}$$

where the term $\delta\sigma_{,x} = 0$ vanishes according to equilibrium equation (3.33).

Furthermore, the perturbation of the constitutive law presented in the first equation of (3.34) leads to

$$\delta\dot{\gamma}_{,x}^{vp} = \frac{\delta\dot{\sigma}_{,x}}{E} - \delta\dot{\gamma}_{,x} = -k^2\omega\delta u \tag{3.39}$$

Equating expressions (3.38) and (3.39) provides the characteristic stability equation:

$$\omega = -\frac{A_2}{\eta\sigma_{max}} \tag{3.40}$$

The following conclusions can be drown:

- For $\omega$ real and positive the perturbation grows with time and instability is possible. For $\omega$ real and negative the perturbed solution decays with time and the homogeneous solution is stable.

- $\eta$ and $\sigma_{max}$ being positive, the sign of the growth rate depends on the sign of the hardening modulus $A_2$. As long as $A_2$ is non-negative, the growth rate decays with time. When softening occurs ($A_2 < 0$) the growth rate increases exponentially.

- The growth rate is independent of the wave number $k$. Its magnitude is inversely proportional to the viscosity and the maximum stress $\sigma_{\mathrm{max}}$.

The previous results agree also with [107] that states that viscoplastic materials are unstable when strain softening occurs.

## 3.5   Discussion on the viscosity parameter

We finally present a brief discussion concerning the physical meaning of the viscosity-like parameter $\eta$ with respect to the material viscosity that can be experimentally measured. In [108], values of viscosity for mixtures of kaolinite and water are provided when the water content is between $57\%$ and $63\%$; the viscosity typically varies between $7{\times}10^4$ and $6{\times}10^5$ Pa·s. In [109], a fall cone test was performed to determine the viscosity of kaolin soils. The authors found that the viscosity ranges between $1{\times}10^3$ and $1{\times}10^4$ Pa·s when the liquidity index is limited within $0.3$ and $1$ and the water content is in the range of $35.8\%$ and $47.4\%$. The same method was adopted for kaolin soils by [110] to show that the shear viscosity decreases exponentially with the liquidity index. When the water content lies between $35.84\%$ and $45.51\%$ and the liquidity index from $0.34$ to $0.91$, viscosity is between $200$ and $516$Pa·s. Measures of viscosity were also obtained by [111] using a rotational rheometer for kaolinite, Ca-montmorillonite and Na-montmorillonite soils; viscosity ranges in that case from $1{\times}10^3$ to $1{\times}10^6$ Pa·s when the water content is between $20\%$ and $180\%$. In laboratory tests, when a soft soil is in plastic state, the measured viscosity lies between $2{\times}10^2$ and $1{\times}10^6$ Pa·s. The aforementioned viscosity measures are summarized in Table 3.2.

In numerical simulations, the viscosity-like parameter $\eta$ of the viscoplastic model estimated

Table 3.2: Viscosity measured experimentally for soft soils

| No | Water content | Fluidity index | Viscosity/Pa·s | Reference |
|----|---------------|----------------|----------------|-----------|
| 1 | $57\% \sim 63\%$ | / | $7{\times}10^4 \sim 6{\times}10^5$ | [108] |
| 2 | $35.84\% \sim 45.51\%$ | $0.34 \sim 0.91$ | $200 \sim 516$ | [110] |
| 3 | $35.8\% \sim 47.4\%$ | $0.3 \sim 1$ | $1{\times}10^3 \sim 1{\times}10^4$ | [109] |
| 4 | / | $0 \sim 1$ | $2{\times}10^2 \sim 1{\times}10^6$ | [112] |
| 5 | $20\% \sim 180\%$ | / | $1{\times}10^3 \sim 1{\times}10^6$ | [111] |

according to the procedure discussed in section 3.3.2 is $3 \times 10^9$ Pa·s, which is far beyond the experimentally measured values. This means that even if $\eta$ has the same physical dimensions as a viscosity, it is just a model parameter to be fitted by back-analysis.

## 3.6 Concluding remarks

In this chapter we have studied the possibility to use a rate dependent constitutive law (viscoplasticity) for soft soils to describe their intrinsic time-dependent response and the so-called regularization effect which several authors attribute to the viscoplastic model. Analytical and numerical studies were presented and several conclusions are found based on the Hill's criterion, the Rice criterion, the results of a numerical perturbation algorithm and a 1D linear perturbation analysis. The main conclusions are as follows:

1. It was found that the use of a rate dependent constitutive law (viscoplasticity) in a classical medium without an internal length parameter may result in an infinite number of possible solutions and strain localization in an infinitesimal band without energy dissipation. Results are therefore non objective and depend on the mesh size. Moreover, a 1D linear perturbation analysis showed that viscoplastic materials are no more stable when strain softening occurs. Increasing the viscosity parameter affects only the magnitude of growth rate but does not change its sign.

2. The use of a viscosity-like parameter may delay softening, strain localization and shear bands appear for subsequent loadings and time steps. Moreover, the viscosity-

like parameter of the constitutive law calibrated from experimental test results is not of the same order of magnitude as the material viscosity measured experimentally.

3. In order to simulate these phenomena in a realistic way, an internal length parameter should be introduced in the rate-dependent model, either using for example non local approaches or higher order media. This will be the subject of the next chapter.

# Chapter 4

# Numerical study using viscoplastic model in a second gradient continuum

## 4.1  Introduction

Among the different regularization techniques, the second gradient model is widely used in geomechanics and geotechnics providing very good results. This chapter begins by revisiting the formulation of a 1D and a 2D second gradient finite element that are both implemented into a Matlab based finite element code. In order to validate the implementation, a classical 1D benchmark is presented. A 2D plane strain problem is also studied including a thorough mesh dependency investigation and some parametric analyses. Finally, a 1D linear perturbation analysis is presented at the end of the chapter. The second gradient finite element formulation presented hereafter is based on the work of [8, 82, 113].

## 4.2  Second gradient finite elements

### 4.2.1  Virtual work principle and equilibrium equation

**Virtual work principle**

In the second gradient model, the microstrain is assumed equal to the macrostrain, such that

$$v_{ij} = \frac{\partial u_i}{\partial x_j} \tag{4.1}$$

For any kinematically admissible virtual displacement field $u_i^*$, the principle of virtual work implies

$$\int_\Omega \left( \sigma_{ij} \frac{\partial u_i^*}{\partial x_j} + \Sigma_{ijk} \frac{\partial^2 u_i^*}{\partial x_j \partial x_k} \right) d\Omega - W_e^* = 0 \tag{4.2}$$

where the superscript $(^*)$ denotes a virtual quantity, $\sigma_{ij}$ is the Cauchy stress tensor, $\Sigma_{ijk}$ the double stress tensor, $x_i$ the coordinate and $W_e^*$ the external virtual work done by the surface and body forces given hereafter

$$W_e^* = \int_\Omega \rho f_i u_i^* d\Omega + \int_\Gamma \left( p_i u_i^* + P_i D u_i^* \right) d\Gamma \tag{4.3}$$

where $f_i$ is the body force per unit mass, $\rho$ the mass density, $p_i$ the external force per unit area and $P_i$ the double force per unit area applied on a part of the boundary $\Gamma$. $D$ denotes the normal derivative, consequently $D u_i^* = \frac{\partial u_i^*}{\partial x_k} n_k$.

**Equilibrium equation**

As usual, the strong form of the balance equation is obtained from equation (4.2) by using the divergence theorem and integrating by parts,

$$\frac{\partial \sigma_{ij}}{\partial x_j} - \frac{\partial \Sigma_{ijk}}{\partial x_j \partial x_k} + \rho f_i = 0 \tag{4.4}$$

The second order derivative of the displacements requires $C_1$ continuity which complexifies the implementation. To avoid this, Lagrange multipliers are introduced and equation (4.2) turns into

$$\int_\Omega \left( \sigma_{ij} \frac{\partial u_i^*}{\partial x_j} + \Sigma_{ijk} \frac{\partial v_{ij}^*}{\partial x_k^t} \right) d\Omega - \int_\Omega \lambda_{ij} \left( \frac{\partial u_i^*}{\partial x_j} - v_{ij}^* \right) d\Omega - W_e^* = 0 \tag{4.5}$$

where $\lambda_{ij}$ represent the Lagrange multiplier field and the following constraint has to be met

$$\int_\Omega \lambda_{ij}^* \left( \frac{\partial u_i}{\partial x_j^t} - v_{ij} \right) d\Omega = 0 \tag{4.6}$$

The strong form equation turns into

$$\begin{aligned} \frac{\partial \sigma_{ij}}{\partial x_j} + \frac{\partial \lambda_{ij}}{\partial x_j} - \rho f_i = 0 \\ \frac{\partial \Sigma_{ijk}}{\partial x_k} - \lambda_{ij} = 0 \end{aligned} \tag{4.7}$$

## 4.2.2   1D second gradient finite element

A 1D second gradient finite element is first implemented into the FE Matlab code. The 1D element is composed of three nodes, two Gauss integration points and the following variables are: displacement $u_1$, microstrain $v_{11}$ and for the point in the middle the Lagrange multiplier $\lambda_{11}$, depicted in Fig 4.1.
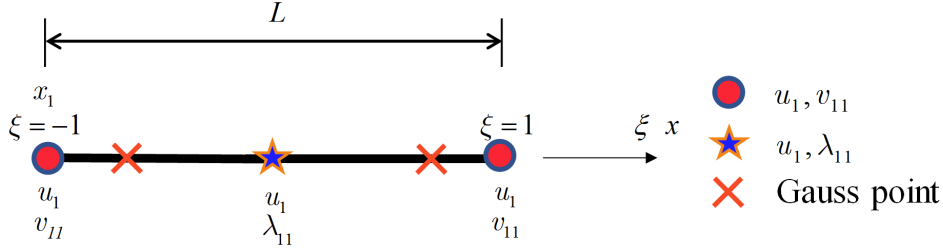


Figure 4.1: Scheme of the 1D second gradient element

The mapping from the reference element or master element to the physical element is shown in Fig 4.2. The physical element (of length $L$) is defined in $x$ coordinates while the reference element (that goes from $-1$ to $1$) is defined in $\xi$ coordinates.
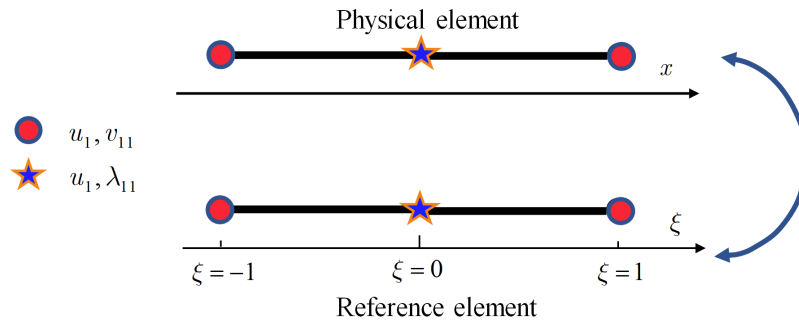


Figure 4.2: Mapping from the reference element to the physical element in 1D

The unknown variables $U_{(node)}$ at nodes in physical coordinates are functions of the reference coordinates denoted by $\xi$.

$$U_{(node)} = \left[ u_{1(\xi=-1)}, u_{1(\xi=1)}, u_{1(\xi=0)}, v_{11(\xi=-1)}, v_{11(\xi=1)}, \lambda_{11(\xi=0)} \right]^{\mathrm{T}} \tag{4.8}$$

In order to rewrite the virtual work principle, the following variables with respect to physical coordinate $x$ have to be considered.

$$dU_{(x)} = \left[ \frac{\partial u_1}{\partial x}, \frac{\partial v_{11}}{\partial x}, v_{11}, \lambda_{11} \right]^{\mathrm{T}} \tag{4.9}$$

75

And in a similar way with respect to reference coordinate $\xi$, $dU_{(\xi)}$ writes

$$dU_{(\xi)} = \left[ \frac{\partial u_1}{\partial \xi}, \frac{\partial v_{11}}{\partial \xi}, v_{11}, \lambda_{11} \right]^T \qquad (4.10)$$

Quadratic shape functions are adopted for the displacement field and the approximated displacements within the element are given by

$$u_1(\xi) = [N_1(\xi) \ N_2(\xi) \ N_3(\xi)] \begin{bmatrix} u_{1(\xi=-1)} \\ u_{1(\xi=1)} \\ u_{1(\xi=0)} \end{bmatrix} \qquad (4.11)$$

where $N_1(\xi) = 0.5\xi(\xi - 1)$, $N_2(\xi) = 0.5\xi(1 + \xi))$, $N_3(\xi) = 1 - \xi^2$

Linear shape functions are chosen for the microstrain field $v_{11}$ and thus

$$v_{11}(\xi) = [\psi_1(\xi) \ \psi_2(\xi)] \begin{bmatrix} v_{11(\xi=-1)} \\ v_{11(\xi=1)} \end{bmatrix} \qquad (4.12)$$

where $\psi_1(\xi) = 0.5(1 - \xi)$, $\psi_2(\xi) = 0.5(1 + \xi)$

The Lagrange multiplier is assumed constant within the element and thus

$$\lambda_{11}(\xi) = \lambda_{11}(\xi = 0) \qquad (4.13)$$

The approximation of the geometry is done with the same set of interpolation functions used to approximate the displacements (isoparametric formulation) which writes

$$x_1(\xi) = [N_1(\xi) \ N_2(\xi) \ N_3(\xi)] \begin{bmatrix} x_1(\xi = -1) \\ x_1(\xi = 1) \\ x_1(\xi = 0) \end{bmatrix} \qquad (4.14)$$

$U_{(node)}$ is consequently connected with $dU_{(\xi)}$ on the Gauss points by the transformation matrix B as follows

$$dU_{(\xi)} = B \ U_{(node)} \qquad (4.15)$$

in which

$$B = \begin{bmatrix} \frac{\partial N_1(\xi)}{\partial \xi} & 0 & \frac{\partial N_2(\xi)}{\partial \xi} & 0 & \frac{\partial N_3(\xi)}{\partial \xi} & 0 \\ 0 & \frac{\partial \psi_1(\xi)}{\partial \xi} & 0 & \frac{\partial \psi_2(\xi)}{\partial \xi} & 0 & 0 \\ 0 & \psi_1(\xi) & 0 & \psi_2(\xi) & 0 & 0 \\ 0 & 0 & 0 & 0 & 0 & 1 \end{bmatrix} \qquad (4.16)$$

As usual, by using the chain rule we get

$$
\begin{aligned}
\frac{\partial u_1}{\partial \xi} &= \frac{\partial u_1}{\partial x}\frac{\partial x}{\partial \xi} \\
\frac{\partial v_{11}}{\partial \xi} &= \frac{\partial v_{11}}{\partial x}\frac{\partial x}{\partial \xi}
\end{aligned}
\tag{4.17}
$$

and

$$
d\mathrm{U}_{(x)} = \mathrm{T}d\mathrm{U}_{(\xi)}
\tag{4.18}
$$

with

$$
\mathrm{T} = \begin{bmatrix}
\left[\frac{\partial x}{\partial \xi}\right]^{-1} & 0 & 0 & 0 \\
0 & \left[\frac{\partial x}{\partial \xi}\right]^{-1} & 0 & 0 \\
0 & 0 & 1 & 0 \\
0 & 0 & 0 & 1
\end{bmatrix}
\tag{4.19}
$$

**Discretization of body force in 1 D**

Using the virtual work principle, the discretization of the body force is given by

$$
\int_\Omega \rho f u^* d\Omega = [u^*]_{node}^{\mathrm{T}} \int_\Omega \rho [\mathrm{N}_{eb}]^{\mathrm{T}} f d\Omega = [u^*]_{node}^{\mathrm{T}} [f_{eb}]
\tag{4.20}
$$

where $\mathrm{N}_{eb} = \begin{bmatrix} N_1 & N_2 & N_3 & 0 & 0 & 0 \end{bmatrix}$, $N_1$, $N_2$ and $N_3$ are given in equation (4.11), $f$ is the body force value per unit mass.

### 4.2.3   2D second gradient finite element

A quadrilateral element with nine nodes, four Gauss integration points and one constant Lagrange multiplier is adopted hereafter [82, 113]. The variables are: displacements $u_i$, microstrains $v_{ij}$ and the Lagrange multiplier $\lambda_{ij}$, see Fig 4.3.

As before, the 9-node quadrilateral element in physical and reference coordinates is shown in Fig 4.4, where the physical element is defined in $x_1$-$x_2$ coordinates and the reference element in $\xi$-$\eta$ coordinates.
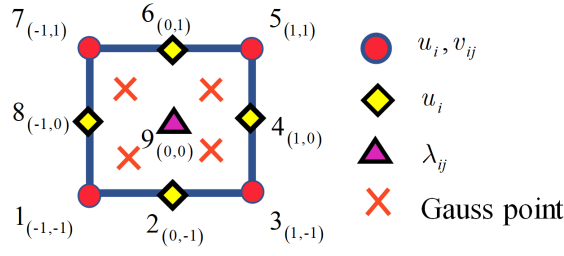
Figure 4.3: Scheme of the 2 D second gradient element
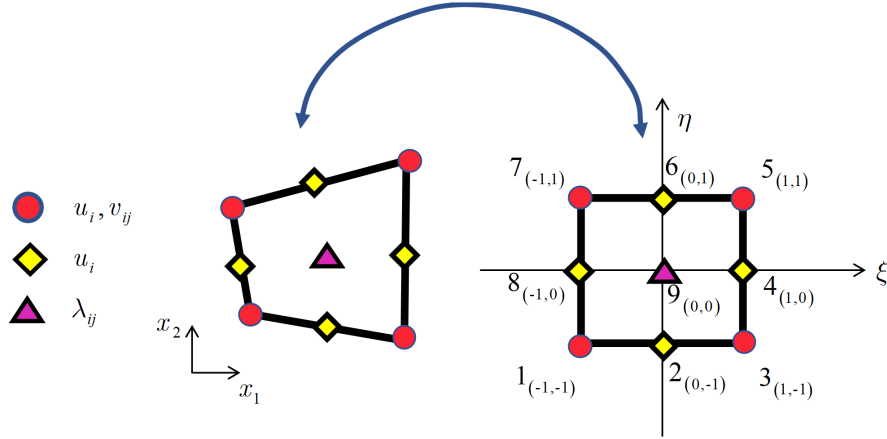


Figure 4.4: Mapping from the reference element to the physical element in 2D

The vector of unknown quantities at nodes is now denoted as

$$
\begin{aligned}
\mathrm{U}_{(\mathrm{node})} = [ & u_{1(\xi=-1,\eta=-1)}, u_{2(\xi=-1,\eta=-1)}, f_{11(\xi=-1,\eta=-1)}, f_{12(\xi=-1,\eta=-1)}, f_{21(\xi=-1,\eta=-1)}, \\
& f_{22(\xi=-1,\eta=-1)}, \cdots f_{22(\xi=-1,\eta=1)}, \lambda_{11(\xi=0,\eta=0)}, \lambda_{12(\xi=0,\eta=0)}, \lambda_{21(\xi=0,\eta=0)}, \lambda_{22(\xi=0,\eta=0)} ]^{\mathrm{T}}
\end{aligned}
$$

(4.21)

The application of the virtual work principle requires the following variables with respect to physical coordinate $x_1$, $x_2$.

$$
d\mathrm{U}_{(x_1,x_2)} = \left[ \begin{array}{ccccccccccccc} \frac{\partial u_1}{\partial x_1} & \frac{\partial u_1}{\partial x_2} & \frac{\partial u_2}{\partial x_1} & \frac{\partial u_2}{\partial x_2} & \frac{\partial v_{11}}{\partial x_1} & \cdots & v_{11} & v_{12} & v_{21} & v_{22} & \lambda_{11} & \lambda_{12} & \lambda_{21} & \lambda_{22} \end{array} \right]^{\mathrm{T}}
$$

(4.22)

With respect to the reference coordinate $\xi$ and $\eta$, the variables considered are

$$
d\mathrm{U}_{(\xi,\eta)} = \left[ \begin{array}{ccccccccccccc} \frac{\partial u_1}{\partial \xi} & \frac{\partial u_1}{\partial \eta} & \frac{\partial u_2}{\partial \xi} & \frac{\partial u_2}{\partial \eta} & \frac{\partial v_{11}}{\partial \xi} & \cdots & v_{11} & v_{12} & v_{21} & v_{22} & \lambda_{11} & \lambda_{12} & \lambda_{21} & \lambda_{22} \end{array} \right]^{\mathrm{T}}
$$

(4.23)

78

The displacements within the element are approximated by

$$u_i\left(\xi\right) = \left[N_1\left(\xi, \eta\right) N_2\left(\xi, \eta\right) \cdots N_8\left(\xi, \eta\right)\right]\begin{bmatrix} u_i \big|_{(\xi=-1,\eta=-1)} \\ u_i \big|_{(\xi=1,\eta=-1)} \\ u_i \big|_{(\xi=1,\eta=1)} \\ u_i \big|_{(\xi=-1,\eta=1)} \\ u_i \big|_{(\xi=0,\eta=-1)} \\ u_i \big|_{(\xi=1,\eta=0)} \\ u_i \big|_{(\xi=0,\eta=1)} \\ u_i \big|_{(\xi=-1,\eta=0)} \end{bmatrix} \quad (4.24)$$

with

$$N_1\left(\xi, \eta\right) = \tfrac{1}{4}\left(1 - \xi\right)\left(1 - \eta\right)\left(-1 - \xi - \eta\right)$$
$$N_2\left(\xi, \eta\right) = \tfrac{1}{4}\left(1 + \xi\right)\left(1 - \eta\right)\left(-1 + \xi - \eta\right)$$
$$N_3\left(\xi, \eta\right) = \tfrac{1}{4}\left(1 + \xi\right)\left(1 + \eta\right)\left(-1 + \xi + \eta\right)$$
$$N_4\left(\xi, \eta\right) = \tfrac{1}{4}\left(1 - \xi\right)\left(1 + \eta\right)\left(-1 - \xi + \eta\right)$$
$$N_5\left(\xi, \eta\right) = \tfrac{1}{2}\left(1 - \xi^2\right)\left(1 - \eta\right)$$
$$N_6\left(\xi, \eta\right) = \tfrac{1}{2}\left(1 + \xi\right)\left(1 - \eta^2\right)$$
$$N_7\left(\xi, \eta\right) = \tfrac{1}{2}\left(1 - \xi^2\right)\left(1 + \eta\right)$$
$$N_8\left(\xi, \eta\right) = \tfrac{1}{2}\left(1 - \xi\right)\left(1 - \eta^2\right)$$

A linear form is adopted for $v_{ij}$

$$v_{ij}\left(\xi, \eta\right) = \left[\psi_1\left(\xi, \eta\right) \psi_2\left(\xi, \eta\right) \psi_3\left(\xi, \eta\right) \psi_4\left(\xi, \eta\right)\right]\begin{bmatrix} v_{ij} \big|_{(\xi=-1,\eta=-1)} \\ v_{ij} \big|_{(\xi=1,\eta=-1)} \\ v_{ij} \big|_{(\xi=1,\eta=1)} \\ v_{ij} \big|_{(\xi=-1,\eta=1)} \end{bmatrix} \quad (4.25)$$

with

$$\psi_1\left(\xi, \eta\right) = \tfrac{1}{4}\left(1 - \xi\right)\left(1 - \eta\right)$$
$$\psi_2\left(\xi, \eta\right) = \tfrac{1}{4}\left(1 + \xi\right)\left(1 - \eta\right)$$
$$\psi_3\left(\xi, \eta\right) = \tfrac{1}{4}\left(1 + \xi\right)\left(1 + \eta\right)$$
$$\psi_4\left(\xi, \eta\right) = \tfrac{1}{4}\left(1 - \xi\right)\left(1 + \eta\right)$$

The Lagrange multiplier is considered constant within the element

$$\lambda_{ij}\left(\xi, \eta\right) = \lambda_{ij}\left(0, 0\right) \quad (4.26)$$

Concerning the mapping function from $(\xi, \eta)$ to $(x_1, x_2)$, the same set of shape functions $N_i$ as those for $u_i$ is adopted.

The nodal unknowns $U_{(node)}$ are connected with $dU_{(\xi,\eta)}$ by matrix B, such that

$$dU_{(\xi,\eta)} = B\ U_{(node)} \tag{4.27}$$

where

$$B = \begin{bmatrix} B_{u(1)} & 0_{(4\times4)} & B_{u(2)} & 0_{(4\times4)} & B_{u(3)} & 0_{(4\times4)} & B_{u(4)} & 0_{(4\times4)} & \cdots & B_{u(8)} & 0_{(4\times10)} \\ 0_{(12\times2)} & B_{v(1)} & 0_{(12\times2)} & B_{v(2)} & 0_{(12\times2)} & B_{v(3)} & 0_{(12\times2)} & B_{v(4)} & 0_{(12\times30)} \\ & & & & 0_{(4\times50)} & & & & & & I_{(4\times4)} \end{bmatrix}$$

with

$$B_{u(i)}{}^{\mathrm{T}} = \begin{bmatrix} \frac{\partial N_i}{\partial \xi} & \frac{\partial N_i}{\partial \eta} & 0 & 0 \\ 0 & 0 & \frac{\partial N_i}{\partial \xi} & \frac{\partial N_i}{\partial \xi} \end{bmatrix}$$

and

$$B_{v(i)}{}^{\mathrm{T}} = \begin{bmatrix} \frac{\partial \psi_i}{\partial \xi} & \frac{\partial \psi_i}{\partial \eta} & 0 & 0 & 0 & 0 & 0 & 0 & \psi_i & 0 & 0 & 0 \\ 0 & 0 & \frac{\partial \psi_i}{\partial \xi} & \frac{\partial \psi_i}{\partial \xi} & 0 & 0 & 0 & 0 & 0 & \psi_i & 0 & 0 \\ 0 & 0 & 0 & 0 & \frac{\partial \psi_i}{\partial \xi} & \frac{\partial \psi_i}{\partial \eta} & 0 & 0 & 0 & 0 & \psi_i & 0 \\ 0 & 0 & 0 & 0 & 0 & 0 & \frac{\partial \psi_i}{\partial \xi} & \frac{\partial \psi_i}{\partial \eta} & 0 & 0 & 0 & \psi_i \end{bmatrix}$$

The derivatives of $u_i$ and $v_{ij}$ with respect to the reference coordinates and physical coordinates hold the following relation by means of the chain rule,

$$
\begin{array}{ll}
\frac{\partial u_i}{\partial \xi} = \frac{\partial u_i}{\partial x_1}\frac{\partial x_1}{\partial \xi} + \frac{\partial u_i}{\partial x_2}\frac{\partial x_2}{\partial \xi} & \frac{\partial u_i}{\partial \eta} = \frac{\partial u_i}{\partial x_1}\frac{\partial x_1}{\partial \eta} + \frac{\partial u_i}{\partial x_2}\frac{\partial x_2}{\partial \eta} \\
\frac{\partial v_{ij}}{\partial \xi} = \frac{\partial v_{ij}}{\partial x_1}\frac{\partial x_1}{\partial \xi} + \frac{\partial v_{ij}}{\partial x_2}\frac{\partial x_2}{\partial \xi} & \frac{\partial v_{ij}}{\partial \eta} = \frac{\partial v_{ij}}{\partial x_1}\frac{\partial x_1}{\partial \eta} + \frac{\partial v_{ij}}{\partial x_2}\frac{\partial x_2}{\partial \eta}
\end{array} \tag{4.28}
$$

Using the matrix form, the above equation can be written as

$$\begin{bmatrix} \frac{\partial u_i}{\partial \xi} \\ \frac{\partial u_i}{\partial \eta} \end{bmatrix} = J^{\mathrm{T}} \begin{bmatrix} \frac{\partial u_i}{\partial x_1} \\ \frac{\partial u_i}{\partial x_2} \end{bmatrix} \qquad \begin{bmatrix} \frac{\partial v_{ij}}{\partial \xi} \\ \frac{\partial v_{ij}}{\partial \eta} \end{bmatrix} = J^{\mathrm{T}} \begin{bmatrix} \frac{\partial v_{ij}}{\partial x_1} \\ \frac{\partial v_{ij}}{\partial x_2} \end{bmatrix} \tag{4.29}$$

where J is called the Jacobian matrix and given by

$$J = \begin{bmatrix} \frac{\partial x_1}{\partial \xi} & \frac{\partial x_1}{\partial \eta} \\ \frac{\partial x_2}{\partial \xi} & \frac{\partial x_2}{\partial \eta} \end{bmatrix}$$

Inversely,

$$\begin{bmatrix} \frac{\partial u_i}{\partial x_1} \\ \frac{\partial u_i}{\partial x_2} \end{bmatrix} = \left(J^{\mathrm{T}}\right)^{-1} \begin{bmatrix} \frac{\partial u_i}{\partial \xi} \\ \frac{\partial u_i}{\partial \eta} \end{bmatrix} \tag{4.30}$$

Therefore, the vectors $dU_{(\xi,\eta)}$ and $dU_{(x_1,x_2)}$ are related via matrix T

$$dU_{(x_1,x_2)} = T dU_{(\xi,\eta)} \tag{4.31}$$

with

$$
T = \begin{bmatrix}
\left(J^T\right)^{-1} & & & & & & & \\
& \left(J^T\right)^{-1} & & & & & & \\
& & \left(J^T\right)^{-1} & & & & & \\
& & & \left(J^T\right)^{-1} & & & & \\
& & & & \left(J^T\right)^{-1} & & & \\
& & & & & \left(J^T\right)^{-1} & & \\
& & & & & & I_{4\times4} & \\
& & & & & & & I_{4\times4}
\end{bmatrix}
$$

where $I_{4\times4}$ is the identity matrix of size 4.

## Discretization of body force in 2 D

Using the virtual work principle, the discretization of the body force is given by

$$\int_\Omega \rho f_i u_i^* d\Omega = [u_i^*]^T_{node} \int_\Omega \rho [N_{eb}]^T f_i d\Omega = [u_i^*]^T_{node} [f_{eb}] \tag{4.32}$$

where

$$
N_{eb} = \begin{bmatrix} N_{eb(1)} & 0_{2\times4} & N_{eb(2)} & 0_{2\times4} & \cdots & N_{eb(8)} & 0_{2\times10} \end{bmatrix} \qquad
N_{eb(i)} = \begin{bmatrix} N_i & 0 \\ 0 & N_i \end{bmatrix}
$$

$N_i$ are given in equation (4.24), $f_i = \begin{bmatrix} f_1 & f_2 \end{bmatrix}^T$ is the body force vector per unit mass.

## Discretization of surface force in 2 D

Another set of shape functions is necessary to discretize the surface force. We have

$$
\begin{aligned}
u_i(\zeta) &= [\varphi_1(\zeta)\ \varphi_2(\zeta)\ \varphi_3(\zeta)] \begin{bmatrix} u_{i(\zeta=-1)} \\ u_{i(\zeta=1)} \\ u_{i(\zeta=0)} \\ x_{i(\zeta=-1)} \\ x_{i(\zeta=1)} \\ x_{i(\zeta=0)} \end{bmatrix} \\
x_i(\zeta) &= [\varphi_1(\zeta)\ \varphi_2(\zeta)\ \varphi_3(\zeta)]
\end{aligned} \tag{4.33}
$$

where

$$\varphi_1\left(\zeta\right) = \tfrac{1}{2}\left(\zeta^2 - \zeta\right)$$

$$\varphi_2\left(\zeta\right) = 1 - \zeta^2$$

$$\varphi_3\left(\zeta\right) = \tfrac{1}{2}\left(\zeta^2 + \zeta\right)$$

By means of the virtual work principle, the virtual work done by the surface force writes,

$$\int_\Gamma pn_i u_i^* d\Gamma = [u_i^*]_{node} \int_S [\mathrm{N}_{es}]^\mathrm{T} pn_i d\Gamma = [u_i^*]_{node}\,[f_{es}] \tag{4.34}$$

where the transformation matrix $[\mathrm{N}_{es}]$ is expressed by

$$[\mathrm{N}_{es}] = \begin{bmatrix} \varphi_1 & 0 & \varphi_2 & 0 & \varphi_3 & 0 \\ 0 & \varphi_1 & 0 & \varphi_2 & 0 & \varphi_3 \end{bmatrix}$$

For a 2D problem, $pn_i$ is written as $pn_i = \begin{bmatrix} pn_1 & pn_2 \end{bmatrix}^\mathrm{T}$.

The vector $\begin{bmatrix} n_1 & n_2 \end{bmatrix}^\mathrm{T}$ which is normal to the boundary is described as follows.

$$\begin{bmatrix} n_1 \\ n_2 \end{bmatrix} = \frac{1}{ds}\begin{bmatrix} -dx_2 \\ dx_1 \end{bmatrix} \tag{4.35}$$

where $ds = \sqrt{(dx_1)^2 + (dx_2)^2}$, $dx_1 = \frac{\partial x_1}{\partial \zeta}d\zeta$, $dx_2 = \frac{\partial x_2}{\partial \zeta}d\zeta$

After some arrangement, equation (4.35) is equivalent to

$$\begin{bmatrix} n_1 \\ n_2 \end{bmatrix} = \frac{d\zeta}{ds}[\mathrm{B}_{es}]^\mathrm{T}[x_i]_{node} \tag{4.36}$$

where

$$[\mathrm{B}_{es}]^\mathrm{T} = \begin{bmatrix} -\frac{\partial \varphi_1}{\partial \zeta} & 0 & -\frac{\partial \varphi_2}{\partial \zeta} & 0 & -\frac{\partial \varphi_3}{\partial \zeta} & 0 \\ 0 & \frac{\partial \varphi_1}{\partial \zeta} & 0 & \frac{\partial \varphi_2}{\partial \zeta} & 0 & \frac{\partial \varphi_1}{\partial \zeta} \end{bmatrix}$$

$$\left[x_{i(node)}\right]^\mathrm{T} = \begin{bmatrix} x_{1(\zeta=-1)} & x_{2(\zeta=-1)} & x_{1(\zeta=1)} & x_{2(\zeta=1)} & x_{1(\zeta=0)} & x_{2(\zeta=0)} \end{bmatrix}$$

$$\frac{d\zeta}{ds} = \frac{1}{\sqrt{\left(\frac{\partial x_1}{\partial \zeta}\right)^2 + \left(\frac{\partial x_2}{\partial \zeta}\right)^2}}$$

## 4.3   Validation of the second gradient FE code

In order to validate the implementation of the previous second gradient finite elements in the Matlab based finite element code, a one-dimensional problem is studied hereafter and the numerical results are compared with the corresponding analytical solutions obtained

by Chambon et al. [8]. The 3-node bar element in Fig 4.1 and the 9-node quadrilateral element in Fig 4.3 are both tested. In particular when the 9-node quadrilateral elements are used, all the degrees of freedom corresponding to the vertical direction ($u_2, v_{12}, v_{21}, v_{22}$) are constrained to be zero and the Poisson's ratio is set to 0 to eliminate 2D effects. Schematic diagrams concerning the geometry and boundary conditions are shown in Fig 4.5. The first gradient and second gradient constitutive laws are given in Fig 4.6, no coupling is assumed. The constitutive laws parameters are given in Table 4.1.



(a) 3-node bar element



(b) 9-node quadrilateral element
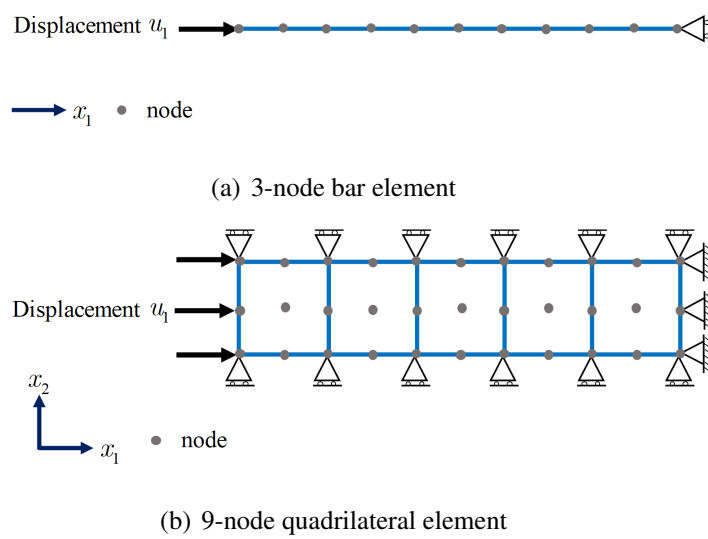
Figure 4.5: Geometry and boundary conditions of the 1D problem using 3-node bar element and 9-node quadrilateral element
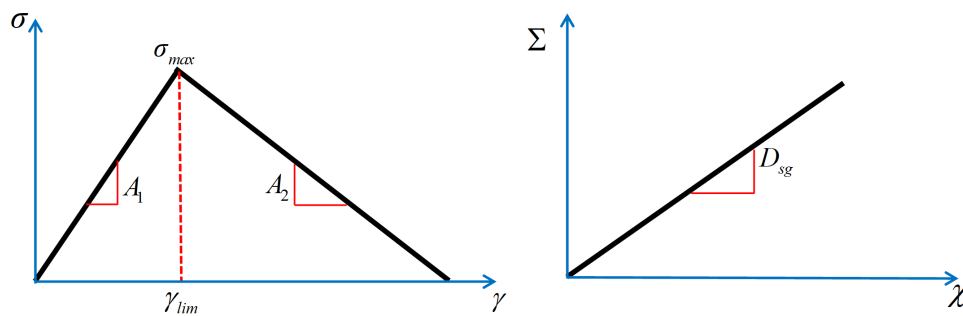


Figure 4.6: First gradient and second gradient constitutive laws for the 1D problem

83

Table 4.1: Material parameters used for the validation of second gradient FE code

| Symbol | Value | Unit |
|:---:|:---:|:---:|
| $A_1$ | 150 | kPa |
| $A_2$ | -75 | kPa |
| $D_{sg}$ | 0.8 | $\text{Pa} \cdot \text{m}^2$ |
| $\gamma_{lim}$ | 0.01 | |

### 4.3.1 Analytical solutions

The analytical solutions of the 1D problem [8] are hereafter briefly recalled. The internal virtual work in the 1D domain $[a, b]$ is given as

$$W_{in}^* = \int_a^b (\sigma \frac{\partial u^*}{\partial x} + \Sigma \frac{\partial^2 u^*}{\partial x^2}) dx \tag{4.37}$$

Assuming that the external force is applied at the two ends $a$ and $b$, the external work reads

$$W_e^* = \nu_b u_b^* + \nu_a u_a^* + \mu_b u_b^{*'} + \mu_a u_a^{*'} \tag{4.38}$$

where $\nu$ is the classical external force and $\mu$ denotes the additional external double force. By means of the virtual work principle and integrating by parts, the balanced equation writes

$$\frac{\partial \sigma}{\partial x} - \frac{\partial^2 \Sigma}{\partial x^2} = 0 \tag{4.39}$$

Integration of equation (4.39) leads to

$$\sigma - \frac{d\Sigma}{dx} = \sigma_0 \tag{4.40}$$

where $\sigma_0$ is an unknown constant.

The constitutive laws of first and second gradient parts shown in Fig 4.6 can be expressed as,

$$\sigma = Eu' + F \quad \Sigma = D_{sg} u'' \tag{4.41}$$

where $u' = \frac{du}{dx}$, $u'' = \frac{d^2 u}{dx^2}$

along with

$$u' \leqslant \gamma_{lim} \quad E = A_1, \quad F = 0$$

$$u' > \gamma_{lim} \quad E = A_2, \quad F = (A_1 - A_2)\gamma_{lim}$$

Combined with the equilibrium equation (4.40), the following differential equations are obtained

$$
\begin{cases}
A_1 u - D_{sg} u'' = \sigma_0 x + K & u' \leqslant \gamma_{lim} \\
A_2 u - D_{sg} u'' = [\sigma_0 + (A_2 - A_1)\gamma_{lim}] x + K & u' > \gamma_{lim}
\end{cases}
\tag{4.42}
$$

After integration, the solutions are given as follows:

for $u' \leqslant \gamma_{lim}$

$$
u = \sigma_0/A_1 x + K + \alpha ch(w_h x) + \beta sh(w_h x) \quad w_h = \sqrt{A_1/D_{sg}}
\tag{4.43}
$$

called hereafter "hard solution"

for $u' > \gamma_{lim}$

$$
u = [\sigma_0 + (A_2 - A_1)\gamma_{lim}]/A_1 x + K + \alpha \cos(w_s x) + \beta \sin(w_s x) \quad w_s = \sqrt{-A_2/D_{sg}}
\tag{4.44}
$$

called hereafter "soft solution".

$\alpha, \beta, K$ in equations (4.43) and (4.44) are constants to be determined.

The authors in [8] found the analytical solutions that satisfy the continuity and boundary conditions. Assuming there are $n$ pieces of such fundamental solutions (the sum of hard pieces and soft pieces is $n$), the unknowns in total are $4n + 1$ ($n\alpha$, $n\beta$, $nK$, pieces length $nl$ and the constant stress $\sigma_0$).

To solve this problem, the following boundary conditions could be chosen

$$
u_a = U \quad u_b = 0 \quad \Sigma_a = 0 \quad \Sigma_b = 0
\tag{4.45}
$$

Using the displacement continuity, the second gradient stress continuity, the strain continuity (necessarily equal to $\gamma_{lim}$) at the junction, $4n - 4$ equations are found. Along with the four boundary conditions given in (4.45) and the total length of the bar $l$, the number of unknowns and equations are equal and consequently different solutions can be found. Moreover, given that $n$ can not be too large with respect to the ratio $l\big/\sqrt{-A_2/D_{sg}}$, the number of possible solutions are finite.

## 4.3.2   Analytical versus numerical results

Two analytical solutions together with the homogeneous one are compared with the numerical results obtained with both the 1D and the 2D second gradient finite element. The random initialization procedure detailed in section 2.4 was applied to find the possible solutions. The same numerical result was obtained for both the 1D element and 2D element. Fig 4.7 presents the analytical and numerical force-displacement curves for three different solutions (homogeneous, hard-soft-hard and soft-hard-soft-hard solutions). Fig 4.8 presents the analytical and numerical strain distributions for three different solutions (homogeneous, hard-soft-hard and soft-hard-soft-hard solutions).
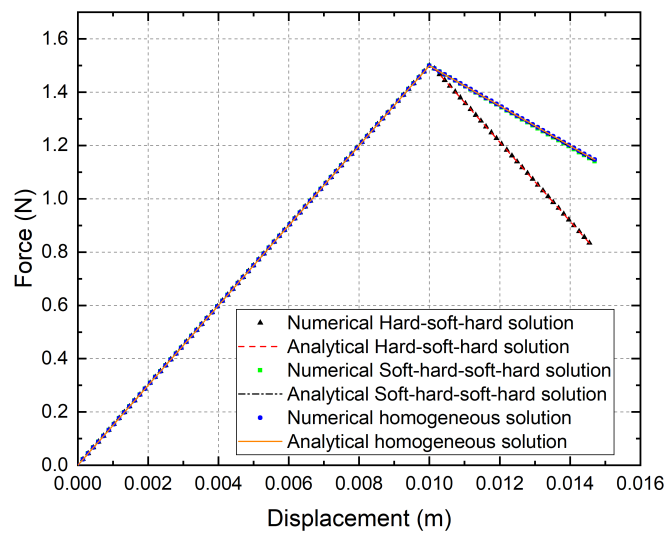


Figure 4.7: Force-displacement curves: analytical versus numerical results (analytical results from [8])

It is obvious from Fig. 4.7 and Fig. 4.8 that the 1D and the 2D second gradient finite elements provide the same results with the analytical solutions. Finally, Fig 4.9 and 4.10 present the ccumulative equivalent plastic strain distribution for the two localized solutions (numerical results with the 2D second gradient finite element).

Mesh independency is then investigated using three mesh refinements for 1 D problem (40, 80 and 160 9-node quadrilateral finite elements). The symmetrical localized solution is trig-
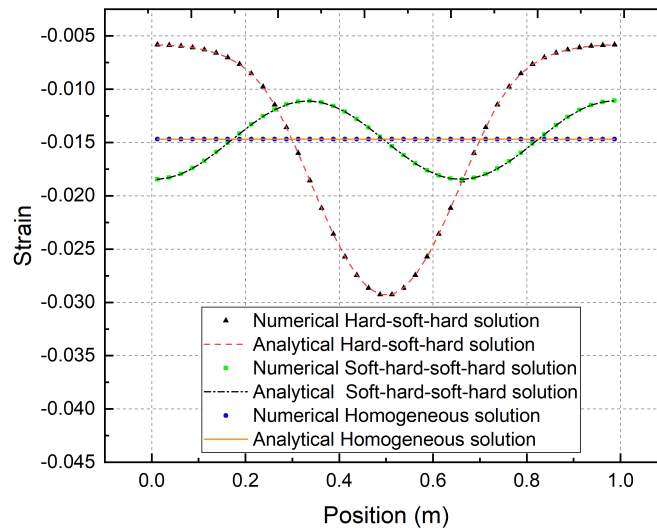
Figure 4.8: Strain distribution: analytical versus numerical results (analytical results from [8])



(a) Hard-soft-hard solution

(b) Soft-hard-soft-hard solution

Figure 4.9: Cumulative equivalent plastic strain distribution (numerical results with the 1D second gradient finite element)



(a) Hard-soft-hard solution

(b) Soft-hard-soft-hard solution
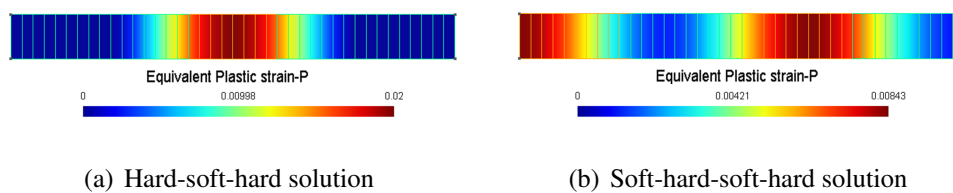
Figure 4.10: Cumulative equivalent plastic strain distribution (numerical results with the 2D second gradient finite element)

gered by the introduction of material imperfection (1 % strength reduction) located in the center of the bar. The global response in terms of force versus displacement is shown in Fig 4.11 and the strain distribution in Fig 4.12. Both figures demonstrate clearly the mesh independency of the second gradient model.
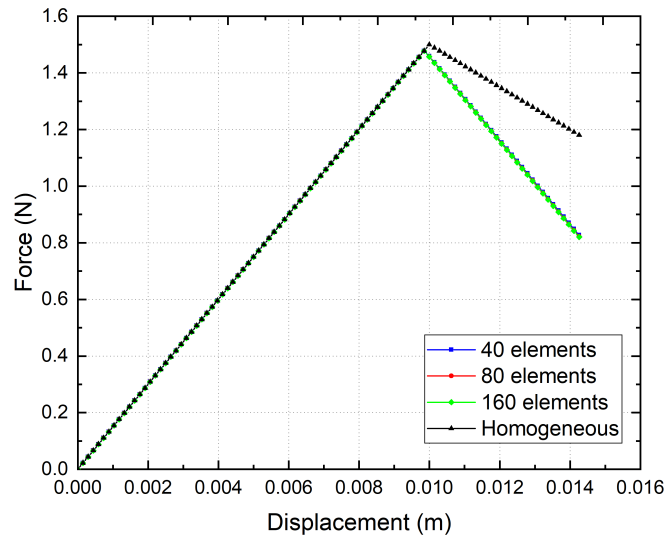
Figure 4.11: Force versus displacement: numerical results with the 2D second gradient finite element for different meshes
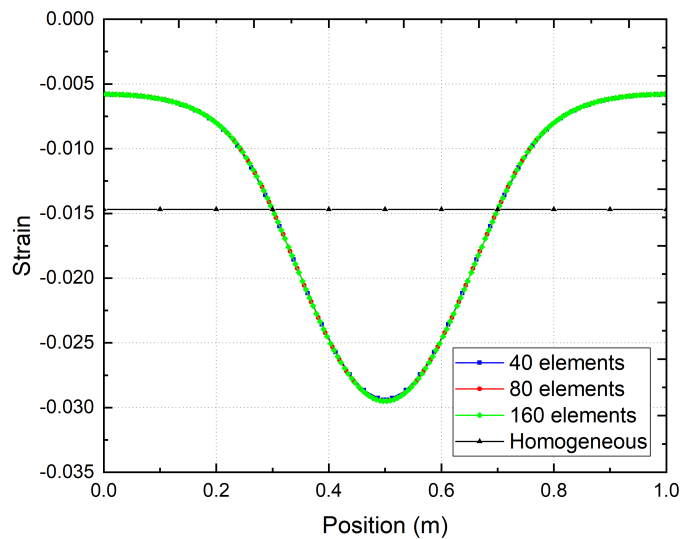


Figure 4.12: Strain distribution: numerical results with the 2D second gradient finite element for different meshes

## 4.4 One-dimensional linear perturbation analysis using viscoplastic model in a second gradient continuum

A 1D linear perturbation analysis for a viscoplastic model in a second gradient medium is presented hereafter. The basic steps presented in section 3.4 are again followed. Other examples of linear perturbation analysis in enhanced models can be studied in [114, 115, 116].

### 4.4.1 Fundamental relations

**Equilibrium equation**

For the 1D case, the equilibrium equation is (see also equation 4.39):

$$\frac{\partial \sigma}{\partial x} - \frac{\partial^2 \Sigma}{\partial x^2} = 0 \tag{4.46}$$

**Constitutive laws**

As mentioned in section 4.3, the second gradient model uses two constitutive laws, for the first and the second gradient terms:

$$\dot{\sigma} = E\left(\dot{\gamma} - \dot{\gamma}^{vp}\right)$$
$$\dot{\gamma}^{vp} = \frac{1}{\eta\sigma_{max}}[\sigma - \sigma_{max} - A_2(\gamma - \gamma_{lim})]^N \tag{4.47}$$
$$\Sigma = D_{sg}\frac{\partial^2 u}{\partial x^2}$$

where $N \geqslant 1$ is a calibration parameter (for simplicity, $N = 1$ is again assumed hereafter).

### 4.4.2 Perturbation analysis

As before, the perturbation in displacements $\delta u$ is assumed to be periodic form and imposed on the homogeneous state such that

$$\delta u = \hat{u}e^{\omega t + ikx} \tag{4.48}$$

with $k$ the wave number, $\omega$ the growth rate and the amplitude $\hat{u}$ is of order $\hat{u} \ll 1$. The following equations can be found:

$$\delta\dot{u} = \frac{\partial\delta u}{\partial t} = \omega\delta u$$

$$\delta\gamma = \frac{\partial\delta u}{\partial x} = ik\delta u$$

$$\delta u_{,xxxx} = k^4\delta u$$

$$\delta\dot{u}_{,xxxx} = \frac{\partial u_{,xxxx}}{\partial t} = \omega k^4\delta u \qquad (4.49)$$

$$\delta\dot{\gamma} = \frac{\partial\delta\gamma}{\partial t} = ik\omega\delta u$$

$$\delta\dot{\gamma}_{,x} = \frac{\partial\delta\dot{\gamma}}{\partial x} = -k^2\omega\delta u$$

Starting from the equilibrium equation (4.46), it is perturbed such that

$$\delta\sigma_{,x} - D_{sg}\delta u_{,xxxx} = 0 \qquad (4.50)$$

Its rate form it gives

$$\delta\dot{\sigma}_{,x} - D_{sg}\delta\dot{u}_{,xxxx} = 0 \qquad (4.51)$$

As before, the next step is to perturb the expression of the plastic strain rate given by the second equation in (4.47) ($N = 1$ is assumed). Differentiating both sides of the equation with respect to $x$ gives

$$\delta\dot{\gamma}_{,x}^{vp} = \frac{k^4 D_{sg} + k^2 A_2}{\eta\sigma_{max}}\delta u \qquad (4.52)$$

Differentiating both sides of the first gradient constitutive law in equation (4.47) combined with equation (4.51) gives

$$\delta\dot{\gamma}_{,x}^{vp} = -k^2\omega\delta u - \omega k^4\frac{D_{sg}}{E}\delta u \qquad (4.53)$$

Equating equations (4.52) and (4.53) and considering that $\delta u$ is not zero, the characteristic stability equation becomes

$$\omega = -\frac{k^2 D_{sg} + A_2}{\eta\sigma_{max}\left(1 + k^2\frac{D_{sg}}{E}\right)} \qquad (4.54)$$

The following conclusions can be found:

• As before, for $\omega$ real and positive the perturbation grows with time and instability is possible. For $\omega$ real and negative the perturbed solution decays with time and the homogeneous solution is stable.

90

- When the second gradient parameter $D_{sg}$ vanishes, equation (4.54) degenerates into equation (3.40).

- While $D_{sg} \neq 0$, the solution becomes unstable when $-k^2 D_{sg} - A_2 > 0$. A critical wave number is thus determined $k = \sqrt{\frac{-A_2}{D_{sg}}}$ linked with the internal length of the second gradient medium, see also [8].

To further investigate how the relation between the growth rate $\omega$ and the wave number $k$ as well as the second gradient parameter $D_{sg}$, keeping $E$, $A_2$, $\eta$, $\sigma_{\max}$ constant, the influence of the wavenumber $k$ and of the second gradient parameter $D_{sg}$ on the growth rate $\omega$ is shown in Fig 4.13. Main findings are illustrated as follows:
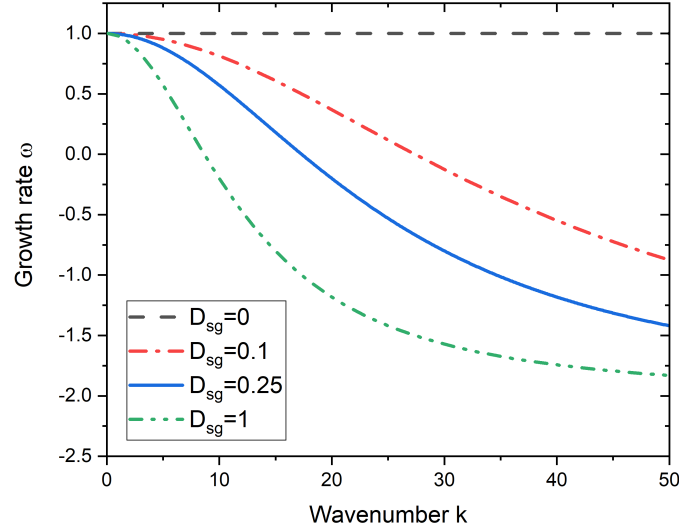


Figure 4.13: The influence of the wavenumber $k$ and of the second gradient parameter $D_{sg}$ on the growth rate $\omega$

- Perturbations of large wavelength (small wavenumber $k$) tend to grow faster while perturbations of small wavelength (large wavenumber $k$) tend to grow slower.

- Increasing the second gradient parameter $D_{sg}$ slows the perturbation growth. The range of the growth rate is limited between $-\frac{E}{\eta \sigma_{max}} \leq \omega \leq -\frac{A_2}{\eta \sigma_{max}}$, irrespective of the second gradient parameter $D_{sg}$ and the wavenumber $k$.

The range of the growth rate is derived in the following way. Equation (4.54) is multiplied with the denominator $\eta \sigma_{max} \left(1 + k^2 \frac{D_{sg}}{E}\right)$ and after some algebra we arrive at a quadratic

equation for $k$:

$$\left(\omega\eta\sigma_{max}\frac{D_{sg}}{E} + D_{sg}\right)k^2 + (\omega\eta\sigma_{max} + A_2) = 0 \tag{4.55}$$

Since at least one solution exists for $k$, the discriminant should be equal or larger than $0$.

$$\Delta = -4\left(\omega\eta\sigma_{max}\frac{D_{sg}}{E} + D_{sg}\right)(\omega\eta\sigma_{max} + A_2) \geqslant 0 \tag{4.56}$$

In the following, the effect of different parameters in the global and local response of a viscoplastic boundary value problem in a classical and in a second gradient medium are studied.

## 4.5 One-dimensional numerical study

### 4.5.1 Initial imperfection

The 1D analysis done hereafter considers a certain length (in the middle of the bar) of weak elements, see Fig 4.14. Inside the initial imperfection (shaded part), the yield strength is reduced by $a\%(0 < a < 20)$. A comparison is first performed with and without the second
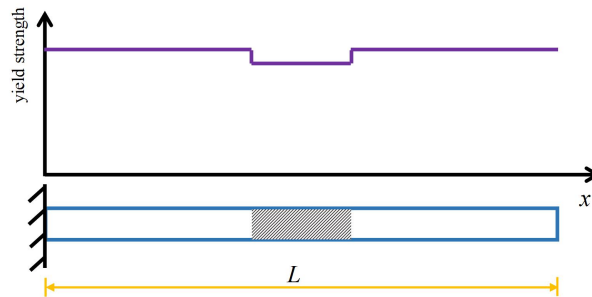


Figure 4.14: Schematic illustration of initial imperfection inside the 1D bar

gradient terms. With $1\%$ strength reduction in the weak elements, the global response and strain distribution for the viscoplastic model in a classical and in a second gradient medium are depicted in Fig 4.15 (the homogeneous solution is also shown). It can be observed that there is essentially no difference on the global response between the two localized solutions and the homogeneous solution. Differences however appear for the strain distribution between the three solutions 4.15(b). Without second gradient, the equivalent plastic strain concentrates in the imperfection. This is not the case for the second gradient model, where strain is regularized and varies gradually.
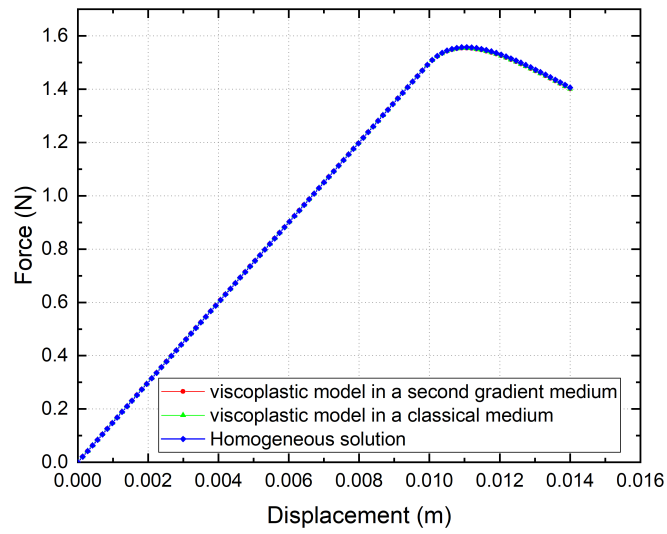
(a) Force versus displacement
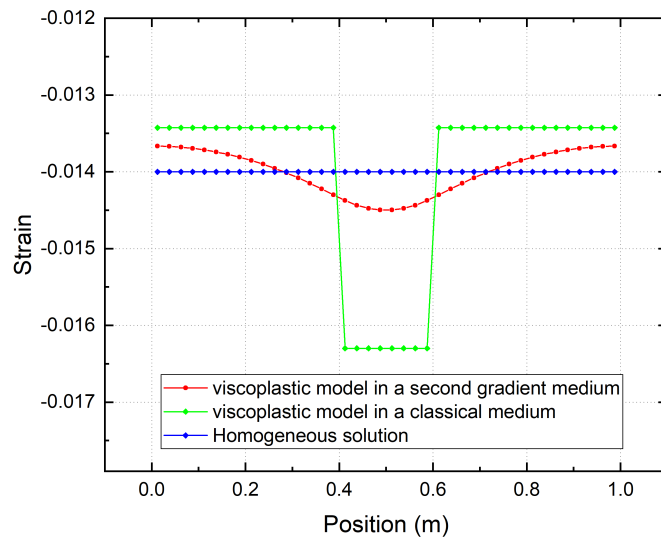


(b) Strain distribution

Figure 4.15: 1D numerical problem: comparison between the viscoplastic model in a classical and in a second gradient medium

The effect of initial imperfection on the formation of the localized zone is also shown considering viscoplasticity in a classical medium in Fig 4.16. The localized zone is determined exclusively by the imperfection. At the border of the initial imperfection, a strain jump exists.

93

In the viscoplastic second gradient model, the localized zone depends on the second gra-
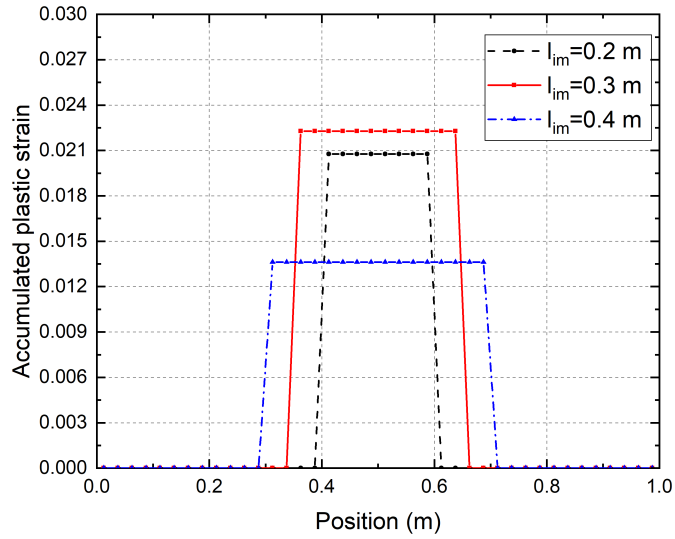


Figure 4.16: 1D numerical problem: effect of different lengths of initial imperfection on the localization zone for the viscoplastic model in a classical medium

dient parameter. Varying the second gradient parameter leads to different widths, as shown in Fig 4.17. In the second gradient model, the length of the localized zone is thus set by internal length introduced by second gradient parameter $D_{sg}$.

### 4.5.2 Random initialization

In the following, no initial imperfections are considered. Different velocities are imposed at one end of the bar and the force displacement response of the homogeneous solution is first given in Fig 4.18. It can be seen that the later the softening behaviour appears, the larger is the velocity. The viscoplastic model in a classical and in a second gradient medium provide the same results (homogeneous solution). The material parameters are listed in Table 4.1. Viscocity is considered equal $\eta = 15$ kPa $\cdot$ s and four velocities are selected, $v_1$=0.02 m/s, $v_2$=0.008 m/s, $v_3$=0.002 m/s.

When a random initialization is applied just after the peak, localized solutions are obtained with the viscoplastic model in a second gradient medium. Two of them along with the homogeneous solution are given Fig 4.19. In terms of global response, the three solutions
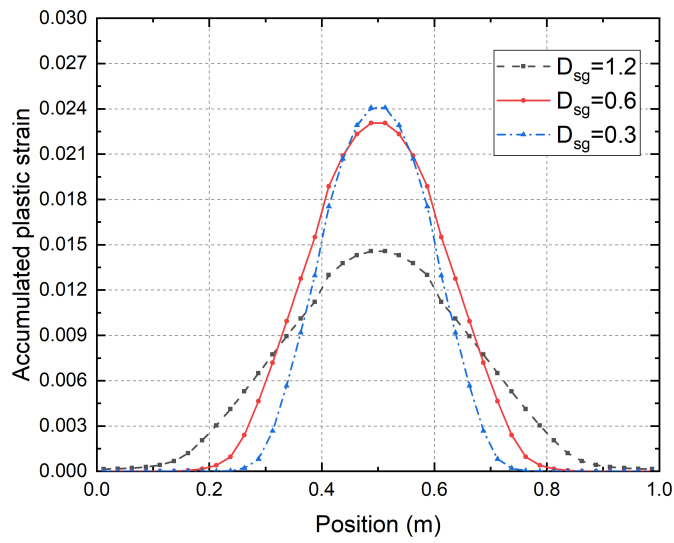
Figure 4.17: 1D numerical problem: effect of the second gradient parameter ($D_{sg}$) on the localization zone for the viscoplastic model in a second gradient continuum
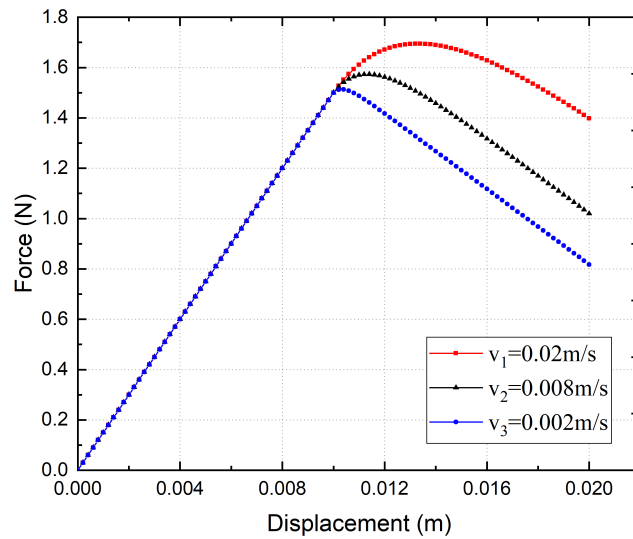


Figure 4.18: 1D numerical problem: force-displacement curves for different velocities

seem similar near the peak, differences grow as the loading increases. Local results (distribution of the accumulated equivalent plastic strain), however show significant differences and different localization patterns, see Fig 4.20.
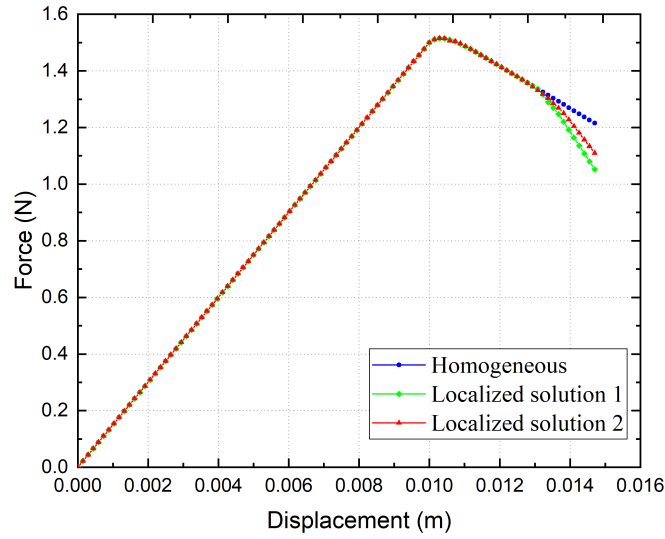
Figure 4.19: 1D numerical problem: force-dispacement curves of different localized solutions obtained with random initialization using the viscoplastic model in a second gradient medum



(a) Homogeneous solution　　　(b) Localized solution 1　　　(c) Localized solution 2
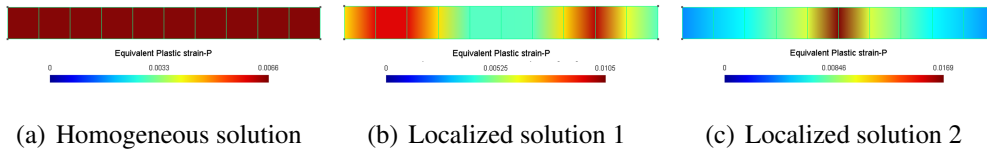
Figure 4.20: 1D numerical problem: accumulated equivalent plastic strain distributions of different localized solutions obtained with random initialization using the viscoplastic model in a second gradient medium, last loading step

## 4.6 Two-dimensional numerical study

### 4.6.1 Effect of mesh refinements

Fig 4.21 presents the results of the EVP-MCC model (whose viscosity parameter is a priori validated from experiments) in a classical medium; a pathological mesh dependency appears. The same analysis considering the EVP-MCC model in a second gradient medium shows that the results are mesh independent in terms of number of elements, see Fig 4.22.

In addition to the mesh size effect, it is recognized that mesh independent solution contains mesh-alignment independence. Therefore some computations are also performed for dif-

(a) 10 ×20 elements      (b) 20 × 40 elements      (c) 30 × 60 elements
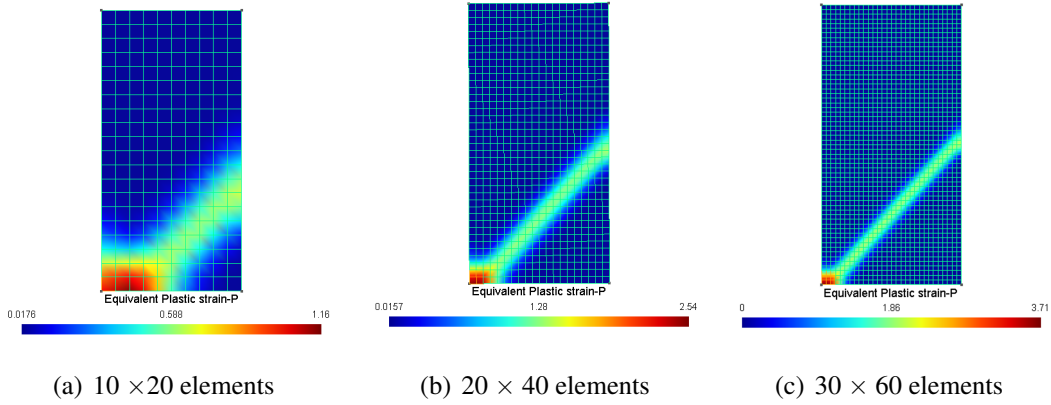
Figure 4.21: Biaxial test: distribution of accumulated equivalent plastic strain of the EVP-MCC model in a classical medium for different mesh sizes, last loading step



(a) 10 × 20 elements      (b) 20 × 40 elements      (c) 30 ×60 elements
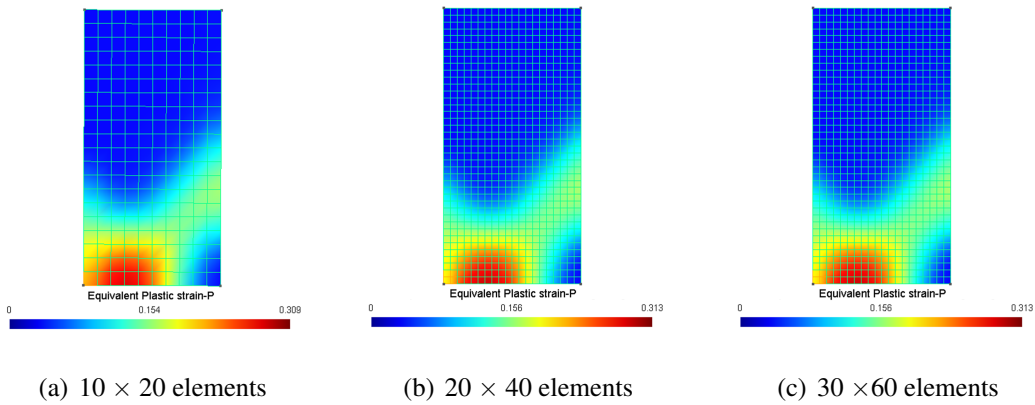
Figure 4.22: Biaxial test: distribution of accumulated equivalent plastic strain of the EVP-MCC model in a second gradient medium for different mesh sizes, last loading step

ferent mesh alignments, including a biased mesh depicted in Fig 4.23(b) and non-structured mesh depicted in Fig 4.23(c). Since shear band is more prone to occur align with the inclined straight line of the mesh, however, from Fig 4.24, mesh-alignment independent results are clearly illustrated.

## 4.6.2   Effect of localization and number of imperfections

The role of imperfections (weak elements) is examined in the following analysis with $20 \times 40$ quadrilateral elements. The localization and number of the imperfections varies, as shown in Fig 4.25.

(a) Structured mesh         (b) Biased mesh         (c) Non structured mesh
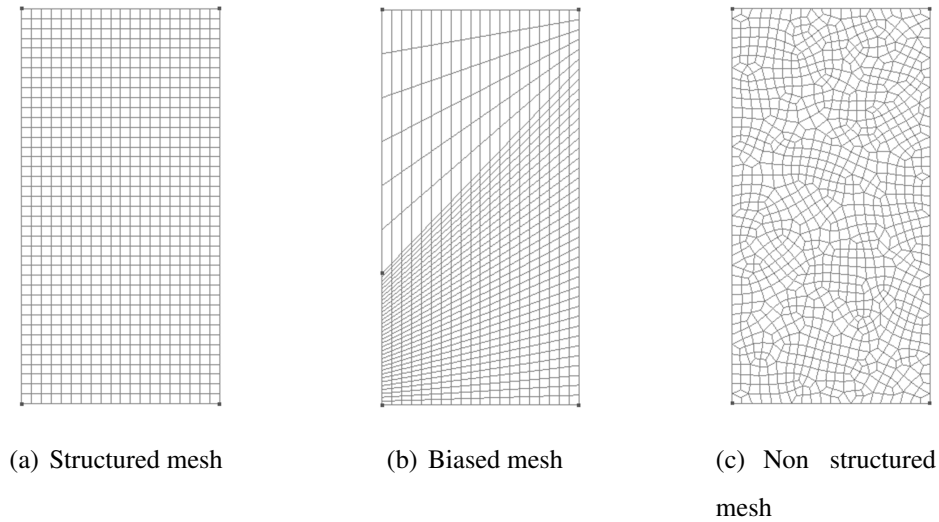
Figure 4.23: Three different types of mesh alignments in biaxial test



(a) Structured mesh        (b) Biased mesh        (c) Non structured mesh
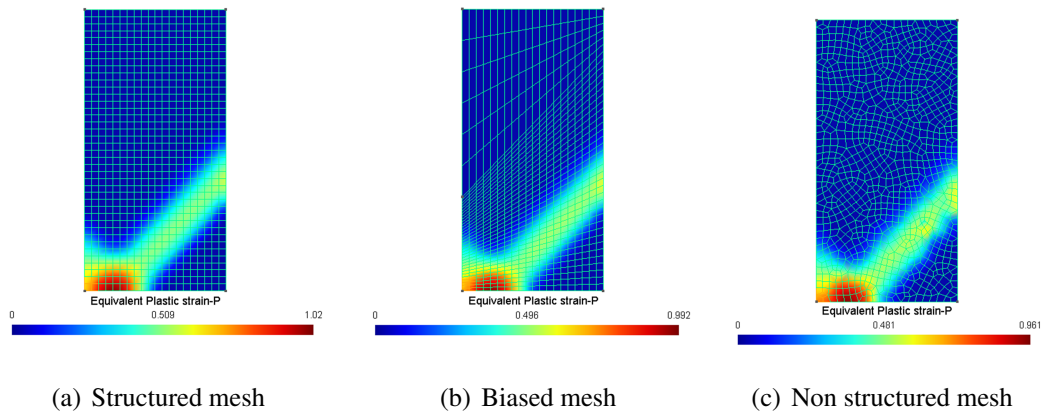
Figure 4.24: Biaxial test: distribution of accumulated equivalent plastic strain of the EVP-MCC model in a second gradient medium for different mesh orientations, last loading step

- Case A: $2\%$ four-element imperfection located on the left corner of the sample;

- Case B: $2\%$ four-element imperfection located in the middle of the left side,

- Case C: two $2\%$ four-element imperfection located on the left side of the sample.

where $2\%$ represents the assigned consolidation pressure $p_c$ reduction compared with the normal value.

The global response in terms of applied displacement and reaction forces is shown in Fig 4.26. Overall, differences are small and more pronounced near the peak.

The accumulated equivalent plastic strain for different loading steps and for cases A, B and C are given in Fig 4.27, Fig4.28 and Fig4.29, respectively. Near the peak, the shear band

(a) Case A　　　　　　　(b) Case B　　　　　　　(c) Case C
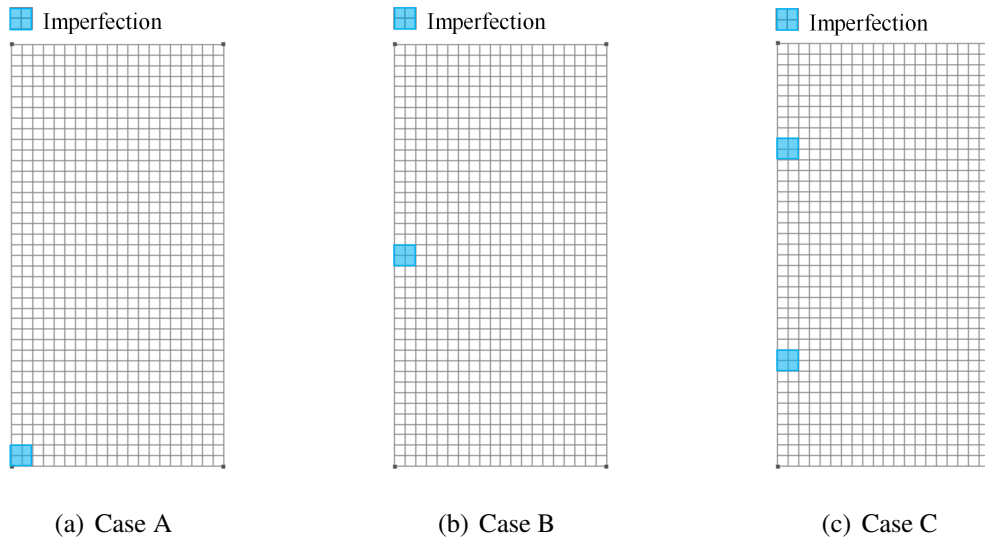
Figure 4.25: Biaxial test: localization and number of imperfections
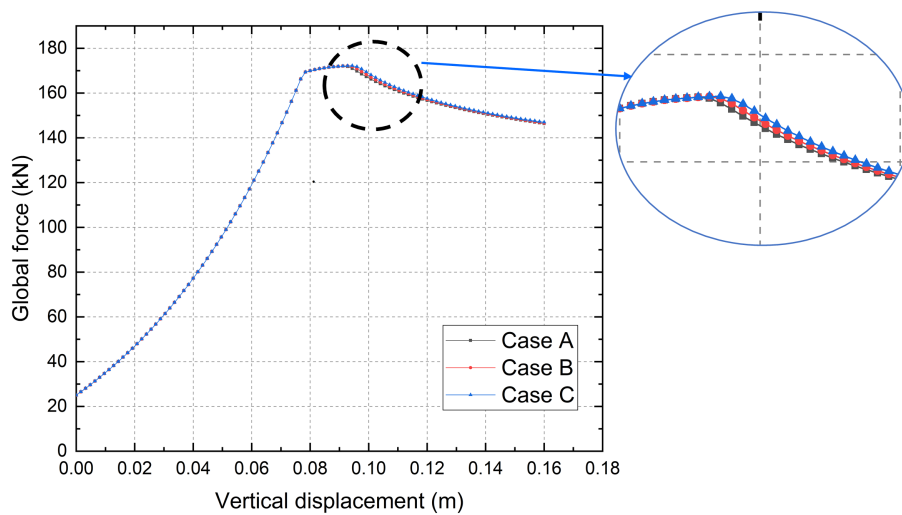


Figure 4.26: Biaxial test: force-displacement curves for different imperfections

presents different forms, see 4.27(a), Fig 4.28(a) and Fig 4.29(a). For case A, localization initiates in two or more crossed sections and several shear bands are visible. With increasing loading, one of them remains active and propagates along the original directions, while the others disappear, see also [84]. In all cases, the shear band width is similar.

(a) U=0.096        (b) U=0.128        (c) U=0.16
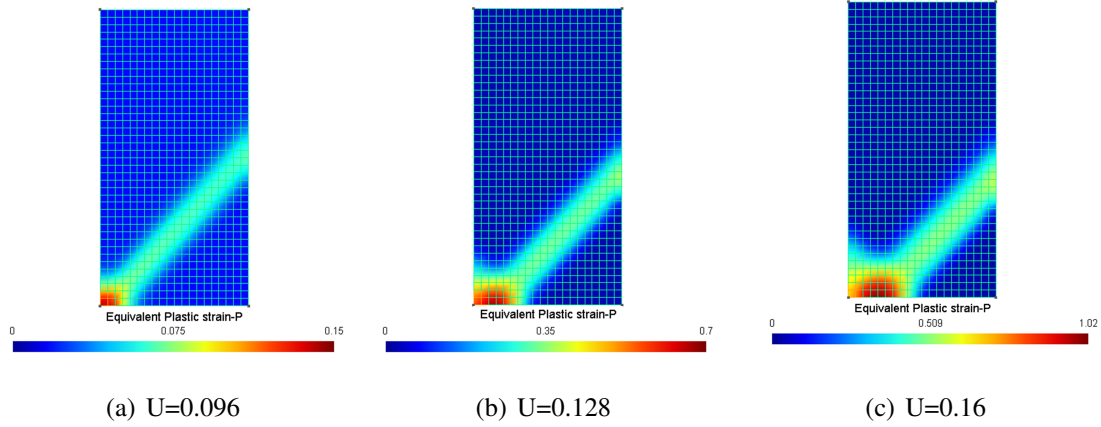
Figure 4.27: Biaxial test: onset and evolution of the shear band (distribution of accumulated equivalent plastic strain), case A



(a) U=0.096        (b) U=0.128        (c) U=0.16
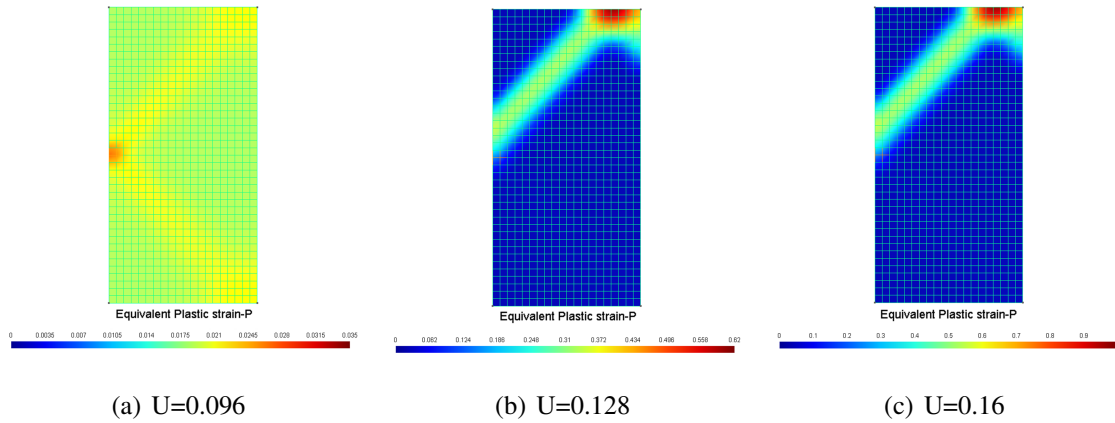
Figure 4.28: Biaxial test: onset and evolution of the shear band (distribution of accumulated equivalent plastic strain), case B

### 4.6.3 Effect of second gradient parameter

In the second gradient model, the internal length is introduced by the second gradient parameter $D_{sg}$. Its effect is investigated hereafter considering a parametric analysis on the force displacement response and the accumulated equivalent plastic strain, see Fig 4.30 and Fig4.31, respectively. It is observed that the width of shear band is governed by the applied $D_{sg}$. The larger the value of $D_{sg}$ is, the steeper is the slope of the post-peak global response. Furthermore, a parametric study is performed to find qualitatively the relation between the second gradient parameter and the shear band width. As for the 1D case, it is found that the shear band thickness is proportional to the square root of the second gradient parameter, Fig 4.32. This is useful in order to choose a priori the second gradient parameter for the desired

(a) U=0.096        (b) U=0.128        (c) U=0.16
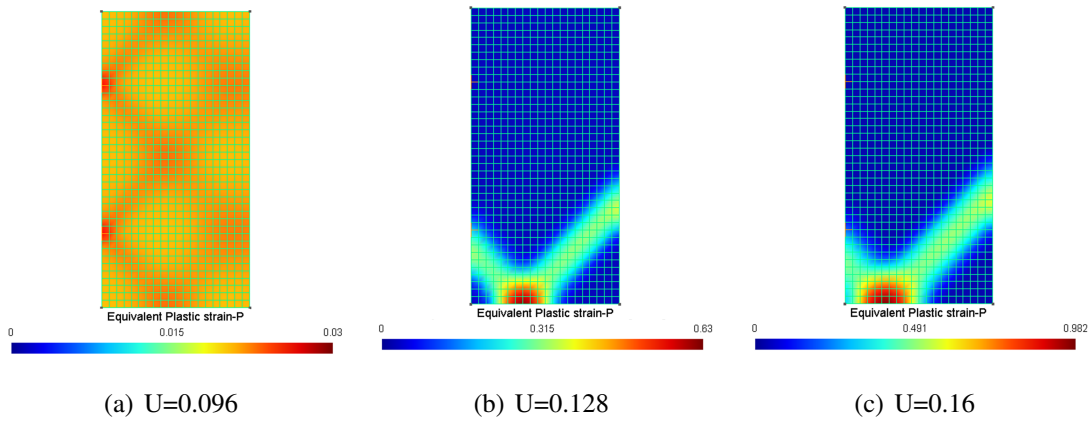
Figure 4.29: Biaxial test: onset and evolution of the shear band (distribution of accumulated equivalent plastic strain), case C

shear band width.
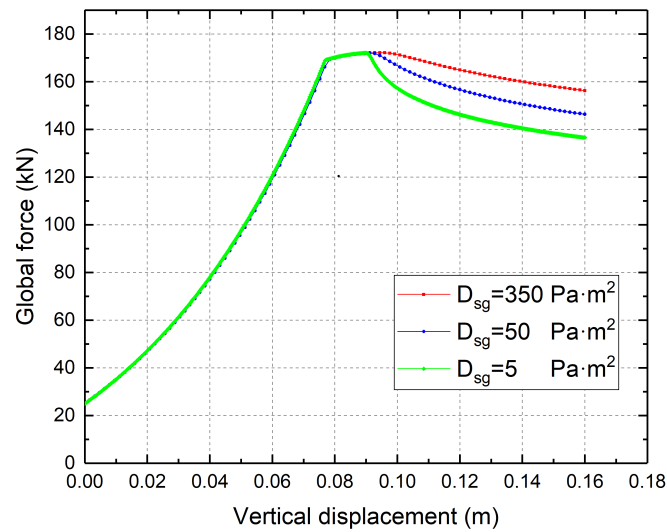


Figure 4.30: Biaxial test: force-displacement curves for different second gradient parameters

Finally, the evolution of the distribution of the accumulated equivalent plastic strain for different loading steps is shown in Fig 4.33. With increasing loading, the shear band width grows and the slope of the post-peak region decreases (see also Fig 4.30).

(a) $D_{sg} = 350 \, \mathrm{Pa} \cdot \mathrm{m}^2$     (b) $D_{sg} = 50 \, \mathrm{Pa} \cdot \mathrm{m}^2$     (c) $D_{sg} = 5 \, \mathrm{Pa} \cdot \mathrm{m}^2$
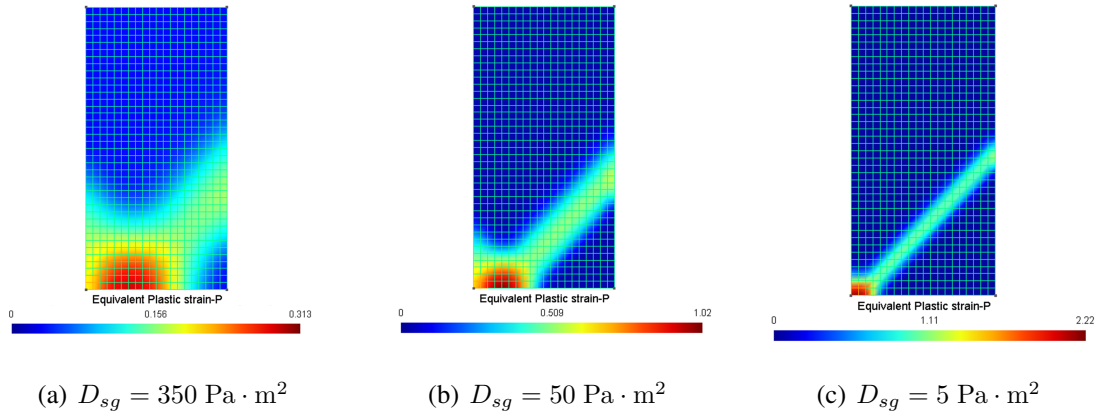
Figure 4.31: Biaxial test: distribution of accumulated equivalent plastic strain for different second gradient parameters, last loading step
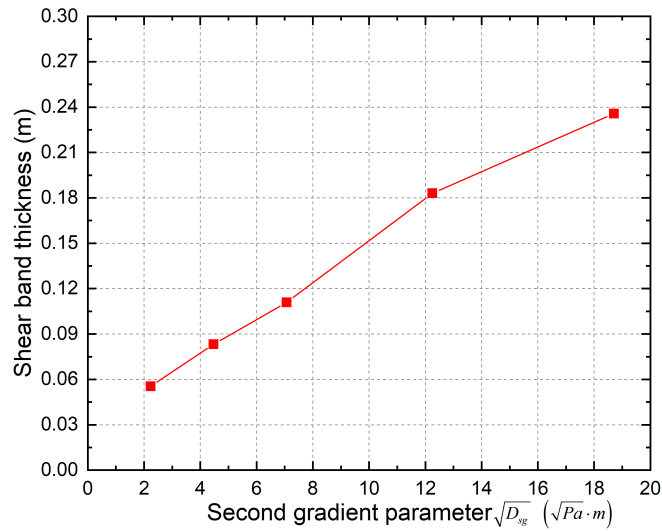


Figure 4.32: Biaxial test: relationship between the square root of the second gradient parameter and the shear band thickness

## 4.7 Concluding remarks

This chapter presents simulations using the second gradient model with viscoplastic laws for strain localization problems. First, the implementation of a 1D and a 2D second gradient

<table>
<tr><td>(a) U = 0.12m</td><td>(b) U = 0.135m</td><td>(c) U = 0.16m</td></tr>
</table>
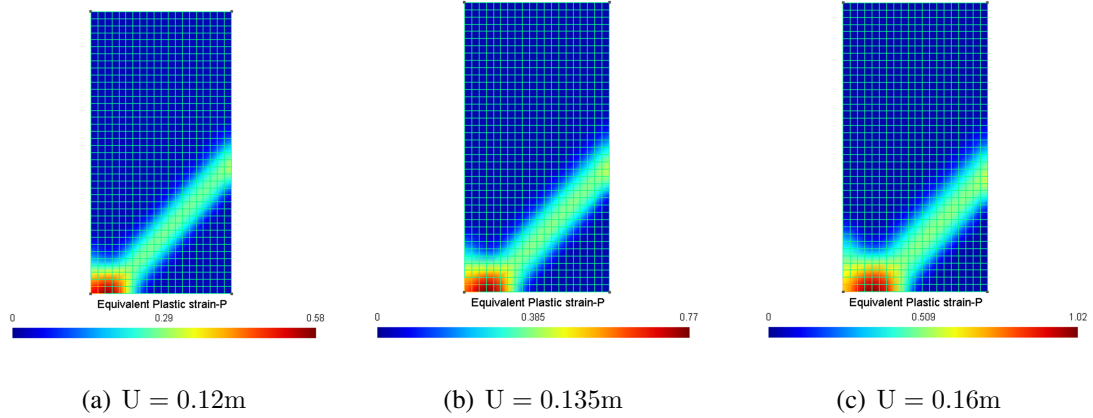
Figure 4.33: Biaxial test: distribution of the accumulated equivalent plastic strain for progressive loading steps

finite element in a Matlab based finite element software was presented and validated. Then, 1D and 2D strain localization problems are studied analytically (linear perturbation) and numerically. The main conclusions are as follows:

1. The 1D numerical study shows that the viscoplastic model in a classical medium does not provide objective results. Integrating it in a second gradient medium regularizes the problem. Different solutions are obtained using random initialization indicating the non-uniqueness of the solution.

2. The 1D linear perturbation analysis for a viscoplastic model in a second gradient medium shows that the stability is conditionally guaranteed and the growth rate is influenced by the wave number and the second gradient parameter. Decrease of the growth rate can be achieved by increasing the second gradient parameter or increasing the wave number.

3. In the 2D study, the viscoplastic model in a second gradient medium provides results that do not depend on the mesh size and the mesh alignment. The number and localization of imperfections influence the shear band propagation and evolution. The shear band width is mainly governed by the second gradient parameter $D_{sg}$.

# Chapter 5

# Case study: a shallow foundation

## 5.1 Introduction

The purpose of this chapter is to evaluate the behaviour of the second gradient model with a viscoplastic law for a boundary value problem. A shallow foundation is chosen with a brief review of its typical failure modes, the constitutive laws and the tension cut-off treatment adopted are also introduced. The model is then validated comparing the numerical obtained bearing capacity with analytical results. The use of a viscoplastic constitutive law in a second gradient medium is finally adopted to evaluate the failure modes and the post-peak progressive failure.

## 5.2 Bearing capacity and failure modes of a shallow foundation

The bearing capacity of a shallow foundation resting on homogeneous and dry soil is usually evaluated using the well-known equation proposed by Terzaghi [117]

$$q_u = cN_c + \gamma D_f N_q + \frac{1}{2}\gamma B N_\gamma \tag{5.1}$$

in which $q_u$ is the bearing capacity, $D_f$ the foundation depth, $c$ the soil cohesion, $B$ the foundation width, $\gamma$ the soil effective unit weight and $N_q$, $N_c$, $N_\gamma$ (dimensionless quantities) the bearing capacity factors dependent on the friction angle. Further studies were also conducted to consider other factors, i.e. the foundation shape, the roughness condition at the

base, the load inclination and eccentricity, the groundwater level, etc.

Shear failure may occur within the soil supporting the footing. It is generally recognized that there are three principal shear failure modes: general shear failure, local shear failure and punching shear failure, see Fig 5.1, Fig 5.2 and Fig 5.3, repectively. In the following, the progressive shear failure of a shallow foundation is investigated, where the plastic strain gradually develops along the slip surface and over time, resulting in a gradual non-uniform distribution, the formation and development of a shear band.



(a) General shear failure mode          (b) Load versus vertical displacement response
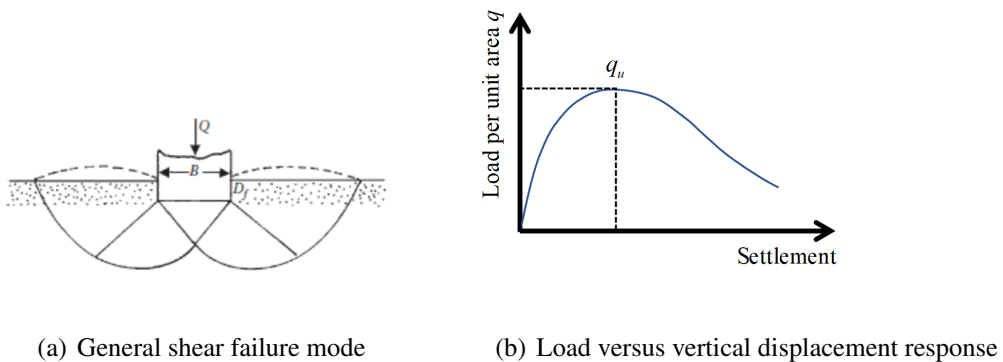
Figure 5.1: General shear failure of shallow foundation



(a) Local shear failure mode          (b) Load versus vertical displacement response
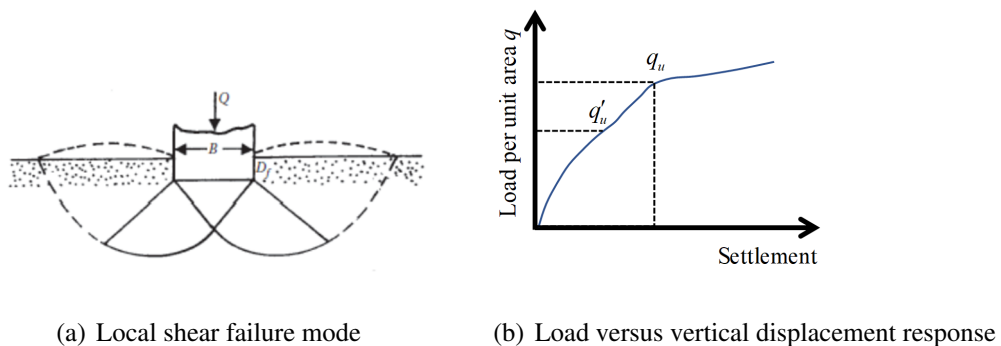
Figure 5.2: Local shear failure of shallow foundation

(a) Punching shear failure mode　　　(b) Load versus vertical displacement response
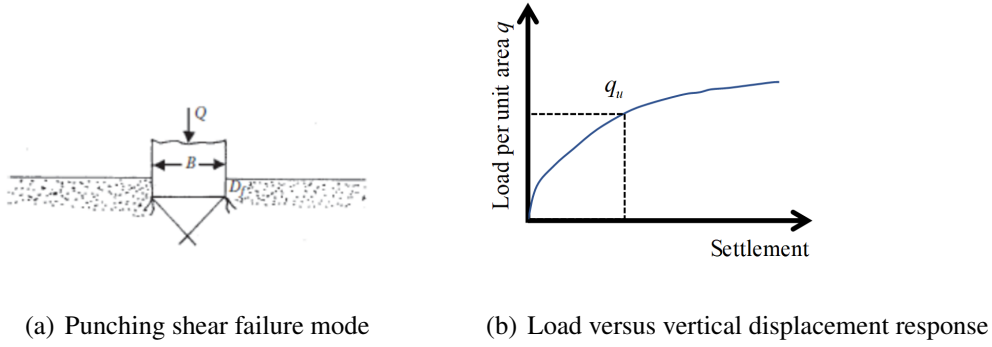
Figure 5.3: Punching shear failure of shallow foundation

# 5.3 Constitutive models

## 5.3.1 Drucker-Prager constitutive law

Without loss of generality and for the sake of simplicity, the Drucker-Prager (DP) yield criterion is adopted hereafter for the first gradient part (the second gradient constitutive law, as already mentioned in section 2.5.3 is linear elastic). Further study will be performed using more complex constitutive laws. The DP criterion was established as a generalization of the Mohr–Coulomb (MC) criterion [118]. It is commonly used for soils without suffering severe numerical difficulties as its yield surface is a circular cone. When the friction angle is equal to 0, the DP model reduces to Von Mises model. Its yield function is defined as:

$$f\left(\sigma, \alpha\right) = \frac{q}{\sqrt{3}} - 3\alpha p - \beta = 0 \tag{5.2}$$

where $p$ is the mean effective stress, $q$ the deviatoric stress, $\alpha$ and $\beta$ are related to the friction angle $\phi$ and the cohesion $c$ of the MC criterion. By fitting the MC criterion and assuming the surface to be circle in the octahedral plane under plane strain conditions, $\alpha$ and $\beta$ are defined as:

$$\alpha = \frac{\tan\phi}{\sqrt{(9 + 12\tan^2\phi)}} \quad \beta = \frac{3\left(c + h\xi_p\right)}{\sqrt{(9 + 12\tan^2\phi)}}$$

in which the accumulated deviatoric strain is defined as follows:

$$\xi_p = \int \dot{\xi}_p dt$$

where $\dot{\xi}_p = \left[\frac{1}{2}\dot{e}_{ij}^p \dot{e}_{ij}^p\right]^{\frac{1}{2}}$, $\dot{e}_{ij}^p = \dot{\varepsilon}_{ij}^p - \frac{1}{3}\dot{\varepsilon}_{kk}^p \delta_{ij}$

here $\dot{\varepsilon}_{ij}^p$ is the total plastic strain rate, $\dot{e}_{ij}^p$ the deviatoric plastic strain rate, $\delta_{ij}$ the Kronecker

delta and $h$ the hardening/softening modulus.

Considering a non-associative constitutive law, the potential function $g$ is expressed similar to the yield function (5.2)

$$g\left(\sigma,\zeta\right) = \frac{q}{\sqrt{3}} - 3\zeta p + constant \tag{5.3}$$

where $\zeta$ is related to the dilation angle $\psi$. Analogously to the definition of $\alpha$ in plane strain problems, it is defined as

$$\zeta = \frac{\tan\psi}{\sqrt{(9 + 12\tan^2\psi)}}$$

This viscoplastic DP model adopted the Perzyna type whose $\Phi(f)$ takes the power form as a common choice:

$$\Phi(f) = (\frac{f}{\sigma_0})^N \tag{5.4}$$

where the calibration parameter $N \geqslant 1$ is assumed to be 1 and $\sigma_0$ is the initial yield stress. Concerning the algorithm aspects, one can refer to section 2.2.3.

## 5.3.2 Tension cut-off

To avoid unrealistic tensile soil behaviour and numerical problems, a tension cut-off is considered and assumed to be rate-independent for simplicity.



Figure 5.4: Drucker-Prager model with tension cut-off

As seen in Fig 5.4, from A to B, the yield function obeys the classical DP law. From B to C, the tension cut-off writes

$$f_t = p - p_t \tag{5.5}$$

107

A flow rule is adopted for equation (5.5).

$$g_t = p \tag{5.6}$$

For a material whose coefficient $\alpha$ is not equal to 0, the tensile strength cannot exceed the value $p_t^{max}$

$$p_t^{max} = \frac{\beta}{3\alpha} \tag{5.7}$$

In the vicinity of the edge of two regions, a unique yield function $h_t$ representing the diagonal between $f = 0$ and $f_t = 0$ is defined by the following expression

$$h_t = q - a_t + b_t\,(p - p_t) \tag{5.8}$$

where $a_t$ and $b_t$ are two constants determined by

$$a_t = \beta + 3\alpha p_t$$
$$b_t = \sqrt{1 + (3\alpha)^2} - 3\alpha$$

The incremental plastic strain is given by:

$$\Delta\varepsilon^p = \Delta\lambda_t \frac{\partial f_t}{\partial \sigma} \tag{5.9}$$

The incremental stress and the incremental elastic strain are related as:

$$\Delta\sigma = \mathbf{C}(\Delta\varepsilon - \Delta\varepsilon^p) \tag{5.10}$$

No hardening or softening rule is considered in the domain of tensile failure. We recall the return mapping algorithm and assume that the consistency condition is satisfied at iteration $k + 1$, the Taylor series expansion implies:

$$f_t^{(k+1)} = f_t^{(k)} + \frac{\partial f_t}{\partial \sigma}\delta\sigma + \frac{\partial f_t}{\partial \lambda_t}\delta\lambda_t \tag{5.11}$$

Differentiation of equation (5.10) leads to the local stress increment $\delta\sigma$:

$$\delta\sigma = \mathbf{H}\left[\delta\varepsilon - \left(\frac{\partial g_t}{\partial \sigma} + \frac{\partial^2 g_t}{\partial \sigma \partial \lambda_t}\right)\delta\lambda_t\right] \tag{5.12}$$

where $\mathbf{H} = \left(\mathbf{C}^{-1} + \Delta\lambda_t \frac{\partial^2 g_t}{\partial \sigma^2}\right)^{-1}$

The combination of equation (5.11) and equation (5.12) provides the local increment of the plastic multiplier:

$$\delta\lambda_t = \frac{1}{\beta^t}\left(f_t^{(k)} + \frac{\partial f_t}{\partial \sigma}\mathbf{H}\delta\varepsilon\right) \tag{5.13}$$

108

where $\beta^t = \frac{\partial f_t}{\partial \sigma} \mathbf{H} \left( \frac{\partial g_t}{\partial \sigma} + \frac{\partial^2 g_t}{\partial \sigma \partial \lambda_t} \right) - \frac{\partial f_t}{\partial \lambda_t}$. The consistent tangent moduli is obtained by substituting equation (5.13) into equation (5.12)

$$\mathbf{C}^{ep} = \mathbf{H} - \frac{1}{\beta^t} \mathbf{H} \left( \frac{\partial g_t}{\partial \sigma} + \frac{\partial^2 g_t}{\partial \sigma \partial \lambda_t} \right) \frac{\partial f_t}{\partial \sigma} \mathbf{H} \tag{5.14}$$

The softening behaviour is described through a mobilised hardening modulus $h$. As shown in Fig 5.5, the yield strength is limited to range between $\beta^{peak}$ and $\beta^{resi}$.

The return mapping algorithm mentioned above is summarized in Box 5.1.
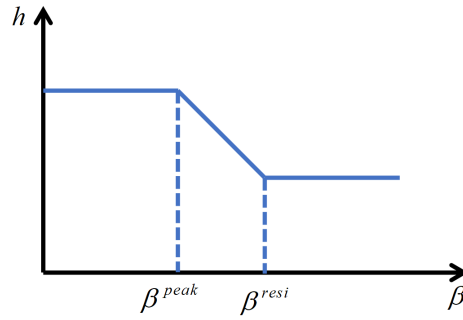


Figure 5.5: Mobilised hardening modulus $h$ of the DP law

Box 5.1: Implicit algorithm with tensile failure

1 Compute the trial state

$\sigma_{n+1}^{tr} = \mathbf{C}\Delta\varepsilon_{n+1} + \sigma_n$

If $f\left(\sigma_{n+1}^{tr}\right) \leq 0$

      Elastic behaviour

else:

      Plastic behaviour

            (1) Initialize the variables

            $\Delta\lambda_t^{(0)} = 0, \Delta\sigma_{n+1}^{(0)} = \mathbf{C}\left(\Delta\varepsilon - \Delta\lambda_t^{(0)}\frac{\partial g_t}{\partial\sigma}\right)$
            $f_t^{(0)} = \sigma_{n+1}^{(0)} - p_t$

            (2) Local iterations

                  1) Compute local variable increment

                  $\delta\lambda_t^{k+1} = \frac{1}{\beta^t}\left(f^{t(k)}\right)$
                  $\Delta\lambda_t^{(k+1)} = \delta\lambda_t^{(k+1)} + \Delta\lambda_t^{(k)}$

                2) Update variables

                $\Delta\sigma_{n+1}^{(k+1)} = C\left(\Delta\varepsilon - \Delta\lambda_t^{(k+1)}\frac{\partial g_t}{\partial\sigma}\right)$

                3) Compute residuals and check convergence

                $r^{(k)} = f_t\left(\sigma_{n+1}^{(k+1)}\right)$

                IF $r^{(k)} > Tol$

                    Set $k \leftarrow k + 1$ and go to (2).

                ELSE $(\cdot)_{n+1} \leftarrow (\cdot)_{n+1}^{(k+1)}$

## 5.4 FE model of shallow foundation

### 5.4.1 Geometry and boundary conditions

Only half of the geometry is considered for the numerical simulations taking advantage of symmetry, see Fig 5.6. The foundation width is denoted by B. In order to eliminate boundary effects, the lateral dimension is extended to $12.5B$ in the horizontal direction and to $12.5B$ in the vertical direction. The interface conditions are considered rough (fixed

horizontal displacements at the bottom of the footing). The bottom of the whole domain is fully fixed and the lateral displacements are constrained on the left and the right side. A uniform vertical displacement is applied beneath the footing with constant velocity as a rigid footing is assumed here.
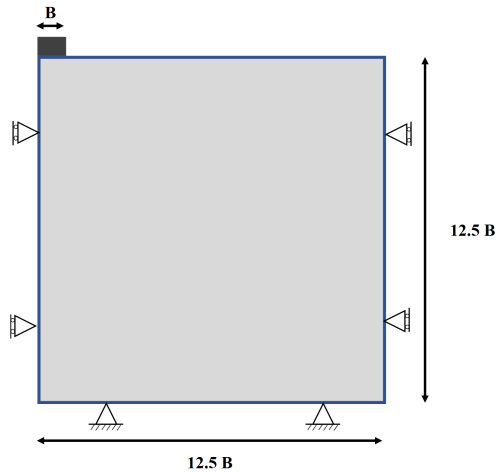


Figure 5.6: Shallow foundation: geometry and boundary conditions

Classical Q8 (without second gradient) and Q9 (with second gradient terms) finite elements are used for the mesh. Three mesh refinements (called hereafter coarse mesh, dense mesh and very dense mesh) are adopted, Fig 5.7. The mesh is refined around the potential strain concentration area.



(a) Coarse mesh      (b) Dense mesh      (c) Very dense mesh
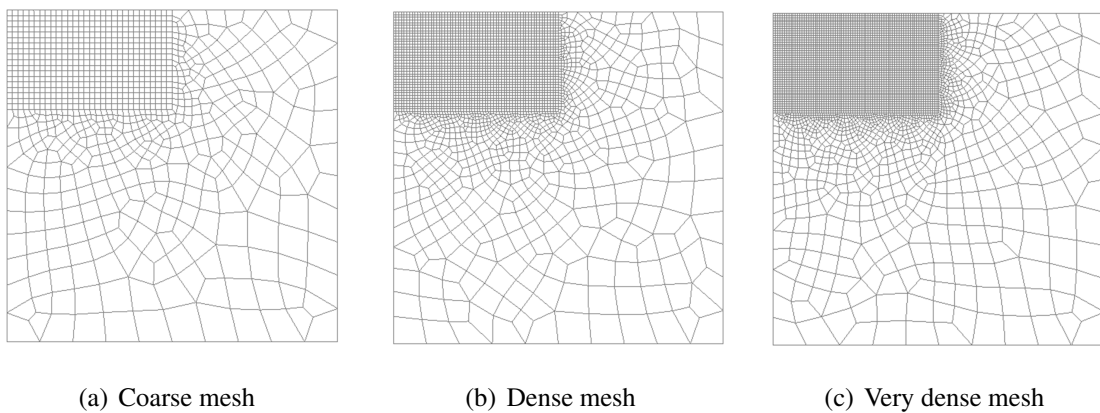
Figure 5.7: Shallow foundation: three mesh refinements

## 5.4.2 Initial stress state

When accounting for the weight of the soil, the initial stress state is usually generated under geostatic condition (or $K_0$ condition).

$$\sigma_{zz} = \gamma z$$
$$\sigma_{yy} = \sigma_{xx} = K_0 \sigma_{zz}$$

(5.15)

where $\gamma$ is the unit weight of the soil below the foundation, determined from the ground water table, $z$ is the depth. The choice of $K_0$ is dependent on the friction angle (for sand) and plasticity index $I_p$ (for clay), it is expressed as:

- For sand, $K_0$ is

$$K_0 = (1 - \sin\phi')$$

(5.16)

where $\phi'$ is the friction angle.

- For clay, $K_0$ is assumed to be correlated with the plasticity index

$$K_0 = 0.19 + 0.233 \, \text{log} I_p$$

(5.17)

with $I_p$ in %

Soil can be in an overconsolidated state (with a load applied and subsequently removed). The coefficient $K_{0R}$ is defined as

$$K_{0R} = K_0 OCR^{c_\lambda}$$

(5.18)

where $OCR$ is the overconsolidation ratio and the characteristic parameter $c_\lambda$ refers to the empirical relation introduced in [119].

## 5.4.3 Finite element model validation

To validate the FE model in a second gradient continuum with regard to bearing capacity of shallow foundation as well as provide some preliminary ideas for the choice of the second gradient parameter $D_{sg}$, the numerical results are compared with the analytical results provided by equation (5.1) for different friction angles (an associative law is adopted and thus the dilation angle is considered equal to the friction angle). The coefficients $N_q$, $N_\gamma$ and $N_c$

of equation (5.1) are determined as follows:

$$N_q = \frac{\exp^2\left(\frac{3}{4}\pi - \frac{\varphi}{2}\right)\tan\varphi}{2\cos^2\left(\frac{\pi}{4} + \frac{\varphi}{2}\right)}$$

$$N_c = (N_q - 1)\cot\varphi \qquad (5.19)$$

$$N_\gamma = \frac{1}{2}\left(\frac{K_{py}}{\cos^2\varphi} - 1\right)\tan\varphi$$

where $K_{py}$ denotes passive pressure coefficient. As seen from equation (5.19), the bearing capacity factors are function of the friction angle. Three friction angles are selected hereafter and the corresponding bearing factors [120] are listed in Table 5.1. The soil properties are given in Table 5.2 and maximum tensile strength is set $10$kPa.

Table 5.1: Terzaghi's bearing capacity factors for different friction angles

| $\varphi$ | $N_c$ | $N_q$ | $N_\gamma$ |
|---|---|---|---|
| $0°$ | 5.70 | 1.00 | 0.00 |
| $10°$ | 9.61 | 2.69 | 0.56 |
| $15°$ | 12.86 | 4.45 | 1.52 |

Table 5.2: Soil parameters of the Dp model in a second gradient continuum

| | Parameter | Value |
|---|---|---|
| Elastic parameters | Young's modulus $E$ | $35000\,\text{kPa}$ |
| | Poisson's ratio $\nu$ | 0.3 |
| Plastic parameters | Cohesion $c$ | $20\,\text{kPa}$ |
| | Friction angle $\phi$ | $0°,10°,15°$ |
| | Dilatation angle $\psi$ | $0°,10°,15°$ |

The numerical bearing capacity is calculated from the following formula:

$$q_u^{Num} = \frac{\sum_{i=1}^{n} F_r^i}{B} \qquad (5.20)$$

where $F_r^i$ is the $i_{th}$ nodal reaction force and $B$ the footing width.

Among all the adopted second gradient parameters varying from $5 \, \text{Pa} \cdot \text{m}^2$ to $5000 \, \text{Pa} \cdot \text{m}^2$, the smallest relative error between numerical bearing capacity and analytical one is provided when $D_{sg} = 50 \, \text{Pa} \cdot \text{m}^2$. With $D_{sg} = 50 \, \text{Pa} \cdot \text{m}^2$, a relative error within $2.90\%$ is indicated in Table 5.3.

Table 5.3: Comparison between analytical and numerical bearing capacities

| $\phi(°)$ | Analytical $q_u^{Ana}$(kPa) | Numerical $q_u^{Num}$(kPa) | Relative error $\delta(\%)$ |
|---|---|---|---|
| 0 | 114.000 | 116.413 | 2.12 |
| 10 | 192.200 | 187.140 | $-2.63$ |
| 15 | 257.200 | 249.874 | $-2.85$ |

Note: the relative error is calculated by the following formula

$$\delta = \frac{q_u^{Num} - q_u^{Ana}}{q_u^{Ana}} \times 100\%$$

Global response for different friction angles is given in Fig 5.8. The bearing capacity increases gradually until a constant value is attained. Moreover, increasing the friction angle results in an increase of the bearing capacity of the shallow foundation. The accumulated equivalent plastic strain distribution and evolution shows that the slip surface starts from the edge of the footing and forms a wedge-shaped region below the loading area. Then, the slip surface spreads upwards as well as outwards to the ground. As the angle of friction increases, the affected zone becomes larger both in the horizontal and vertical direction, see Fig 5.9.

## 5.5 Post-peak response using the second gradient model with a viscoplastic law

Increasing plastic strain results in strength reduction for soils such as dense sand, overconsolidated soft soil etc. This strain-softening behaviour and progressive failure happens as intense strain is localized in a limited thickness zone.

---

[1]$U = 0.1$m means the plot is taken when the applied vertical displacement is equal to $0.1$ m
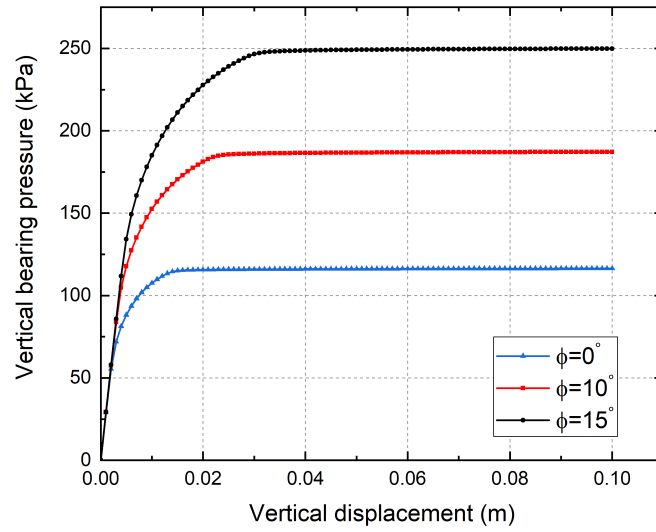
Figure 5.8: Shallow foundation: vertical pressure versus displacement for different friction angles



(a) $\phi = 0°$        (b) $\phi = 10°$        (c) $\phi = 15°$
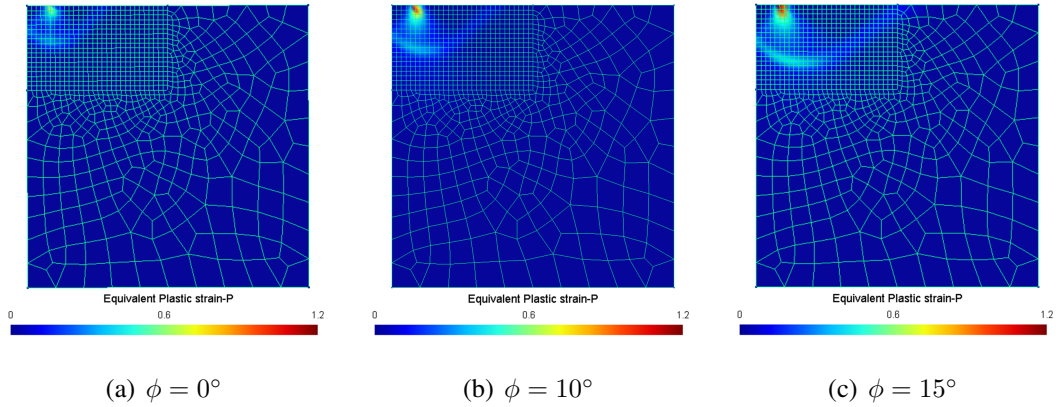
Figure 5.9: Shallow foundation: accumulated equivalent plastic strain distribution for different friction angles (U = 0.1 m [1])

A set of soil parameters used in the numerical analysis presented hereafter are listed in Table 5.4. Each parameter is then varied separately while keeping other parameter equal to the given values in Table 5.4. The basic second gradient parameter $D_{sg}$ was chosen to be $50$ $\mathrm{Pa} \cdot \mathrm{m}^2$ according to the previous bearing capacity validation case.

Table 5.4: Soil parameters of the viscoplastic model in a second gradient continuum

| Category | Parameter | Value |
|---|---|---|
| Elastic parameters | Young's modulus $E$ | $35000\,\mathrm{kPa}$ |
| | Poisson's ratio $\nu$ | 0.3 |
| Plastic parameters | Cohesion $c$ | $20\,\mathrm{kPa}$ |
| | Friction angle $\phi$ | $20°$ |
| | Dilatation angle $\psi$ | $10°$ |
| | Softening modulus $h$ | $-1 \times 10^5$ |
| Viscous parameter | Viscosity parameter $\eta$ | $1 \times 10^9\,\mathrm{Pa \cdot s}$ |
| | Calibration parameter $N$ | 1 |
| Second grade | Second gradient parameter $D_{sg}$ | $50\,\mathrm{Pa \cdot m^2}$ |
| Loading parameters | Loading velocity $v$ | $1 \times 10^{-4}\,\mathrm{m/s}$ |

## 5.5.1 Failure modes

A Prandtl-type failure mechanism is observed throughout the calculations with the viscoplastic model in a second gradient continuum. In order to get a better understanding of the shear band evolution, four typical loading stages are chosen, from A-D, as illustrated in Fig 5.10. The cumulative equivalent plastic strain is shown in Fig 5.11. Plastic strain localizes near the edge of the footing in early stages. With increasing loading, the localized zone enlarges downwards until a wedge-shaped region forms and the peak pressure is attained simultaneously. Inside this region, the soil remains elastic. After the peak, the shear band spreads laterally. However, the accumulated equivalent plastic strain is much lower than that in the previously formed zones.
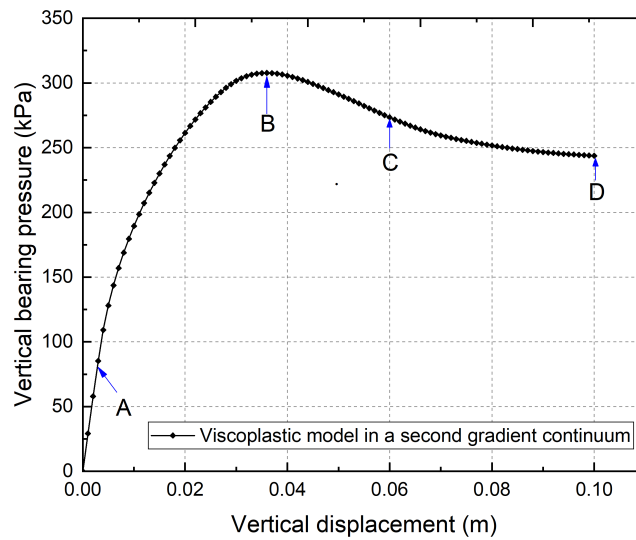
Figure 5.10: Shallow foundation: vertical pressure-vertical displacement curves and four typical stages (A-D) using the viscoplastic law in a second gradient medium
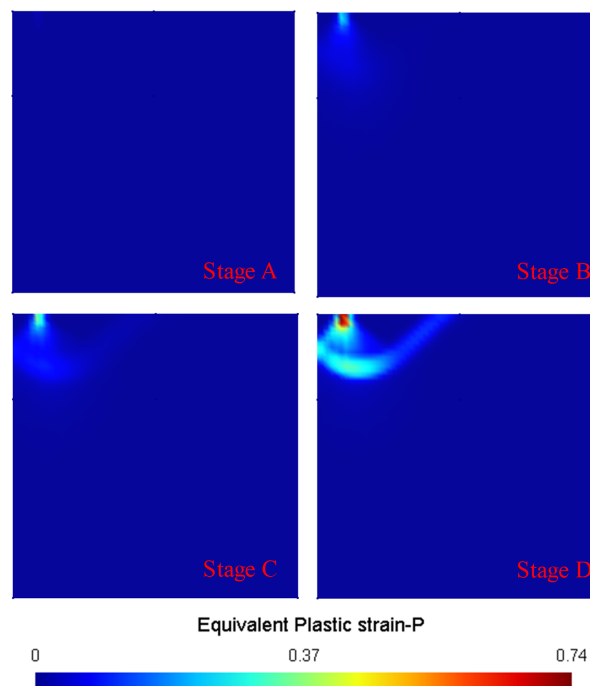


Figure 5.11: Shallow foundation: accumulative equivalent plastic strain for four consecutive loading stages (A-D) using the viscoplastic law in a second gradient medium

The displacement vectors are plotted in Fig 5.12. The magnitude of the displacements is high beneath the footing and decreases in the far distance vertically and laterally until an infinitesimal value.

117
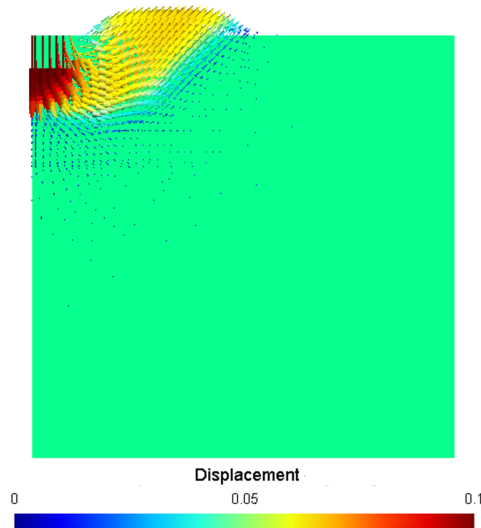
Figure 5.12: Shallow foundation: displacement vectors at the last loading step (U = 0.1 m)

## 5.5.2 Effect of mesh refinement and second gradient parameter

Global results using the two mesh refinements (coarse and dense) and two second gradient parameters ($D_{sg} = 50$ Pa $\cdot$ m$^2$, $D_{sg} = 500$ Pa $\cdot$ m$^2$) are shown in Fig 5.13. For smaller second gradient parameter, $D_{sg} = 50$ Pa $\cdot$ m$^2$, results of the coarse and dense mesh area almost identical. Small differences appear for larger second gradient parameter, $D_{sg} = 500$ Pa $\cdot$ m$^2$, but those differences almost disappear when a denser mesh (very dense mesh) is used, see Fig 5.14.

118
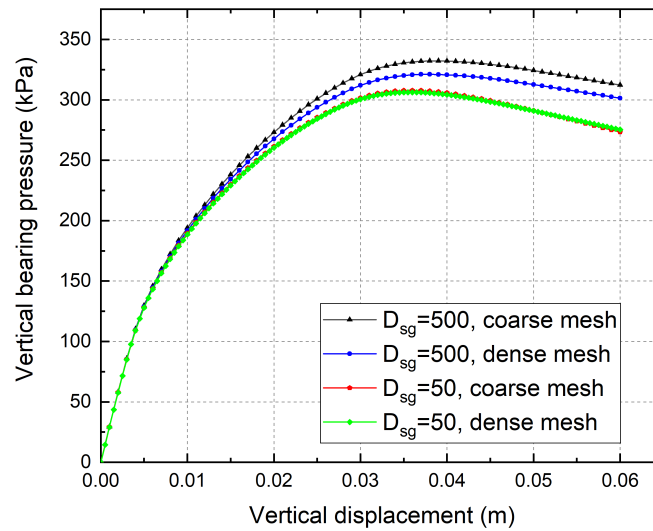
Figure 5.13: Shallow foundation: vertical pressure-displacement of shallow foundation for different second gradient parameters $D_{sg}$ and mesh sizes
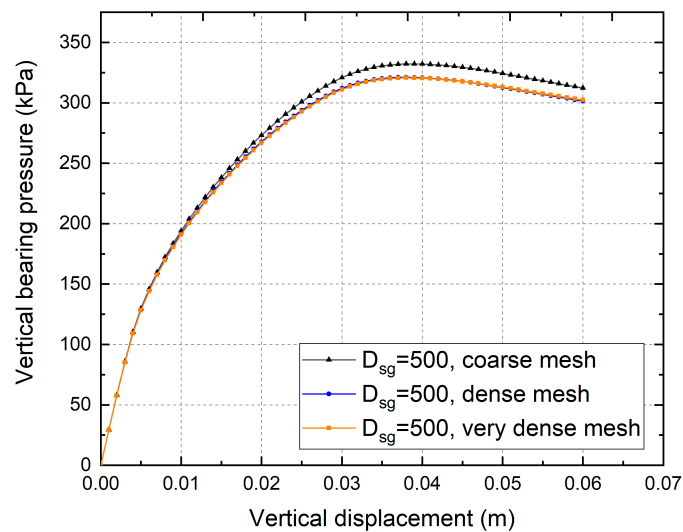


Figure 5.14: Shallow foundation: vertical pressure-displacement of shallow foundation for different mesh sizes with $D_{sg} = 500 \mathrm{Pa} \cdot \mathrm{m}^2$ (U = 0.1 m )

Local results can be seen in Fig 5.15 and Fig 5.16. Comparing the accumulated equivalent plastic strain distributions for the dense and very dense sand it can be concluded that the strain localization zone is mesh independent. The effect of the internal length can also be detected in Fig 5.13 and Fig 5.15. The increase of the second gradient parameter $D_{sg}$

119

leads to an increase of the shear band thickness, an increase of the bearing capacity and a more ductile post-peak response.
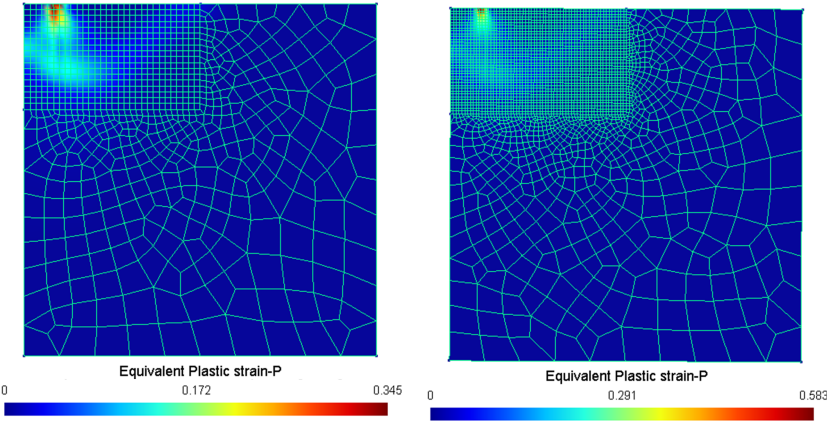


(a) $D_{sg} = 5 \times 10^2$ Pa · m$^2$, coarse mesh

(b) $D_{sg} = 5 \times 10^2$ Pa · m$^2$, dense mesh
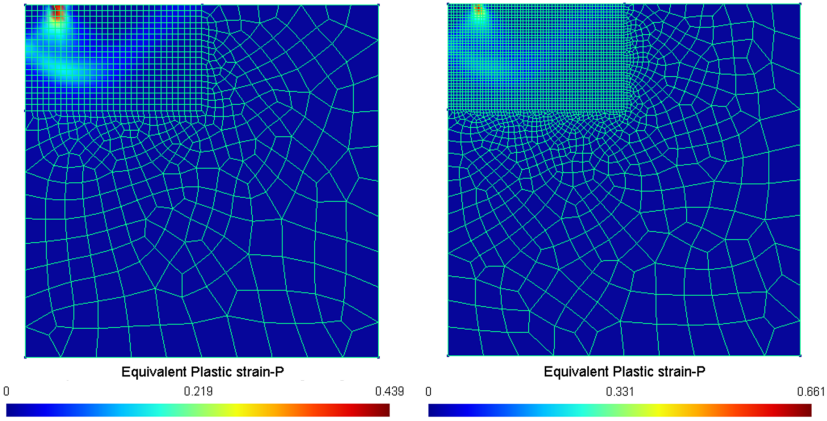
(c) $D_{sg} = 5 \times 10^1$ Pa · m$^2$, coarse mesh

(d) $D_{sg} = 5 \times 10^1$ Pa · m$^2$, dense mesh

Figure 5.15: Shallow foundation: accumulated equivalent plastic strain distribution of shallow foundation for different second gradient parameters and meshes (U $= 0.06$m)
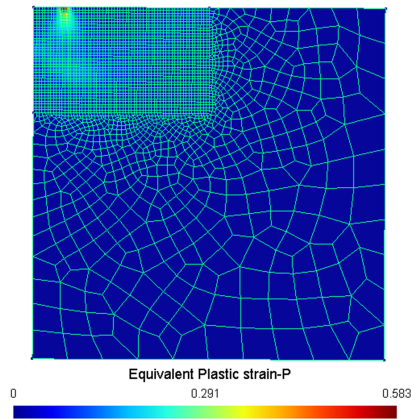
Figure 5.16: Shallow foundation: accumulated equivalent plastic strain distribution of shallow foundation, very dense mesh, $D_{sg} = 500 \, \text{Pa} \cdot \text{m}^2$ (U = 0.06m)

### 5.5.3 Effect of loading velocity

Moreover, the effect of loading velocity on bearing response is investigated. As seen from Fig 5.17, different loading velocities lead to different peak pressures and different slopes of post-peak curve. Increasing the the imposed loading velocity would increase the bearing capacity as well as deduce the steepness of the post-peak curve.
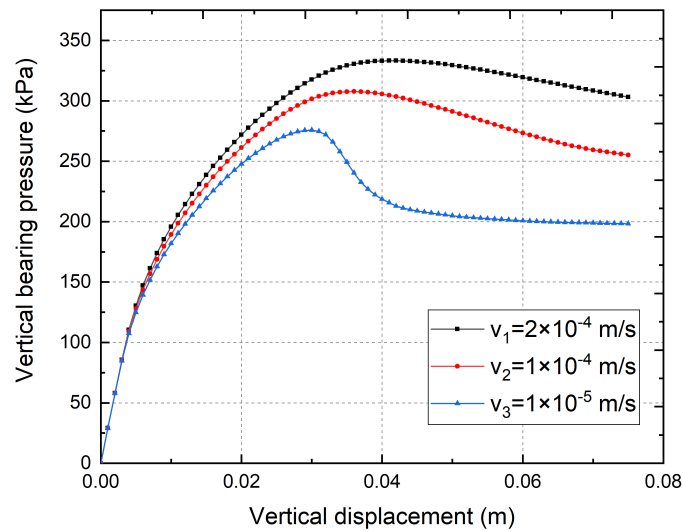


Figure 5.17: Global responses: vertical pressure-displacement of shallow foundation for different imposed velocities

(a) $v_1 = 2 \times 10^{-4}\text{m/s}$  (b) $v_2 = 1 \times 10^{-4}\text{m/s}$  (c) $v_3 = 1 \times 10^{-5}\text{m/s}$
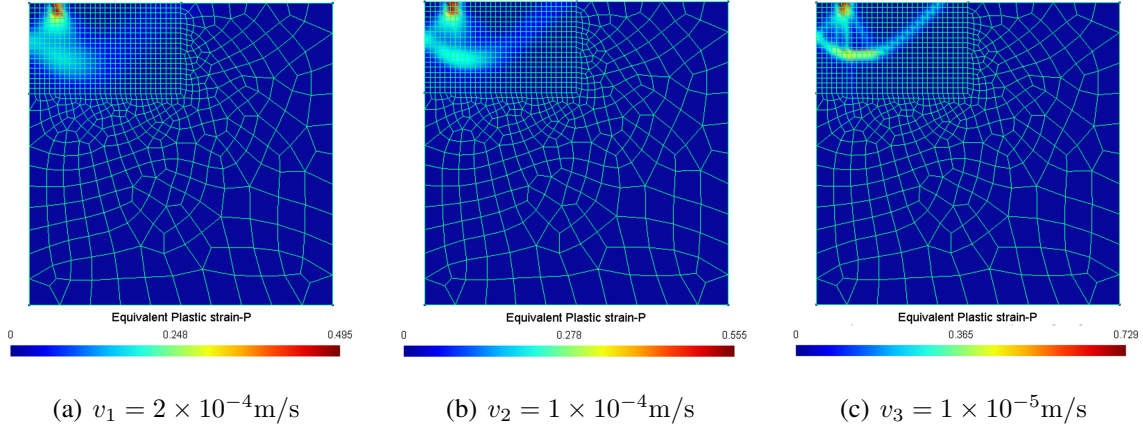
Figure 5.18: Shallow foundation: accumulated equivalent plastic strain distribution of shallow foundation for different imposed loading velocities (U = 0.075m)

Local responses given in Fig 5.18 show that higher loading velocity yields a response closer to the elastic one. As seen locally, no clear shear band is formed and plastic strain mainly localizes in the right edge of the footing. By contrast, lower velocity results in a response approaching the response of rate-independent materials, where clear shear band could be observed. This tendency is consistent with the characteristic of viscoplastic constitutive law.

## 5.6 Concluding remarks

This chapter focuses on a classical boundary value problem, the bearing response and progressive failure of shallow foundation. The viscoplastic model is used in a second gradient medium and it was found that simulations are mesh independent (provided a sufficient dense mesh is adopted). A bigger internal length results in an increase of the foundation bearing capacity and the thickness of shear band, while the post-peak response becomes more ductile. Furthermore, larger loading velocity can cause a higher bearing capacity and a more ductile post-peak response. The use of viscoplastic model in a second gradient continuum can objectively predict progressive failure.

# Chapter 6

# General conclusions and perspectives

## 6.1 Conclusions

This PhD study focuses on the use of viscoplastic models in a classical and in a second gradient medium for the description of geomaterials. Several issues related with strain localization, uniqueness of the solution, bifurcation, stability and mesh dependency are discussed. The main contributions are summarized hereafter.

1. The use of a viscoplastic law in a classical continuum is not sufficient to regularize the strain localization problem, i.e. an infinite number of solutions is possible, strains can localize in an infinitesimal band without energy dissipation. Results are therefore non objective and dependent on the mesh size. The use of a viscosity-like parameter may delay softening, however strain localization and shear bands appear for subsequent loading and time steps. Moreover, the viscosity-like parameter of the constitutive law calibrated from experimental test results is not of the same order of magnitude as the material viscosity measured experimentally.

2. The use of a viscoplastic law in a second gradient medium regularizes the results but do not restore the uniqueness of the solution. Objective results are provided which do not depend on the mesh size or the mesh alignment. A quadratic relation exists between the second gradient parameter $D_{sg}$ and the shear band width.

3. A 1D linear perturbation analysis for a viscoplastic model in a classical medium shows that stability is lost when softening appears. Increasing the viscosity parameter affects only the magnitude of growth rate but does not change its sign. For the viscoplas-

tic model in a second gradient medium stability is conditionally guaranteed and the growth rate is influenced by the wave number and the second gradient parameter. The decrease of the growth rate is realized by increasing the second gradient parameter or the wave number.

4. The classical case study of a shallow foundation shows that increasing the internal length (linked with the second gradient parameter) leads to a higher bearing capacity, a larger shear band width and a more ductile post-peak response. Moreover, larger loading velocity produces a higher bearing capacity as well as a more ductile post-peak response. The use of a viscoplastic model in a second gradient medium gives objective global and local results, provided that a sufficient dense mesh is adopted.

## 6.2 Perspectives

Several perspectives of this work are suggested hereafter.

1. Implementation of more advanced constitutive models in the Matlab based finite element code.

2. Introducing the arc-length technique in the Matlab based finite element code to deal with possible convergence problems (snap-back).

3. Introducing the effect of water (partially drained or undrained conditions).

4. Experimental and numerical studies to identify the internal length of the second gradient model.

# Appendix

## Matlab code

The FE code was originally developed by Bonnet et al.[121]. Nathan Benkemoun applied for classical 2D non linear problems and Bitar [122] added beam elements. In this thesis, various soil constitutive laws (MCC, EVP-MCC and DP) were introduced, as well as the 1D and 2D second gradient finite elements. The link with the GMSH [123] pre and post processing code has been established, as well as the implementation of some specific numerical tools (random initialization, Rice criterion, acoustic tensor . . . )

### General algorithm of the FE code

The general algorithm of the finite element code is summarized in Box 6.1.

In order to simplify some expressions, the following conventions are used.

(1) Global level

$(\cdot)_{(t)}^{(k)}$ Superscript $(k)$ and subscript $(t)$ denotes quantity at time step $t$, $k_{th}$ iteration.

$\mathbf{K}_g$      Global stiffness matrix

$\mathbf{F}_{g,int}$      Global internal force vector

$\mathbf{F}_{g,ext}$      Global external force vector

$\mathbf{F}_{g,eqd}$      Global equivalent displacement force vector

$\mathbf{R}_g$      Global residual force vector

(2) Local level

Subscript $(\cdot)_e$ denotes the numbering of each element; the total element number is $n_e$.

Subscript $(\cdot)_{i_G}$ denotes the numbering of Gauss point; the total Gauss point number is $n_G$.

$\mathbf{K}_e$      Local (element) stiffness matrix

$\mathbf{F}_{e,int}$      Local (element) internal force vector

$\mathbf{\Delta}\varepsilon_{i_G}$      Strain of the $i_G$th Gauss point

$\boldsymbol{\Delta}\sigma_{i_G}$    Stress increment of the $i_G$th Gauss point

$\sigma_{i_G}$    Total stress of the $i_G$th Gauss point

$\mathbf{C}^{ep}_{i_G}$    Elastoplastic tangent moduli of the $i_G$th Gauss point

$\mathbf{B}$    Strain–displacement matrix of the $i_G$th Gauss point

1 Initialize the variables and matrices

$\mathbf{K}_{g,t_0}^{(0)}, \mathbf{F}_{int,t_0}^{(0)}, \mathbf{F}_{ext,t_0}^{(0)}, \mathbf{F}_{eqd,t_0}^{(0)}$

2 Loop on the time step

   2.1 Initial estimate of forces and displacement increments

      $\mathbf{F}_{int,(t+1)}^{(0)} = \mathbf{F}_{int,(t)}, \mathbf{F}_{eqd,(t+1)}^{(0)} = \mathbf{F}_{eqd,(t)}$

      $\mathbf{\Delta U}_{g,(t+1)}^{(0)} = \mathbf{O}$

   2.2 Loop inside one time ($k \geqslant 0$)

      $\mathbf{R}_{t+1}^{(k)} = \mathbf{F}_{ext,(t+1)} - \mathbf{F}_{int,(t+1)}^{(k)} - \Delta t \mathbf{F}_{eqd,(t+1)}^{(k)}$

      $\mathbf{\Delta U}_{g,(t+1)}^{(k+1)} = \mathbf{\Delta U}_{g,(t+1)}^{(k)} - \left[\mathbf{K}_{g,(t+1)}^{(k)}\right]^{-1} \mathbf{R}_t^{(k)}$

      2.2.1 Loop on the element

         (1) Calculate strain from nodal displacements

            $\mathbf{\Delta U}_e, \mathbf{\Delta}\varepsilon_{i_G} = \mathbf{B}_{i_G}\mathbf{\Delta U}_e$

         (2) Loop on the constitutive law

            $\mathbf{\Delta}\sigma_{i_G}, \sigma_{i_G}, \mathbf{C}_{i_G}^{ep}$

         (3) Assembly of the nodal forces and stiffness matrix of element

            $\mathbf{K}_e = \sum\limits_{i_G=1}^{n_G} \int\limits_V \mathbf{B}_{i_G}^T \mathbf{C}_{i_G}^{ep} \mathbf{B}_{i_G} dV$

            $\mathbf{F}_{e,\text{int}} = \sum\limits_{i_G=1}^{n_G} \int\limits_V \mathbf{B}_{i_G} \sigma_{i_G} dV$

      2.2.2 Assembly of the global nodal forces and stiffness matrix

         $\mathbf{K}_{g,(t+1)}^{(k+1)} = \sum\limits_{e=1}^{n_e} \mathbf{K}_e$

         $\mathbf{F}_{g,int,(t+1)}^{(k+1)} = \sum\limits_{e=1}^{n_e} \mathbf{F}_{e,\text{int}}$

      2.2.3 Evaluate residual force

         $\mathbf{R}_{t+1}^{(k+1)} = \mathbf{F}_{ext,(t+1)} - \mathbf{F}_{int,(t+1)}^{(k+1)}$

           IF $\frac{\left\|\mathbf{R}_{t+1}^{(k+1)}\right\|}{1+\left\|\mathbf{F}_{int,(t+1)}^{(k+1)}\right\|} > Tol$

              $(\cdot)_{(t+1)}^{(k)} \leftarrow (\cdot)_{(t+1)}^{(k+1)}$ and go to 2.2

           ELSE

              Update solution

              $\mathbf{U}_{g,(t+1)} = \mathbf{\Delta U}_{g,(t+1)}^{(k+1)} + \mathbf{U}_{g,(t)}$

              set $(\cdot)_{(t)} \leftarrow (\cdot)_{(t+1)}^{(k+1)}$ and go to 2

# References

[1] L. Bjerrum, "Engineering geology of norwegian normally-consolidated marine clays as related to settlements of buildings," *Geotechnique*, vol. 17, no. 2, pp. 83–118, 1967.

[2] S. Lerouel, M. Kabbaj, F. Tavenas, and R. Bouchard, "Stress-strain-strain rate relation for the of sensitive natural clays compressibility," *Geotechnique*, vol. 35, no. 2, pp. 159–180, 1985.

[3] J.-G. Zhu, J.-H. Yin, and S.-T. Luk, "Time-dependent stress-strain behavior of soft hong kong marine deposits," *Geotechnical Testing Journal*, vol. 22, no. 2, pp. 118–126, 1999.

[4] J. Yuan, Q. Zhang, B. Li, and X. Zhao, "Experimental analysis of shear band formation in plane strain tests on shanghai silty clay," *Bulletin of Engineering Geology and the Environment*, vol. 72, no. 1, pp. 107–114, 2013.

[5] V. Thakur, S. Nordal, G. Viggiani, and P. Charrier, "Shear bands in undrained plane strain compression of norwegian quick clays," *Canadian Geotechnical Journal*, vol. 55, no. 1, pp. 45–56, 2017.

[6] V. Thakur, G. Grimstad, and S. Nordal, "Instability in soft sensitive clays," in *PROCEEDINGS OF GEOHAZARDS*, 2006.

[7] J. Desrues and G. Viggiani, "Strain localization in sand: an overview of the experimental results obtained in grenoble using stereophotogrammetry," *International Journal for Numerical and Analytical Methods in Geomechanics*, vol. 28, no. 4, pp. 279–321, 2004.

[8] R. Chambon, D. Caillerie, and N. El Hassan, "One-dimensional localisation studied with a second grade model," *European Journal of Mechanics-A/Solids*, vol. 17, no. 4, pp. 637–656, 1998.

[9] T. Adachi and F. Oka, "Constitutive equations for normally consolidated clay based on elasto-viscoplasticity," *Soils and Foundations*, vol. 22, no. 4, pp. 57–70, 1982.

[10] J.-H. Yin and J. Graham, "Elastic viscoplastic modelling of the time-dependent stress-strain behaviour of soils," *Canadian Geotechnical Journal*, vol. 36, no. 4, pp. 736–745, 1999.

[11] P. Hicher, "Experimental study of viscoplastic mechanisms in clay under complex loading," *Géotechnique*, vol. 66, no. 8, pp. 661–669, 2016.

[12] H. Jostad and S. Degago, "Comparison of methods for calculation of settlements of soft clay," in *Proceedings of the 7th European Conference on Numerical Methods in Geotechnical Engineering*, pp. 57–62, 2010.

[13] Z. P. Bazant and G. Pijaudier-Cabot, "Nonlocal continuum damage, localization instability and convergence," *Journal of applied mechanics*, vol. 55, no. 2, pp. 287–293, 1988.

[14] Z. P. Bažant and F.-B. Lin, "Nonlocal smeared cracking model for concrete fracture," *Journal of Structural Engineering*, vol. 114, no. 11, pp. 2493–2510, 1988.

[15] E. Lorentz and S. Andrieux, "A variational formulation for nonlocal damage models," *International Journal of Plasticity*, vol. 15, no. 2, pp. 119–138, 1999.

[16] E. C. Aifantis, "On the microstructural origin of certain inelastic models," *Journal of Engineering Materials and technology*, vol. 106, no. 4, pp. 326–330, 1984.

[17] P. Germain, "The method of virtual power in continuum mechanics. part 2: Microstructure," *SIAM Journal on Applied Mathematics*, vol. 25, no. 3, pp. 556–575, 1973.

[18] R. D. Mindlin, "Micro-structure in linear elasticity," *Archive for Rational Mechanics and Analysis*, vol. 16, no. 1, pp. 51–78, 1964.

[19] A. Needleman, "Material rate dependence and mesh sensitivity in localization problems," *Computer methods in applied mechanics and engineering*, vol. 67, no. 1, pp. 69–85, 1988.

[20] W. Wang and L. Sluys, "Formulation of an implicit algorithm for finite deformation viscoplasticity," *International Journal of Solids and Structures*, vol. 37, no. 48-50, pp. 7329–7348, 2000.

[21] J. Pan, "Perturbation analysis of shear strain localization in rate sensitive materials," *International Journal of Solids and Structures*, vol. 19, no. 2, pp. 153–164, 1983.

[22] C. Di Prisco, S. Imposimato, and E. Aifantis, "A visco-plastic constitutive model for granular soils modified according to non-local and gradient approaches," *International journal for numerical and analytical methods in geomechanics*, vol. 26, no. 2, pp. 121–138, 2002.

[23] A. Augustesen, M. Liingaard, and P. V. Lade, "Evaluation of time-dependent behavior of soils," *International Journal of Geomechanics*, vol. 4, no. 3, pp. 137–156, 2004.

[24] N. Sivasithamparam, M. Karstunen, and P. Bonnier, "Modelling creep behaviour of anisotropic soft soils," *Computers and Geotechnics*, vol. 69, pp. 46–57, 2015.

[25] W. Huang, S. Fityus, D. Bishop, D. Smith, and D. Sheng, "Finite-element parametric study of the consolidation behavior of a trial embankment on soft clay," *International Journal of Geomechanics*, vol. 6, no. 5, pp. 328–341, 2006.

[26] P. Perzyna, "Fundamental problems in viscoplasticity," *Advances in applied mechanics*, vol. 9, pp. 243–377, 1966.

[27] M. Naatanen, M. Lojander, and N. Puumalainen, "Primary and secondary consolidation of finish clays," *Compression and consolidation of clayey soils. Balkema, Rottrerdam*, pp. 162–170, 1995.

[28] P. G. Joseph, "Viscosity and secondary consolidation in one-dimensional loading," *Geotechnical Research*, vol. 1, no. 3, pp. 90–98, 2014.

[29] V. Navarro and E. Alonso Pérez de Agreda, "Secondary compression of clays as a local dehydration process," *Géotechnique*, vol. 51, no. 10, pp. 859–869, 2001.

[30] J. H. Cushman *et al.*, "A multiscale theory of swelling porous media: Ii. dual porosity models for consolidation of clays incorporating physicochemical effects," *Transport in porous media*, vol. 28, no. 1, pp. 69–108, 1997.

[31] P. Cosenza and D. Korošak, "Secondary consolidation of clay as an anomalous diffusion process," *International Journal for Numerical and Analytical Methods in Geomechanics*, vol. 38, no. 12, pp. 1231–1246, 2014.

[32] M. Liingaard, A. Augustesen, and P. V. Lade, "Characterization of models for time-dependent behavior of soils," *International Journal of Geomechanics*, vol. 4, no. 3, pp. 157–177, 2004.

[33] B. Kutter and N. Sathialingam, "Elastic-viscoplastic modelling of the rate-dependent behaviour of clays," *Géotechnique*, vol. 42, no. 3, pp. 427–441, 1992.

[34] Z.-Y. Yin, M. Karstunen, C. S. Chang, M. Koskinen, and M. Lojander, "Modeling time-dependent behavior of soft sensitive clay," *Journal of geotechnical and geoenvironmental engineering*, vol. 137, no. 11, pp. 1103–1113, 2011.

[35] M. Lazari, L. Sanavia, C. di Prisco, and F. Pisanò, "Predictive potential of perzyna viscoplastic modelling for granular geomaterials," *International Journal for Numerical and Analytical Methods in Geomechanics*, vol. 43, no. 2, pp. 544–567, 2019.

[36] B. HERVE DI, F. Tatsuoka, and M. Ishihara, "Time-dependent shear deformation characteristics of sand and their constitutive modelling.," *Journal of the Japanese Geotechnical Society : soils and foundations.*, vol. 42, no. 2, pp. 1–22, 2002.

[37] D. Pham Van Bang, H. Di Benedetto, A. Duttine, and A. Ezaoui, "Viscous behaviour of dry sand," *International Journal for Numerical and Analytical Methods in Geomechanics*, vol. 31, no. 15, pp. 1631–1658, 2007.

[38] J. K. Mitchell and Z. V. Solymar, "Time-dependent strength gain in freshly deposited or densified sand," *Journal of Geotechnical Engineering*, vol. 110, no. 11, pp. 1559–1576, 1984.

[39] A. Singh and J. K. Mitchell, "Closure of general stress-strain-time function for soils," *Journal of Soil Mechanics & Foundations Div*, 1969.

[40] W. Lacerda, "Stress relaxation in soils," *Proc. 8th ICSMFE, Moscow, 1973*, pp. 221–227, 1973.

[41] S. Leroueil, M. Kabbaj, F. Tavenas, and R. Bouchard, "Stress–strain–strain rate relation for the compressibility of sensitive natural clays," *Géotechnique*, vol. 35, no. 2, pp. 159–180, 1985.

[42] J.-H. Yin and J. Graham, "Viscous–elastic–plastic modelling of one-dimensional time-dependent behaviour of clays," *Canadian Geotechnical Journal*, vol. 26, no. 2, pp. 199–209, 1989.

[43] J. Yin and J. Graham, "General elastic viscous plastic constitutive relationships for 1-d straining in clays," in *Proc., 3rd Int. Symp. Numerical Models in Geomechanics*, pp. 108–117, 1989.

[44] G. Duvaut and J. L. Lions, *Les inéquations en mécanique et en physique*. Dunod, 1972.

[45] H. Sekiguchi, "Macrometric approaches-static-intrinsically time-dependent," *Constitutive Laws of Soils, Proc. Discussion Session 1A, 11th ICSMFE, 1985*, pp. 66–98, 1985.

[46] K. Iwashita and M. Oda, *Mechanics of granular materials: an introduction*. CRC press, 1999.

[47] W. Wang, L. Sluys, and R. De Borst, "Viscoplasticity for instabilities due to strain softening and strain-rate softening," *International Journal for Numerical Methods in Engineering*, vol. 40, no. 20, pp. 3839–3864, 1997.

[48] P. Perzyna, "The constitutive equations for rate sensitive plastic materials," *Quarterly of applied mathematics*, vol. 20, no. 4, pp. 321–332, 1963.

[49] J. Simo, J. Kennedy, and S. Govindjee, "Non-smooth multisurface plasticity and viscoplasticity. loading/unloading conditions and numerical algorithms," *International Journal for Numerical Methods in Engineering*, vol. 26, no. 10, pp. 2161–2185, 1988.

[50] T. J. Hughes and R. L. Taylor, "Unconditionally stable algorithms for quasi-static elasto/visco-plastic finite element analysis," *Computers & Structures*, vol. 8, no. 2, pp. 169–173, 1978.

[51] J. Simo and T. Hughes, *Computational Inelasticity (Interdisciplinary Applied Mathematics)(Volume 7)*. Springer Science & Business Media, 1998.

[52] J. Ju, "Consistent tangent moduli for a class of viscoplasticity," *Journal of Engineering Mechanics*, vol. 116, no. 8, pp. 1764–1779, 1990.

[53] R. J. Finno, W. Harris, M. A. Mooney, and G. Viggiani, "Shear bands in plane strain compression of loose sand," *Geotechnique*, vol. 47, no. 1, pp. 149–165, 1997.

[54] G. Viggiani, S. Marello, L. Lenti, and J. Desrues, "Shear bands in plane strain compression of stiff clay," 2003.

[55] A. S. Gylland, H. P. Jostad, and S. Nordal, "Experimental study of strain localization in sensitive clays," *Acta Geotechnica*, vol. 9, no. 2, pp. 227–240, 2014.

[56] F. Oka, T. Kodaka, S. Kimoto, T. Ichinose, and Y. Higo, "Strain localization of rectangular clay specimen under undrained triaxial compression conditions," in *PROCEEDINGS OF THE INTERNATIONAL CONFERENCE ON SOIL MECHANICS AND GEOTECHNICAL ENGINEERING*, AA BALKEMA PUBLISHERS, 2005.

[57] P. Hicher, H. Wahyudi, and D. Tessier, "Microstructural analysis of strain localisation in clay," *Computers and Geotechnics*, vol. 16, no. 3, pp. 205–222, 1994.

[58] T. Kodaka, Y. Higo, S. Kimoto, and F. Oka, "Effects of sample shape on the strain localization of water-saturated clay," *International journal for numerical and analytical methods in geomechanics*, vol. 31, no. 3, pp. 483–521, 2007.

[59] I. D. Moore and R. Rowe, "Numerical models for evaluating progressive failure in earth structures—a review," *Computers and Geotechnics*, vol. 6, no. 3, pp. 217–239, 1988.

[60] V. Thakur, "Strain localization in sensitive soft clays," *NTNU, Trondheim*, 2007.

[61] K. A. Alshibli and S. Sture, "Shear band formation in plane strain experiments of sand," *Journal of Geotechnical and Geoenvironmental Engineering*, vol. 126, no. 6, pp. 495–503, 2000.

[62] H. Mühlhaus and I. Vardoulakis, "The thickness of shear bands in granular materials," *Geotechnique*, vol. 37, no. 3, pp. 271–283, 1987.

[63] R. Hill, "A general theory of uniqueness and stability in elastic-plastic solids," *Journal of the Mechanics and Physics of Solids*, vol. 6, no. 3, pp. 236–249, 1958.

[64] D. Bigoni, *Nonlinear solid mechanics: bifurcation theory and material instability*. Cambridge University Press, 2012.

[65] C.-F. Zhao, Z.-Y. Yin, and P.-Y. Hicher, "A multiscale approach for investigating the effect of microstructural instability on global failure in granular materials," *International Journal for Numerical and Analytical Methods in Geomechanics*, vol. 42, no. 17, pp. 2065–2094, 2018.

[66] D. Bigoni and D. Zaccaria, "Loss of strong ellipticity in non-associative elastoplasticity," *Journal of the Mechanics and Physics of Solids*, vol. 40, no. 6, pp. 1313–1331, 1992.

[67] J. W. Rudnicki and J. Rice, "Conditions for the localization of deformation in pressure-sensitive dilatant materials," *Journal of the Mechanics and Physics of Solids*, vol. 23, no. 6, pp. 371–394, 1975.

[68] M. Ortiz, Y. Leroy, and A. Needleman, "A finite element method for localized failure analysis," *Computer methods in applied mechanics and engineering*, vol. 61, no. 2, pp. 189–214, 1987.

[69] R. De Borst, "Computation of post-bifurcation and post-failure behavior of strain-softening solids," *Computers & Structures*, vol. 25, no. 2, pp. 211–224, 1987.

[70] R. Chambon, S. Crochepeyre, and R. Charlier, "An algorithm and a method to search bifurcation points in non-linear problems," *International Journal for Numerical Methods in Engineering*, vol. 51, no. 3, pp. 315–332, 2001.

[71] W. Wagner and P. Wriggers, "A simple method for the calculation of postcritical branches," *Engineering computations*, vol. 5, no. 2, pp. 103–109, 1988.

[72] M. Crisfield and J. Wills, "Solution strategies and softening materials," *Computer methods in applied mechanics and engineering*, vol. 66, no. 3, pp. 267–289, 1988.

[73] R. de Borst, "Numerical modelling of bifurcation and localisation in cohesive-frictional materials," *pure and applied geophysics*, vol. 137, no. 4, pp. 367–390, 1991.

[74] B. Loret and J. H. Prevost, "Dynamic strain localization in elasto-(visco-) plastic solids, part 1. general formulation and one-dimensional examples," *Computer Methods in Applied Mechanics and Engineering*, vol. 83, no. 3, pp. 247–273, 1990.

[75] J. M. Melenk and I. Babuška, "The partition of unity finite element method: basic theory and applications," *Computer methods in applied mechanics and engineering*, vol. 139, no. 1-4, pp. 289–314, 1996.

[76] T. Belytschko and T. Black, "Elastic crack growth in finite elements with minimal remeshing," *International journal for numerical methods in engineering*, vol. 45, no. 5, pp. 601–620, 1999.

[77] J. C. Simo and M. Rifai, "A class of mixed assumed strain methods and the method of incompatible modes," *International journal for numerical methods in engineering*, vol. 29, no. 8, pp. 1595–1638, 1990.

[78] G. Pijaudier-Cabot and Z. P. Bažant, "Nonlocal damage theory," *Journal of engineering mechanics*, vol. 113, no. 10, pp. 1512–1533, 1987.

[79] P. Germain, "La méthode des puissances virtuelles en mécanique des milieux continus," *J. Mécanique*, vol. 12, pp. 236–274, 1973.

[80] F. Calvetti, G. Combe, and J. Lanier, "Experimental micromechanical analysis of a 2d granular material: relation between structure evolution and loading path," *Mechanics of Cohesive-frictional Materials: An International Journal on Experiments, Modelling and Computation of Materials and Structures*, vol. 2, no. 2, pp. 121–163, 1997.

[81] T. MATSUSHIMA, H. SAOMOTO, Y. TSUBOKAwA, and Y. YAMADA, "Grain rotation versus continuum rotation during shear deformation of granular assembly," *Soils and foundations*, vol. 43, no. 4, pp. 95–106, 2003.

[82] T. Matsushima, R. Chambon, and D. Caillerie, "Large strain finite element analysis of a local second gradient model: application to localization," *International journal for numerical methods in engineering*, vol. 54, no. 4, pp. 499–521, 2002.

[83] R. Chambon, D. Caillerie, and C. Tamagnini, "A strain space gradient plasticity theory for finite strain," *Computer Methods in Applied Mechanics and Engineering*, vol. 193, no. 27-29, pp. 2797–2826, 2004.

[84] P. Bésuelle, R. Chambon, and F. Collin, "Switching deformation modes in post-localization solutions with a quasibrittle material," *Journal of Mechanics of materials and structures*, vol. 1, no. 7, pp. 1115–1134, 2006.

[85] B. Pardoen, S. Levasseur, and F. Collin, "Using local second gradient model and shear strain localisation to model the excavation damaged zone in unsaturated claystone," *Rock Mechanics and Rock Engineering*, vol. 48, no. 2, pp. 691–714, 2015.

[86] F. Collin, R. Chambon, and R. Charlier, "A finite element method for poro mechanical modelling of geotechnical problems using local second gradient models," *International journal for numerical methods in engineering*, vol. 65, no. 11, pp. 1749–1772, 2006.

[87] J. Y. Shu, W. E. King, and N. A. Fleck, "Finite elements for materials with strain gradient effects," *International Journal for Numerical Methods in Engineering*, vol. 44, no. 3, pp. 373–391, 1999.

[88] G. Sciarra and S. Vidoli, "Asymptotic fracture modes in strain-gradient elasticity: Size effects and characteristic lengths for isotropic materials," *Journal of Elasticity*, vol. 113, no. 1, pp. 27–53, 2013.

[89] R. Chambon and J.-C. Moullet, "Uniqueness studies in boundary value problems involving some second gradient models," *Computer methods in applied mechanics and engineering*, vol. 193, no. 27-29, pp. 2771–2796, 2004.

[90] R. Fernandes, C. Chavant, and R. Chambon, "A simplified second gradient model for dilatant materials: theory and numerical implementation," *International Journal of Solids and Structures*, vol. 45, no. 20, pp. 5289–5307, 2008.

[91] G. Z. Voyiadjis, R. K. Abu Al-Rub, and A. N. Palazotto, "On the small and finite deformation thermo-elasto-viscoplasticity theory for strain localization problems: Algorithmic and computational aspects," *European Journal of Computational Mechanics/Revue Européenne de Mécanique Numérique*, vol. 15, no. 7-8, pp. 945–987, 2006.

[92] M. S. Niazi, H. Wisselink, and T. Meinders, "Viscoplastic regularization of local damage models: revisited," *Computational mechanics*, vol. 51, no. 2, pp. 203–216, 2013.

[93] L. SLUYS and W. WANG, "Overview of viscoplastic approaches for the modelling of shear bands," in *Advances in Engineering Plasticity and its Applications (aepa 1996)*, pp. 171–177, Pergamon, 1996.

[94] G. Ljustina, M. Fagerström, and R. Larsson, "Rate sensitive continuum damage models and mesh dependence in finite element analyses," *The Scientific World Journal*, vol. 2014, 2014.

[95] R. Larsson, S. Razanica, and B. L. Josefson, "Mesh objective continuum damage models for ductile fracture," *International Journal for Numerical Methods in Engineering*, vol. 106, no. 10, pp. 840–860, 2016.

[96] P. Pirali, G. H. Liaghat, and M. Ahmadi, "Viscoplasticity coupled with nonlocalized damage for incompatibilities due to strain softening," *Mechanics*, vol. 86, no. 6, pp. 17–23, 2010.

[97] P. Kotronis, S. Al Holo, P. Bésuelle, and R. Chambon, "Shear softening and localization: Modelling the evolution of the width of the shear zone," *Acta Geotechnica*, vol. 3, no. 2, pp. 85–97, 2008.

[98] O. M. Heeres, A. S. Suiker, and R. de Borst, "A comparison between the perzyna viscoplastic model and the consistency viscoplastic model," *European Journal of Mechanics-A/Solids*, vol. 21, no. 1, pp. 1–12, 2002.

[99] N. Mac, B. Shahbodaghkhan, and N. Khalili, "A constitutive model for time-dependent behavior of clay," *World Academy of Science, Engineering and Technology, International Journal of Civil, Environmental, Structural, Construction and Architectural Engineering*, vol. 8, no. 6, pp. 596–601, 2014.

[100] R. I. Borja and S. R. Lee, "Cam-clay plasticity, part 1: implicit integration of elastoplastic constitutive relations," *Computer Methods in Applied Mechanics and Engineering*, vol. 78, no. 1, pp. 49–72, 1990.

[101] T. Adachi, "Descriptive accuracy of several existing constitutive models for normally consolidated clays," *Proc. T5th ICONMG, 1985*, vol. 1, pp. 259–269, 1985.

[102] D. Bigoni and T. Hueckel, "Uniqueness and localization—i. associative and non-associative elastoplasticity," *International Journal of Solids and structures*, vol. 28, no. 2, pp. 197–213, 1991.

[103] F. Collin, S. Levasseur, and R. Chambon, "Numerical post failure methods in multiphysical problems," *European Journal of Environmental and Civil Engineering*, vol. 13, no. 7-8, pp. 983–1004, 2009.

[104] F. Collin, P. Kotronis, and B. Pardoen, "Numerical modelling of multiphysics couplings and strain localization," in *Modelling of instabilities and bifurcation in Geomechnics*, pp. 247–291, Alert Geomaterials, 2016. http://alertgeomaterials.eu/publications.

[105] L. Anand, K. Kim, and T. Shawki, "Onset of shear localization in viscoplastic solids," *Journal of the Mechanics and Physics of Solids*, vol. 35, no. 4, pp. 407–429, 1987.

[106] I. Dobovsek and B. Moran, "Material instabilities in rate dependent solids," *European journal of mechanics. A. Solids*, vol. 15, no. 2, pp. 267–294, 1996.

[107] Y. Leroy and M. Ortiz, "Finite element analysis of transient strain localization phenomena in frictional solids," *International Journal for Numerical and Analytical Methods in Geomechanics*, vol. 14, no. 2, pp. 93–124, 1990.

[108] L. E. Vallejo and V. A. Scovazzo, "Determination of the shear strength parameters associated with mudflows," *Soils and foundations*, vol. 43, no. 2, pp. 129–133, 2003.

[109] S. P. Mahajan and M. Budhu, "Viscous effects on penetrating shafts in clays," *Acta Geotechnica*, vol. 1, no. 3, p. 157, 2006.

[110] S. Mahajan and M. Budhu, "Shear viscosity of clays to compute viscous resistance," in *Proceedings of the 12th International Conference of International Association for Computer Methods and Advances in Geomechanics (IACMAG), Goa, India*, 2008.

[111] T. A. Ghezzehei and D. Or, "Rheological properties of wet soils and clays under steady and oscillatory stresses," *Soil Science Society of America Journal*, vol. 65, no. 3, pp. 624–637, 2001.

[112] B. Widjaja and S. H.-H. Lee, "Flow box test for viscosity of soil in plastic and viscous liquid states," *Soils and Foundations*, vol. 53, no. 1, pp. 35–46, 2013.

[113] P. Bésuelle, "Implémentation d'un nouveau type d'élément fini dans le code lagamine pour une classe de lois à longueur interne," 2003. Internal report, FNRS, Belgique, pages 1–17.

[114] M. Kulkarni and T. Belytschko, "On the effect of imperfections and spatial gradient regularization in strain softening viscoplasticity," *Mechanics research communications*, vol. 18, no. 6, pp. 335–343, 1991.

[115] E. Aifantis, F. Oka, A. Yashima, and T. Adachi, "Instability of gradient dependent elasto-viscoplasticity for clay," *International journal for numerical and analytical methods in geomechanics*, vol. 23, no. 10, pp. 973–994, 1999.

[116] F. Oka, A. Yashima, K. Sawada, and E. Aifantis, "Instability of gradient-dependent elastoviscoplastic model for clay and strain localization analysis," *Computer methods in applied mechanics and engineering*, vol. 183, no. 1-2, pp. 67–86, 2000.

[117] K. Terzaghi, *Theoretical soil mechanics*. Chapman And Hall, Limited.; London, 1951.

[118] D. C. Drucker and W. Prager, "Soil mechanics and plastic analysis or limit design," *Quarterly of applied mathematics*, vol. 10, no. 2, pp. 157–165, 1952.

[119] I. Alpan, "The empirical evaluation of the coefficient k0 and k0r," *Soils and foundations*, vol. 7, no. 1, pp. 31–40, 1967.

[120] B. M. Das, *Shallow foundations: bearing capacity and settlement*. CRC press, 2017.

[121] d. M. Bonnet and A. Frangi, "Analyse des solides déformables par la méthode des éléments finis," *European Journal of Computational Mechanics/Revue Européenne de Mécanique Numérique*, vol. 16, no. 5, pp. 667–668, 2007.

[122] I. Bitar, *Modélisation de la rupture dans les structures en béton armé par des éléments finis poutres généralisées et multifibres*. PhD thesis, Ecole Centrale de Nantes (ECN), 2017.

[123] C. Geuzaine and J.-F. Remacle, "Gmsh: A 3-d finite element mesh generator with built-in pre-and post-processing facilities," *International journal for numerical methods in engineering*, vol. 79, no. 11, pp. 1309–1331, 2009.

**Titre :** Visqueux et second gradient techniques de régularisation pour la description du comportement de géomatériaux

**Mots clés :** régularisation, localisation des déformations, viscoplasticité, second gradient

**Résumé :** Les géomatériaux présentent des comportements plus ou moins dépendants du temps, car leur microstructure évolue. Ce processus peut varier entre quelques minutes (sable) et plusieurs jours voire plusieurs années (sols mous). Pour décrire un comportement dépendant du temps, des modèles viscoplastiques, dépendant de la vitesse, sont couramment utilisés. Autre qu'une description intrinsèque du comportement visqueux, la dépendance à la vitesse de la loi constitutive est également présentée quelques fois dans la littérature comme une technique de régularisation.

On étudie dans cette thèse la possibilité d'utiliser une loi de comportement viscoplastique pour décrire le comportement transitoire des sols mous dépendant du temps et la localisation des déformations. Des études analytiques et numériques sont présentées et plusieurs conclusions sont trouvées sur la base du critère de Hill, du critère de Rice, d'un algorithme de perturbation numérique et de la théorie classique de perturbation linéaire. Il s'avère que l'utilisation d'un modèle viscoplastique pour des chargements transitoires ne permet pas de régulariser le problème.

Afin de proposer une stratégie de modélisation performante, les modèles viscoplastiques sont ensuite intégrées dans un milieu à microstructure et plus spécifiquement dans un modèle second gradient. Des problèmes concernant l'unicité, la bifurcation et la dépendance au maillage sont examinés et une analyse classique de perturbation linéaire est présentée. La combinaison d'un modèle second gradient avec des lois viscoplastiques permet de régulariser le problème et de prendre en compte l'influence de la vitesse de la sollicitation. Afin de démontrer la performance de l'approche dans un cas réel, une fondation superficielle est analysée en mettant l'accent sur sa capacité portante et sa défaillance progressive.

**Title :** Viscous and second gradient regularization techniques for the description of the behavior of geomaterials

**Keywords :** regularization, strain localization, viscoplasticity, second gradient

**Abstract:** Geomaterials may exhibit time-dependent behaviors as their microstructures evolve. This process may vary from a few minutes (sand) to several days or even years (soft soils). To describe this time-dependent behavior, viscoplastic models are commonly used. Other than providing an intrinsic description of the viscous behavior, rate-dependent constitutive laws are sometimes presented in the literature as a regularization technique.

In this thesis, we study the possibility to use viscoplastic constitutive laws in transient problems to describe the time-dependent response of soft soils and strain localization. Analytical and numerical studies are presented and several conclusions are found based on the Hill's criterion, the Rice's criterion, a numerical perturbation algorithm and classical linear perturbation theory. It turns out that the use of viscoplastic models in transient problems is not able to regularize the problem.

Viscoplastic models are then integrated in a higher order continuum, the second gradient model. Problems concerning the uniqueness, bifurcation and mesh dependency are examined and a classical linear perturbation analysis is presented.

The combination of a second gradient model with viscoplastic laws makes possible both to regularize the problem and to take into account rate effects. Finally, the bearing capacity and progressive failure of a shallow foundation are analyzed in order to demonstrate the performance of the approach on a real case study.